2P(mix)

X-752-71-277

65866

FINAL REPORT
THE ASEE - UNIVERSITY OF MARYLAND - CATHOLIC UNIVERSITY - NASA SUMMER FACULTY FELLOWSHIP PROGRAM

COMPILED
BY
J. C. MORAKIS

JUNE 15 TO AUGUST 21, 1970

GSFC — GODDARD SPACE FLIGHT CENTER —

GREENBELT, MARYLAND

X-752-71-277

FINAL REPORT
THE ASEE-UNIVERSITY OF MARYLAND-CATHOLIC UNIVERSITY-NASA SUMMER FACULTY FELLOWSHIP PROGRAM

June 15 to August 21, 1970

Goddard Space Flight Center
Greenbelt, Maryland

INTRODUCTION

The GSFC Faculty Fellowship Program is a cooperative effort between Goddard, the American Society of Engineering Education (ASEE), the University of Maryland, and the Catholic University of America.

Under this program university faculty members come to Goddard for a period often weeks during which they engage actively in research and at the same time participate in seminars related to their research.

The objectives of this program are many; some of them are listed below:

1. Stimulation of schools to become interested in the research problems confronting Goddard.

2. Creation of interest on the part of the university faculty to continue their research after completing the formal program.

3. Stimulation of our people professionally through associations with the university faculty and through participation in the program's seminars.

4. Establishment of closer ties with the Universities.

This report marks the completion of the sixth year of this program at Goddard, and represents the progress in one of its objectives.

John F. Clark
Director

PRECEDING PAGE BLANK NOT FILMED

CONTENTS

CONTENTS–(continued)

I ADMINISTRATION

Dr. F. Emad	Co-director	Professor, EE Dept., Univ. of Md.
Dr. B. Fang	Co-director	Professor, S.Sc. Dpt., CU
Dr. J. Morakis	Co-director	Navigation and Data Collection Branch Code 752 GSFC

Acknowledgment: The Co-directors of this program wish to thank the personnel of the Employee Development Branch for their unlimited support and assistance in carrying out this program

II. PARTICIPANTS

A. Second-Year Fellows

Fellow	Academic Rank and Affiliation
Dr. Michael L. Bottino	Associate Professor, Department of Geology, Marshall University, Huntington, West Virginia 25701
Dr. John H. Carman	Assistant Professor, Department of Geology, The University of Iowa, Iowa City, Iowa 52240
Dr. Yukap Hahn	Associate Professor, Department of Physics, University of Connecticut, Storrs, Connecticut 06268
Dr. Ernest H. Henninger	Assistant Professor, Department of Physics, DePauw University, Greencastle, Indiana 46135
Dr. Joseph L. Katz	Instructor, Department of Electrical Engineering, Purdue University, Lafayette, Indiana 47907
Dr. Thomas F. Krile	Assistant Professor, Department of Electrical Engineering, Rose Polytechnic Institute, Terre Haute, Indiana 47803
Dr. Alfred G. Lieberman	Assistant Professor, Electrical Engineering Department, University of Maryland, College Park, Maryland 20742
Dr. Frederick H. Morse	Assistant Professor, Mechanical Engineering Department, University of Maryland, College Park, Maryland 20742
Dr. Lennart R. Peterson	Assistant Professor, Department of Physics and Astronomy, University of Florida, Gainesville, Florida 32601
Jacob C. Sabto	Lecturer, Department of Electronic Engineering, California State Polytechnic College, San Luis Obispo, California 93490
Dr. William R. Thickstun, Jr.	Associate Professor, Department of Mathematics, Clarkson College of Technology, Potsdam, New York 13676
Dr. Robert E. Wilson	Associate Professor, Department of Astronomy, University of South Florida, Tampa, Florida 33620
Dr. Rodger E. Ziemer	Associate Professor, Department of Electrical Engineering, University of Missour-Rolla, Rolla, Missouri 65401

B. First-Year Fellows

Fellow	Academic Rank and Affiliation
Dr. Virgilio Acosta	Associate Professor, Physics Department, U.S. Naval Academy, Annapolis, Maryland 21402
Dr. Peter M. Bainum	Associate Professor, Mechanical Engineering Department Howard University, Washington, D. C. 20001

Fellow	Academic Rank and Affiliation
Dr. Kenneth H. Carpenter	Associate Professor, Department of Physics, East Tennessee State University, Johnson City, Tennessee 37601
Dr. Stephen W. Ching	Associate Professor, Electrical Engineering Department, Villanova University, Villanova, Pennsylvania 19085
Dr. Frederic M. Davidson	Assistant Professor, Electrical Engineering Department, University of Houston, Houston, Texas 77004
Dr. Garabet J. Gabriel	Associate Professor, Electrical Engineering Department, University of Notre Dame, Notre Dame, Indiana 46556
Dr. Edward A. Harms	Assistant Professor, Department of Physics, Fairfield University, Fairfield, Connecticut
Dr. Eugene W. Henry	Professor, Electrical Engineering Department, University of Notre Dame, Notre Dame, Indiana 46556
Dr. David M. LeVine	Assistant Professor, Electrical Engineering Department, University of Maryland, College Park, Maryland 20742
Dr. Victor J. Newton	Assistant Professor, Department of Physics, Fairfield University, Fairfield, Connecticut 06430
Dr. Tung Tsang	Associate Professor, Department of Physics, Howard University, Washington, D. C. 20001

C. Goddard Personnel

Name	Name
Andrew R. Chi Code 521	Nelson McAvoy Code 524
Lawrence T. Draper Code 732	C. L. Parsons Code 325
Joseph Epstein Code 716	Dr. Robert W. Rochelle Code 710
Dr. J. V. Fedor Code 723	John Rodgers Code 521
Dr. Subrata Ghose Code 644	David H. Schaeffer Code 711
Thomas S. Golden Code 520	Thomas P. Sciacca, Jr. Code 735
Dr. Donald F. Heath Code 622	Reginald K. Squires Code 643
Dr. W. A. Hovis Code 622	Dr. Aaron Temkin Code 641
	Dr. Louis W. Walter Code 644
	George Winston Code 525

III EDUCATIONAL PROGRAM

I. Short Courses (Room 207, Building 26, Goddard Space Flight Center)

1. Systems & Optics

Instructor:	Dr. A. Papoulis Professor of Electrical Engineering Polytechnic Institute of Brooklyn
Date & Hours:	8:30 - 10:30 a.m., the week of June 22-26, 1970.

2. Basic Network Synthesis

Instructor:	Dr. Kendall L. Su Regents Professor Georgia Institute of Technology
Date & Hours:	8:30 - 10:30 a.m., the week of August 3-7, 1970.

II. Lectures and Seminars (Room 207, Building 26, Goddard Space Flight Center)

Date & Time	Subject	Speaker
Wednesday, June 17 8:30 a.m. - 10:00 a.m.	Optical Tracking and Communications Program	Dr. Henry H. Plotkin Head, Optical Systems GSFC
Thursday, June 18 10:00 a.m. - 11:30 a.m.	Computers at GSFC	Mr. James Fleming Deputy Director, Center of Automatic Data Processing, GSFC
Friday, June 19 9:00 a.m. - 10:30 a.m.	Spacecraft Technology and Research	Dr. R. Rochelle Asst. Chief, Spacecraft Technology Division, GSFC
Monday, July 6 8:30 a.m. - 10:00 a.m.	Recent Studies on Tornado-like Vortices	Dr. Chieh C. Chang Professor and Chairman Dept. of Aerospace & Atmospheric Sciences Catholic Univ. of America
Monday, July 13 9:30 a.m. - 11:00 a.m.	On the Stability of Non-linear Control Systems	Dr. V. M. Popov Professor, Dept. of Electrical Engineering University of Maryland
Monday, July 20 8:30 a.m. - 10:00 a.m.	The Biological Revolution	Dr. Roland M. Nardone Professor of Biology Catholic Univ. of America

Date & Time	Subject	Speaker
Monday, July 27 8:30 a.m. - 10:00 a.m.	A Review of the Theory of Linear Time Varying Systems	Dr. N. DeClaris Professor and Chairman Dept. of Electrical Engineering University of Maryland
Monday, August 3 8:30 a.m. - 10:00 a.m.	Bioengineering and the Study of Living Cells - Prospects for the Future	Dr. Roland M. Nardone Professor of Biology Catholic Univ. of America
Monday, August 10 2:00 p.m. - 3:30 p.m.	A Special Purpose Digital Signal Processor, Its Design, Economics and Application	Dr. James F. Kaiser Bell Telephone Laboratory
Monday, August 17 8:30 a.m. - 10:00 a.m.	Ocean Engineering	Dr. Frank Andrews Professor and Chairman Dept. of Mechanical and Civil Engineering Catholic Univ. of America

IV RESEARCH

PRE-VIBRATION MAGNETIC TESTING OF THE SAS-A

Dr. Virgilio Acosta
Associate Professor of Physics
United States Naval Academy
Annapolis, Maryland 21402

1. BRIEF DESCRIPTION OF THE MAGNETIC TEST SITE FACILITY

The Magnetic Test Site is a complex of eleven different buildings outside the main campus of GSFC and located in a wooded area near Good Luck Road, in Greenbelt, Maryland. A sketch of the distribution of the buildings, not on scale, appears in Figure 1.

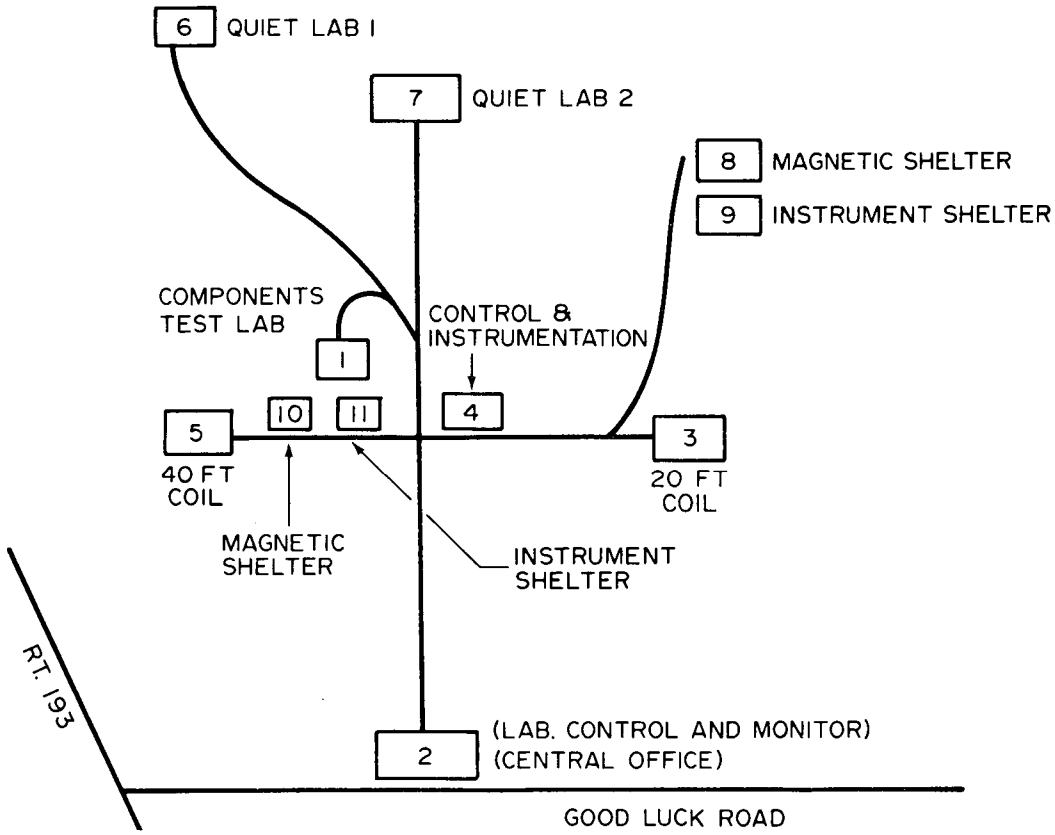

Figure 1. Magnetic Test Site

MAIN OBJECTIVES –

The Magnetic Test Site consists of two principal test facilities; the Spacecraft Magnetic Testing Facility (SMTF) and the Magnetic Instrument Test Lab (MITL).

The SMTF is intended to furnish the GSFC with enough capability for the evaluation of some aspects relative to the control of the orientation of spacecrafts in a magnetic environment, similar to the one they are going to find in outer space. More specifically, the SMTF is intended to provide a controllable large magnetic field (maximum value 60K gamma) and spacewise large enough to accommodate spacecrafts and components bigger than those that can be tested in the MITL. Other capacilities include:

a. Controllable ways for the simulation of the relative motion of the spacecraft under test and the magnetic field in the outerspace in order to find the magnetic forces and torques acting on a flying spacecraft.

b. Mapping contours of the spacecraft's intrinsic magnetic field in a controllable external magnetic field.

c. Study the effects of external magnetic forces and torques on the different subsystems and components of the spacecraft with the main purpose of having attitude control or remove interference with magnetic instruments outboard the spacecraft. The SMTF is located in Building 4.

DESCRIPTION OF FACILITIES

Building 2 - The central office is located in this building as well as a machine shop and the controls of air conditioning in the other buildings.

Building 3 - Contains a tri-axial Helmholtz's coil assembly consisting of 12 coils, 4 horizontal, 4 oriented with the common axis in the NS direction, and 4 with the common axis oriented in the EW direction. Maximum diameter of the coils is 22 ft. Magnetic testing of small spacecrafts or of sounding rockets can be done in this building. Maximum field in any direction is 60K gamma ± 0.2 gamma. The magnetometer that is used in this facility is a triaxial flux-gate, maximum sensitivity is 0.1 gamma. Field can be rotated in any direction at a maximum rate of 100 rad/s. The building is also equipped with a Rubidium vapor magnetometer. Maximum sensitivity is 0.1 gamma.

Building 5 - In this building a three-axis Braunbeck coil system (Figure 2) consisting of 12 coils is installed as in Building 3; 4 coils are horizontal, 4 with the common axis oriented in the NS direction and 4 in the EW direction. The main characteristics are maximum diameter 42 feet; completely non-magnetic structure; magnetic field 0 - ± 60K gamma in any direction; accuracy 0.20 gamma; rotating field 0 - 60K gamma in any direction at a maximum rate of 100 rad/s. Large spacecrafts or rockets are tested in this building. The spacecraft magnetic test facilities are located in this building.

Building 4 - The electronics and instrumentation for the coils in Buildings 3 and 5 are located here. For data acquisition there are four fluxgate triaxial magnetometers with a maximum sensitivity of 0.1 gamma. Several three-axes flux-gate magnetometers (maximum sensitivity 0.1 gamma) and a Rubidium vapor magnetometer (maximum sensitivity 0.1 gamma) are part of the associated equipment.

Building 1 - The main facility in this building is a square coil assembly, 14 feet on each side. The main purpose is to produce a zero field at the center of the facility in order to cancel out the earth's magnetic field within 0.5 gamma in any direction. The facility contains the necessary instrumentation (three axes flux-gate magnetometer, voltmeter, printer, etc.) for performing magnetic field measurements. Components, subsystem testing and dipole determinations can be made in this facility.

Building 8 - Magnetic Shelter. This contains the proper control for canceling out the diurnal fluctuations of the earth magnetic field within 0.5 gamma at the center of the coils in Building 3.

Building 9 - Here are located the necessary electronic hardware to operate the controls in Building 8.

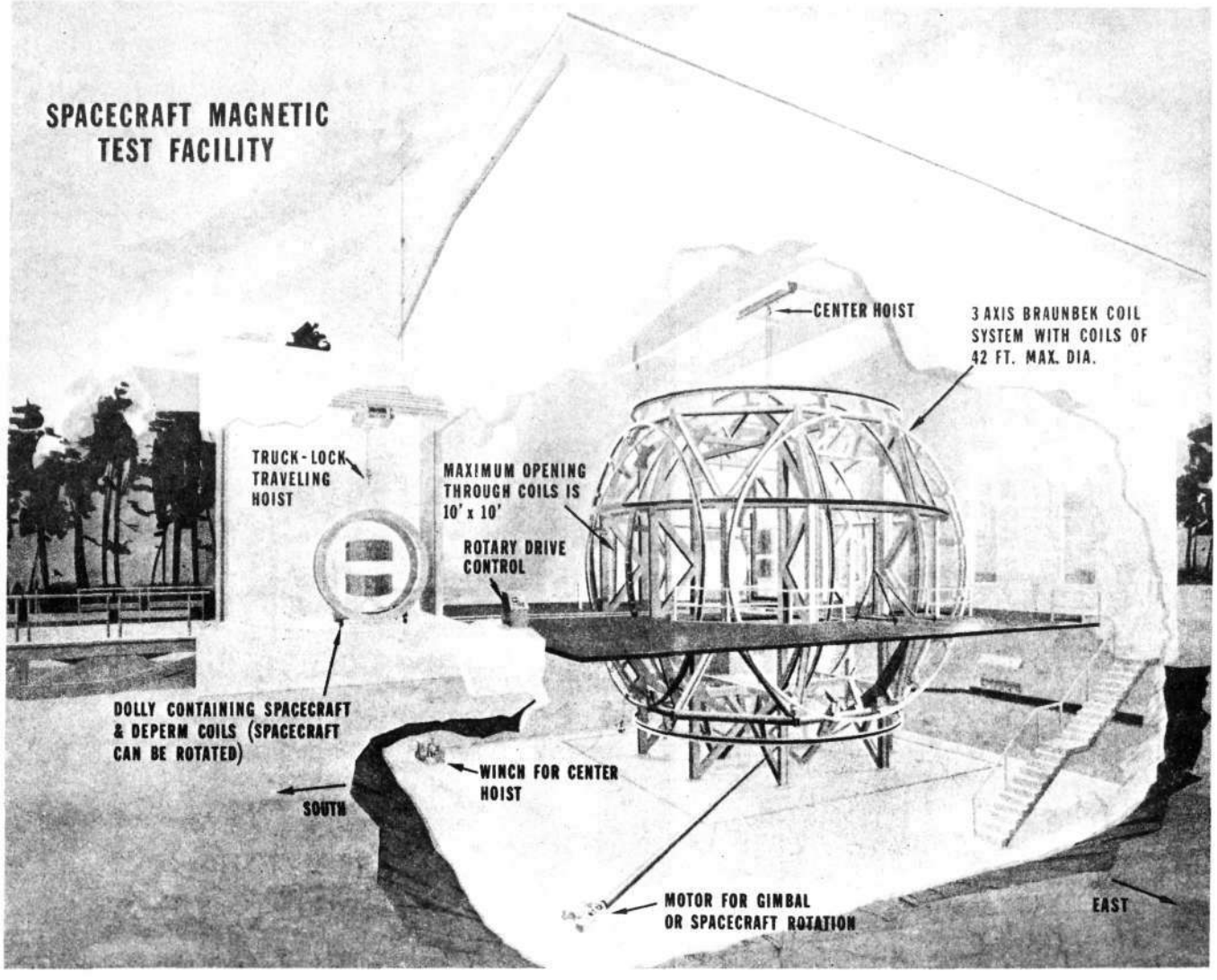

Figure 2. 40 Foot Braunbeck Coil Assembly

Building 10 - Magnetic Shelter. Contains the proper controls for cancelling out the diurnal fluctuations of the earth magnetic field within 0.5 gamma in a spherical volume about 6 feet in diameter with its center coinciding with the center of the Braunbeck coil system in Building 5.

Building 11 - Here are located the necessary electronic hardware to operate the controls in Building 10.

Building 6 - Quiet Lab 1. This facility is operated mainly by the personnel of the Space Science Directorate. The main facility in this building is a Braunbeck 12 foot coil assembly, consisting of 10 coils; 4 are horizontal, 4 are oriented with the common axis in the NS direction, and 2 are oriented with the common axis pointing in the EW direction. It is possible to produce a zero field at the center of the coils and cancel out the diurnal fluctuations of the earth's magnetic field within 0.5 gamma in each direction. The building is equipped with several three axes flux-gate magnetometers (maximum sensitivity 0.1 gamma). The main purpose of the facility is magnetometer development.

Building 7 - Quiet Lab 2. This facility, as the one installed in Building 6, is operated mainly by personnel of the Space Science Directorate. The main facility in this building is a cubical coil assembly, 15 feet on each side. It is possible to cancel out the earth's magnetic field at the center of the coils (within 0.5 gamma) in any direction and at the same time cancel out the diurnal fluctuations of the geomagnetic field (within 0.5 gamma). The building is equipped with several three axes flux-gate magnetometers with a maximum sensitivity of 0.1 gamma. The facility is mainly used in magnetometer development.

2. DESCRIPTION OF THE PREPARATORY WORK DONE (INCLUDING DATA) FOR THE SAS-A PRE-VIBRATION MAGNETIC TEST.

As one of the main goals of the actual testing of the spacecraft, the determination of its associated dipole-moment, it is necessary to simulate the geomagnetic field that the satellite is going to find when it is in flight in order to compute the magnetic torque that will be acting on it in order to have ground control on its attitude (orientation) and spin rate. The magnetic torque is computed by the equation:

$$\boxed{\vec{L} = \vec{M} \times \vec{B}} \qquad (1)$$

in which

M is the magnetic moment in pole-cm.

B is the magnetic field in oersted.

L is the magnetic torque in dyne-cm.

In order to measure the torque a very ingenious device called a torquemeter was designed at the Magnetic Test Site. (Figure 3). The torquemeter that is in use at present is an improved version of the one represented in Figure 3 and was designed by Joseph C. Boyle of the staff of the Magnetic Test Site and in charge of the experimental testing done on spacecrafts, components and subsystems.

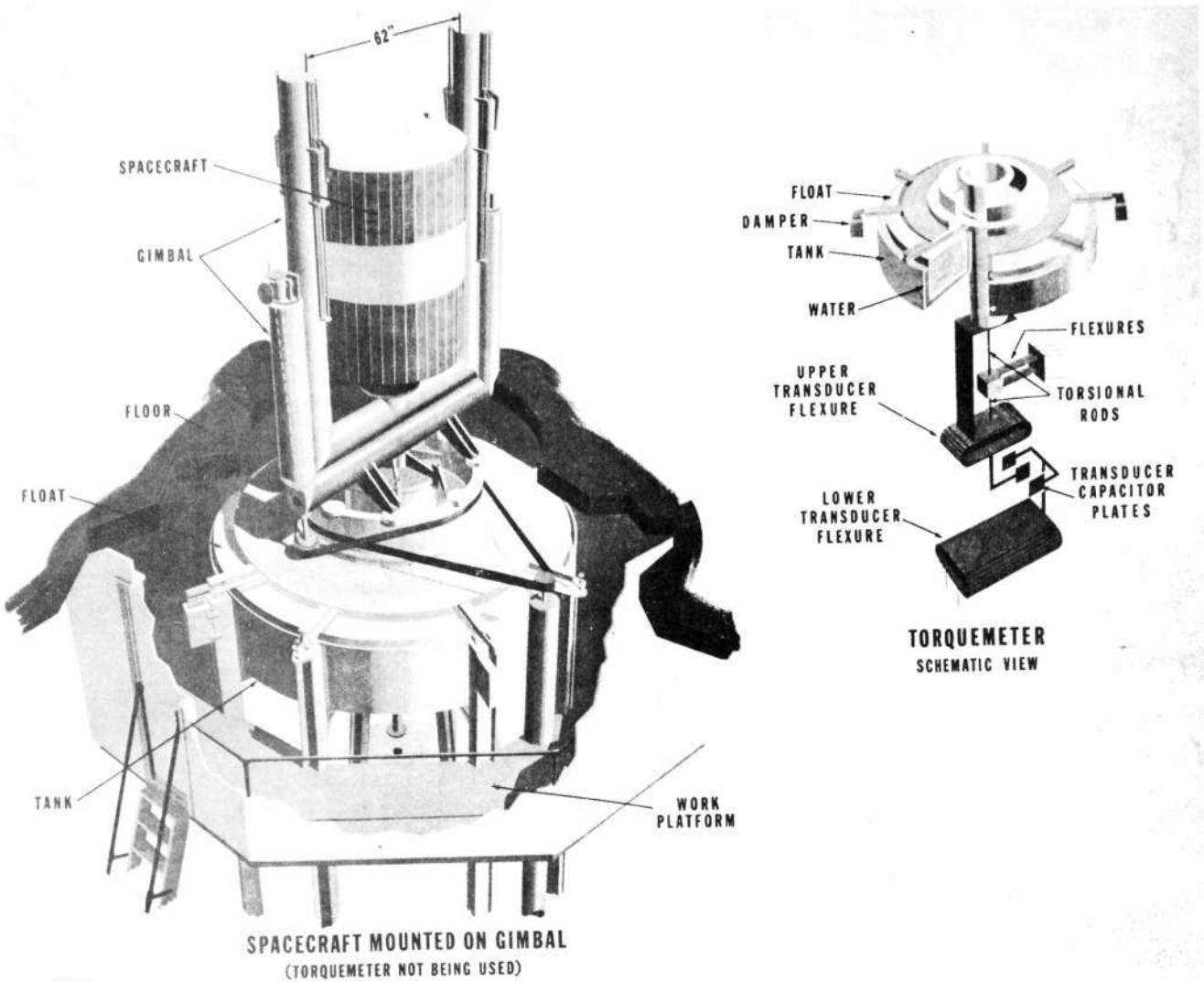

Figure 3. Schematics of the Torquemeter

This improved torquemeter is capable of measuring torques in the vertical direction in the range 0.3 dyne-cm to 10^6 dyne-cm and can be loaded with a maximum load of 800 pounds. In order to produce a known magnetic moment for calibrating the torquemeter and for nulling spacecraft,torques, two air core solenoids at right angles and in a horizontal plane are attached to the torquemeter. These air core coil solenoids can be energized by means of a D.C. current and they have independent circuits, so they can be operated either separately or simultaneously. The purpose of these solenoids is to associate to the torquemeter a magnetic dipole moment that can be varied at will because the other components of the meter are made of non-magnetic materials. Now by placing the torquemeter in an environmental magnetic field, a magnetic torque will be acting on it, the vertical components of which can be measured by remote control. As the two air-core solenoids are mounted at right angles and in a horizontal plane it is necessary to calibrate them in order to know the magnetic moment in the horizontal plane associated with the torquemeter. The calibration constant in pole-cm/amp was measured magnetically by use of the torquemeter. In order to distinguish the air-core solenoids, we will designate them as the radial and tangential coils. If M is the magnetic moment associated with one solenoid and I the energizing current, the calibration constant will be obtained by the expression:

$$K = \frac{M}{I} \text{ ploe-cm/amp.} \qquad (2)$$

Magnetic Calibration of the Air-Coils of the Torquemeter - This was done in Building 1, where one of the cubical coil systems is located (See Figure 3 for the experimental setup).

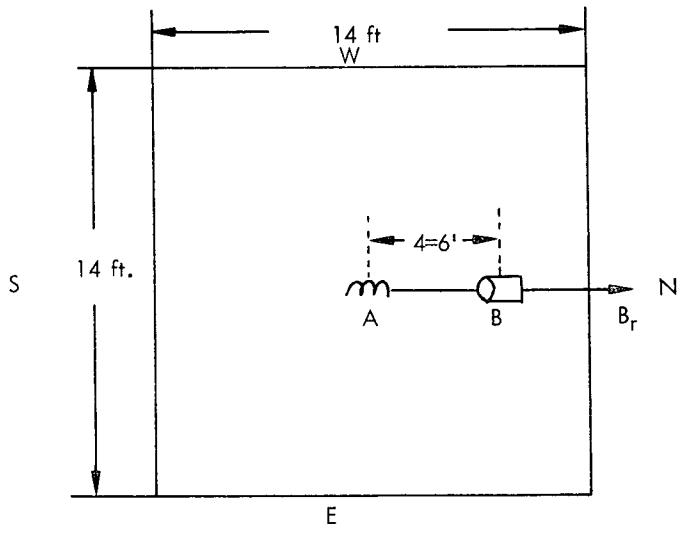

Figure 4. Schematic Set-Up for the Static Air-Coil Calibration

A represents a coil placed horizontally at the center of the cubical coil assembly with its axis pointing in the NS direction and B aligned in the same direction is the probe of a flux-gate magnetometer, the distance r was set at 6 feet. A zero magnetic field was set at the center of the coils, a regulated D.C. current of 1 amp was sent through the coil at A and the corresponding radial magnetic field B_r was measured with the magnetometer.

Then the magnetic moment M associated with the coil was computed using the equation:

$$M = \frac{B_r r^3}{2} \tag{3}$$

Several measurements were made with each coil and the average taken for M. The results were as follows:

$$\text{Radial Coil } K_r = \frac{MR}{I} = 2349 \frac{\text{Pole-cm}}{\text{Amp.}}$$

$$\text{Tangential Coil } K_t = \frac{Mt}{I} = 1958 \frac{\text{Pole-cm}}{\text{Amp.}}$$

Before proceeding to check dynamically the calibration of the two air-core coils of the torquemeter, we performed several preliminary tests relative to the torquemeter itself. In order to conduct these tests we moved the torquemeter to Building 5 where the Braunbeck coil system is installed, and three balance-noise tests were conducted, with the torquemeter unloaded and then loaded with about 100 pounds and finally with 400 pounds. The reason for loading the torquemeter with 400 pounds was to simulate the approximate weight and moment of inertia of the SAS-A spacecraft that we were going to test later on. In this test the torquemeter was placed at the center of the Braunbeck coil system as it is shown in Figure 5 with the Z axis in a vertical position. D_1 and D_2 are two flat squeeze film dampers and by pouring water in both they exert a damping effect on the vibrations of the torquemeter around the Z axis. The main goals of these balance noise tests were to bring the center of mass of the torquemeter to same point along the Z axis and to minimize its output noise by balancing the torquemeter once it is leveled.

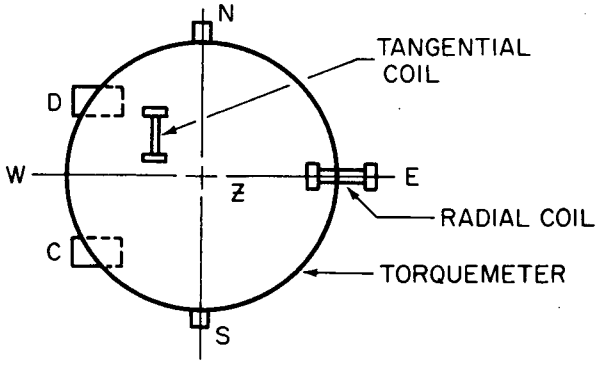

Figure 5. Balance Test of Torquemeter

At this point it is convenient to mention that the output mechanical signal of the torquemeter (the torque acting on it) is transformed into an electrical signal by means of an air differential capacitor (attached to the torquemeter) whose capacitance changes with the applied torque and torque fluctuations acting on it. The electrical output of the torquemeter is transmitted to a two channel recorder where it can be measured and recorded. A block diagram of the setup used for the balance-noise is shown in Figure 6.

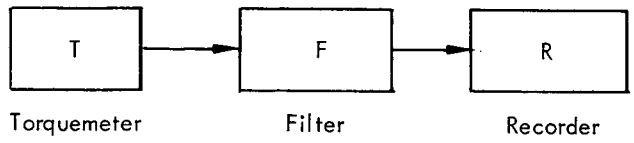

Figure 6. Block Diagram of the Electric System used for the Balance-Noise Tests

The object of the filter is to get rid of undesirable frequencies in the recorder input. The filter has three modes of operations: low pass, band pass, and high pass. Noise being recorded by the recorder come from different sources: natural seismic vibration of the building, vibrations produced by flying air planes or any other moving vehicle close to the building, external or internal air currents, thunderstorms, etc. In order to minimize air currents inside the building, the Braunbeck coil system is provided with a polythylene covering (shroud) that can be placed around the instrument that is under test. As we said before, the main goal of this test was to reduce to a minimum the noise coming from the torque meter due to the above mentioned factors, but mainly to the lack of balance of the torquemeter. As a result of different tests the noise was reduced to a minimum by adding two weights C and D of about 5 pounds each, attached to the upper moving platform of the torquemeter (Figure 5), both dampers full with water and at a band pass frequency of 1.00 Hz as input to the recorder. The test was conducted with no current in the Braunbeck assembly and without energizing the radial and tangential coils and with an applied torque of 681 dyne-cm applied to the torquemeter. This calibrating torque can be applied to the torquemeter by a very delicate balance (bell-crank) in which calibrated weights produced known torques acting along the Z axis of the torquemeter.

SIGNAL TO NOISE RATIO

As it is known, the vibrations of a body under the action of a driving sinusoidal torque $\tau = \tau_0 \sin wt$ obey the differential equation

$$\boxed{I\ddot{x} + c\dot{x} + Kx = \tau_0 \sin \omega t} \qquad (3)$$

which is called the differential equation of a forced rotational oscillation. In this equation

I = Moment of inertia around the axis of rotation

C = Damping Factor

K = Torsional constant

x = Angular deflexion

$\tau = \tau_0$ in wt = applied sinusoidal torque along the axis of rotation.

The corresponding angular deflections are given by

$$x = \frac{x_{ST}}{\sqrt{\left[1 - \left(\frac{f}{f_0}\right)^2\right]^2 + \left[2\frac{c}{c_0}\left(\frac{f_r}{f_0}\right)\right]}} \qquad (4)$$

in which

Xst = constant static deflection under a constant torque and given by Hooke's Law $\tau = KX_{st}$ in which τ is the applied torque and K the torsional constant.

f = Forcing frequency

f_0 = Natural frequency

c = Actual damping factor

c_0 = Critical damping factor

The ratio:

$$\boxed{M F = \frac{X}{X_{st}}} \tag{5}$$

is called the magnification factor, a family of frequency response curves in which MF is plotted versus f/f_0 and c/c_0 is taken as parameter, is shown in Figure 7.

In order to find the signal to noise ratio, the following procedures was followed:

a. Torquemeter balanced and loaded with 400 pounds.

b. Dampers full

c. Calibrating mechanical weight producing a Z axis torque of 681 dyne-cm.

d. A 2 amp current was set in the EW (radial coil) in order to produce a magnetic dipole moment associated with the torquemeter and located in a horizontal plane.

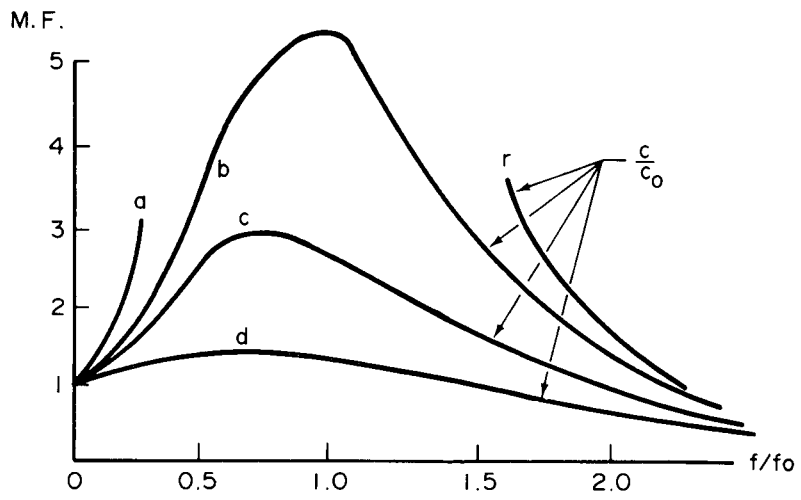

Figure 7. Frequency response curves for different values of c/c_0. a) shows no damping $c/c_0 = 0$, d) shows high damping, b) corresponds to the maximum M.F. at resonance frequency.

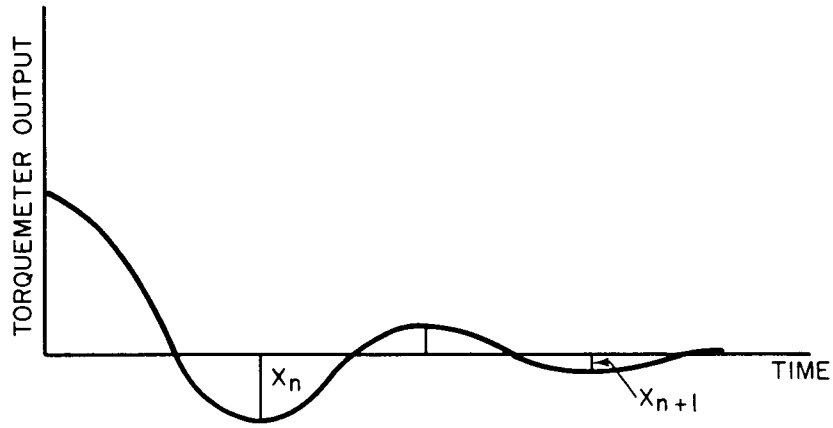

Figure 8. Typical Response in Recorder

e. No magnetic field sets up by the Braunbeck assembly.

f. Geomagnetic field of the earth present.

Under these conditions the current in the E-W coil was suddenly reduced to zero and the output signal was recorded in the dual recorder. A typical curve obtained from the recorder appears in Figure 8.

The main purpose of this operation was to obtain a decay curve from which we obtained the natural frequency as well as the damping c/c_0. This allowed us to "fictionalize" the response to an imaginary input torque signal. This fictional response was then compared to the actual measured noise with the filter set in the band pass mode at the frequencies tabulated (Table I) to obtain the signal to noise ratio.

Several curves were obtained for different frequency inputs to the recorder as set by the filter. Results appear in Table I.

Table I

Torquemeter Responses for Different Frequencies Assuming Torquemeter signal = 1 for f = o and setting arbitrarily $X_{st} = 1$

f(Hz)	Signal X with $X_{st} = 1$	Peak Noise from Recorder	Signal Noise	Relative Signal Noise
0.25	4.20	15	0.28	–
0.283 (f_0)	10.00	17	0.59	2.0
0.50	0.47	8	0.059	0.2
0.75	0.17	3	0.057	0.2
1.00	0.09	2	0.045	0.16
1.25	0.05	3	0.017	0.06
1.50	0.04	3	0.013	0.05

As can be seen, the maximum M.F. = 10 and corresponds to the natural frequency 0.283 Hz of the loaded torquemeter. The natural frequency of oscillation of the torquemeter loaded with 400 pounds was determined experimentally by an analysis of the data obtained from the recorder. The values X/Xst were computed by using the equation:

$$\frac{X}{X_{st}} = \frac{1}{\sqrt{\left[1 - \left(\frac{f}{f_0}\right)^2\right]^2 + \left[2\frac{c}{c_0}\left(\frac{f}{f_0}\right)^2\right]}} \tag{5}$$

In order to find the relative damping c/c_0 (which is necessary to compute the values of X/X_{st} according to $E_g 5$, the ratio c/c_0 must be calculated first. This was done in the following way. It can be proved that if X_n and X_{n+1} (see Figure 8) are two successive peaks in the torquemeter output the following relationship follows for small damping:

$$\delta = \frac{\ell n\, X_x}{X_{n+1}} = 2\pi\frac{c}{c_0} \tag{6}$$

hence:

$$\frac{c}{c_0} = \frac{1}{2\pi}\ell n\frac{X_n}{X_{n+1}}$$

Several values of c/c_0 were computed yielding an average:

$$\frac{c}{c_0} = 0.05$$

The M.F. at resonance is then given by the equation:

$$\boxed{M\,F = \frac{1}{2\frac{c}{c_0}}} \tag{7}$$

Replacing the value $c/c_0 = 0.05$ in equation 7 the result coincides with the result of Table I (second row of table).

Mechanical Calibration of Torquemeter and Correlation with both Air-Coil Dipole moments. Dynamic Calibration of the Air-Coils and Checking their Alignment.

These tests were done in several steps as described here. The first test was done under the following conditions (Figure 5):

a. Torquemeter setup at center of the Braunbeck coil assembly with the Z axis in a vertical position and the radial coil oriented east-west.

b. No current in the Braunbeck coil assembly.

c. Geomagnetics field of the earth present.

d. Applied torques to the torquemeter by means of bell crank device: 681 dyne-cm.

e. Filter in the low pass mode of operation at a cutoff frequency of 1 Hz.

f. Energizing current in the air-coils attached to the torquemeter was 2 amp.

g. Torquemeter load: 400 pounds.

The block diagram of the electrical setup used for this calibration appears in Figure 6. The calibration constant as recorded (average calibration) by the recorder was 32.7 (dyne-cm/div.) at 1 volt/cm sensitivity in the recorder. This calibration was a mechanical calibration of the torquemeter.

The following step was a check of the proper alignment of the air-coils attached to the torquemeter to within 1 degree.

Test was conducted with the torquemeter set as shown in Figure 5. Conditions for this test were as follows (Figure 5):

a. Torquemeter set up at center of Braunbeck coil system and with the Z axis in a vertical position.

b. Dampers full

c. Torquemeter load: 400 pounds.

d. No energizing current in the air-coils attached to the torquemeter.

e. Electrical setup as in Figure 6.

The alignment of the radial coil was performed first under a fixed field of 60K gamma, E-W direction provided by Braunbeck coil assembly. The result was acceptable. The criterion for coil alignment was that the torque produced when the radial coil was energized in the presence of an E-W field does not exceed that due to 1 degree misalignment. The maximum allowance for a 1 degree misalignment of the radial coil was 40 pole-cm.

At this time we also verified the coil constants of both coils (within 5% of the magnetically obtained values) by measuring the torque produced in a known field applied at right angles with a known coil current.

The same alignment test was then performed for the tangential coil under the same conditions as before but with a field of 60K gamma in the N-S direction. The result of this test was also considered as acceptable.

The next step was a dynamic calibration of the torquemeter and correlation with the current in the air-core coils and at the same time a dynamic check on the proper alignment of the air coils.

The setup for the torquemeter in this step is again the same one shown in Figure 5.

The electrical setup is shown in Figure 6.

Test was conducted under the following conditions:

a. Torquemeter setup at center of Braunbeck coil system and with Z axis in a vertical position.

b. Dampers full

c. Torquemeter load: 400 pounds.

d. Current in the air-coils: 2 amp.

e. Filter in the band-pass mode at 0.286 Hz (natural frequency).

The first coil tested was the tangential coil (cal. const. 1958 pole-cm/amp).

An oscillating field (maximum amplitude 60K gamma) oriented in the N-S direction and with a frequency of oscillation of 0.286 Hz was set up by the Braunbeck coil assembly.

The result of this alignment check was: 41 dyne-cm/Amp (approximately 2° misalignment) for the tangential coil. The radial coil was not tested.

The next step was a torque calibration of the air-coils attached to the torquemeter to check the magnetic calibration performed before.

The results of the magnetic calibration were:

Radial Coil K_r = 2349 pole/cm/amp

Tangential Coil K_t = 1958 pole/cm/amp

In order to perform these torquemeter calibrations, the following conditions were followed:

a. Torquemeter setup as in Figure 5.

b. Torquemeter load: 400 pounds.

c. Dampers full

d. Electrical setup as in Figure 6.

The tangential coil was tested first and a 60K gamma (E-W) field was set using the Braunbeck coil assembly. Then the tangential coil was energized with a current of 1 amp and the corresponding deflection in the recorder was measured.

Same procedure was followed in the testing of the radial coil, but with a field of 30K gamma in the N-S direction.

Results from these calibrations were as follows:

a. Radial Coil K_r = 2380 pole/cm/amp

b. Tangential Coil K_t = 1900 pole-cm/amp

The results were considered as acceptable when compared with the former values obtained following the magnetic procedure.

Now a dynamic test was performed whose main purpose was to confirm that the best operational frequency for the SAS-A test was the natural frequency (0.283 Hz).

A block diagram of the electrical setup is snown in Figure 9.

The experimental setup is shown in Figure 5 but adding a fluxgate magnetometer near the center of the Braunbeck coil assembly and whose main purpose was to trigger the averager.

The following conditions were established:

a. Torquemeter set up (Figure 5)

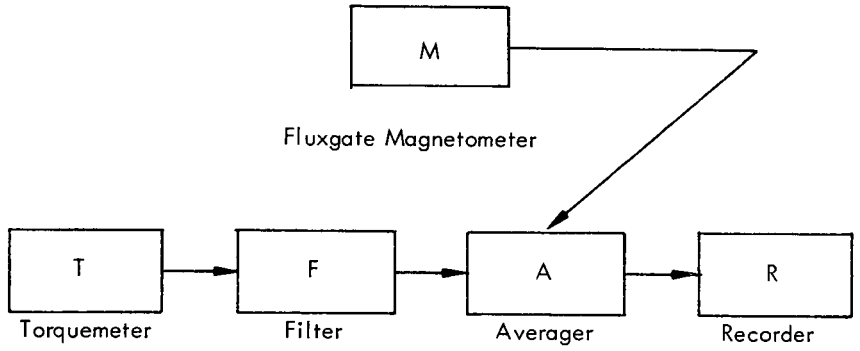

Figure 9. Block Diagram of the Electrical Setup used looking for the optimum Operational Frequency.

b. Flux gate magnetometer near the center of the Braunbeck coil assembly.

c. Torquemeter load: 400 pounds.

d. Filter: band pass mode.

The averager is a sophisticated device whose main purpose is to extract the signal from the noise and as a consequence to improve the signal/noise ratio. This can be done when we have a random background noise and the signal is repetitive periodic or not. It can also extract the signal from the noise when the period of the noise is different from the period of the signal. It has a time disadvantage because you have to wait for a certain number of sweeps before the signal can be extracted with some confidence.

As previously mentioned, the main goal of these tests was to choose the optimum frequency of operation. If the natural frequency of operation was chosen, the peak noise (See Table 1) was a maximum but the magnification factor is the highest. On the other hand operating at 1.00 Hz (Table 1) the noise was minimum but the signal/noise is very small.

A rotational field 0.1 gauss = 10K gamma, angular frequency 0.283 Hz (clockwise) and in a horizontal plane was set by the Braunbeck coil assembly and the radial coil was energized with a current of 0.640 amp. The magnetic dipole moment of the radial coil at this current is:

$$M_r = 2380 \frac{\text{Pole-cm}}{\text{Amp}} = 0.640 \text{ amp.} = 1500 \text{ pole-cm}$$

and the expected peak torque is

$$\tau = \mathfrak{B} M_r = 0.1 \text{ gauss} \times 1500 = 150 \text{ dyne-cm}$$

This torque was considered too high.

Operating the radial coil at 0.064 amp the expected torque is of course $\tau = 15$ dyne-cm so that the output of the averager should be 0.1 of that obtained when operating at 0.640 amp. Actually after 20 sweeps the output was found to be 0.08 rather than 0.1. Next we operated at a frequency of 1.00 Hz, both the filter and the rotational field and

with currents of 0.064 and 0.640 amp in the radial coil. After 80 sweeps the output of the averager at 0.064 amps was only about 0.05 instead of the theoretical value of 0.1. Therefore the best operational frequency was considered to be the natural frequency (0.283 Hz).

5. OBJECTIVES AND BRIEF DESCRIPTION OF THE MAGNETIC TESTING DONE ON THE SAS-A SPACECRAFT

Objectives - The SAS-A satellite is the result of the combined effort of the following organizations:

a. AS&E - a research organization in space exploration and located in Boston, Massachusetts. Responsible for the X-Ray experiment.

b. APL - another research organization stressing also on space exploration and located on Route 29, half-way between Washington, D.C. and Baltimore, Md.

c. The Magnetic Test Site - a branch of NASA/GSFC and whose cooperation in the project has been described before.

d. A private organization located in the Washington area took care of the programming computer assistance for the computer on board of the SAS-A.

The main goal of the SAS-A satellite is to conduct an X-Ray experiment looking for X-Ray sources coming from celestial sources which apparently are located around the equatorial plane. This is the reason for placing the SAS-A in a circular orbit around the equator. If the results of the experiment are satisfactory, the SAS-A will be followed by the SAS-A but looking for gamma sources. Dr. Riccardo Giacommi from AS&E was the principal investigator on the X-Ray experiment. Both SAS-A and SAS-B are not intended to be X-Ray or Gamma-Ray telescopes.

In more detail the scientific objectives of the X-Ray experiment are:

a. To conduct a high sensitivity, high resolution survey of X-Rays sources, that will produce an X-Ray catalogue for sources with intensity greater than approximately 5×10^4 SCOX-1 (the strongest source known at present).

b. To look for time fluctuations in X-Ray intensities over periods of minutes to months. The satellite will be sending information for a period of more than six months.

c. Determination of the spectral distribution of the sources detected in the energy range 1-20 KeV. Weight of the experiment is 150 pounds. That of the spacecraft is about 180 pounds. So the total weight is approximately 330 pounds. See Figure 10 for other details of the SAS-A.

The SAS-A will also keep on board the following facilities:

a. Star Sensor - consists of a lens that focuses light from the stars on a sensitive photomultiplier. Signal output of the photomultiplier will be amplified, transformed into a pulse and processed into telemetry.

b. Solar Sensor - The sun sensor will provide information about sunlight when the star-sensor is not in operation because of proximity of the satellite to the sun-SAS-A line. The sun sensor will also provide attitude information along with three magnetometers on board if the star sensor fails to operate.

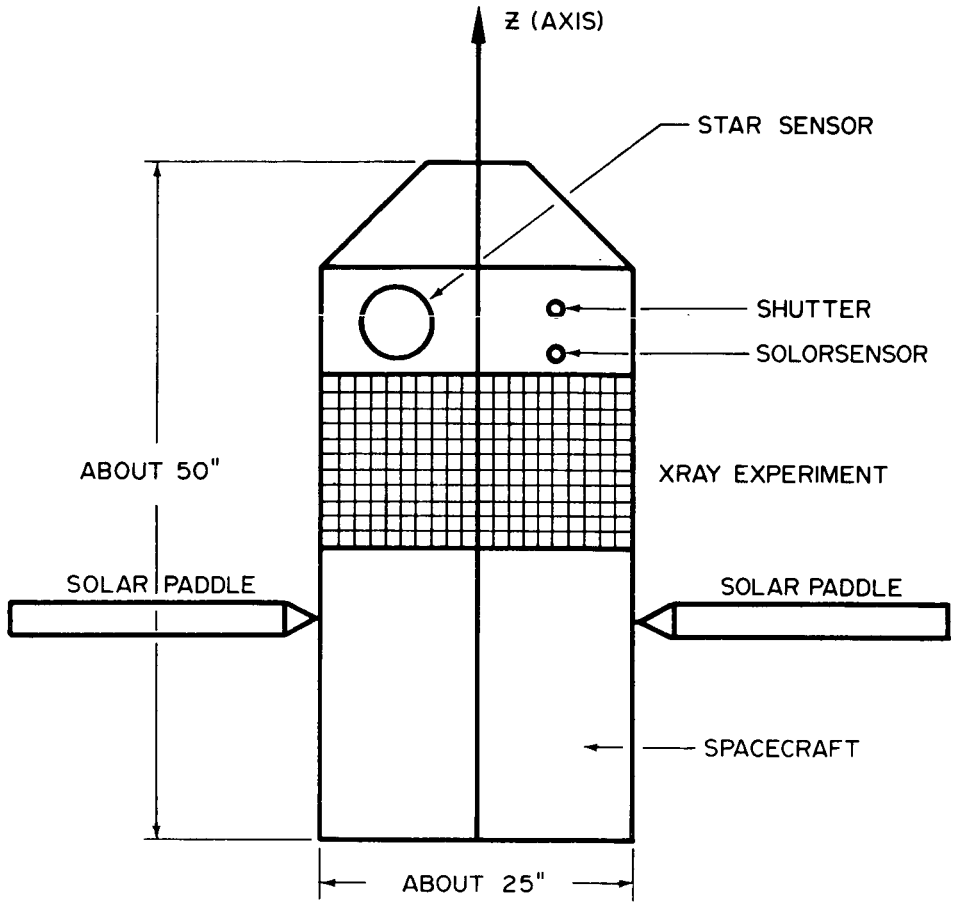

Figure 10. Approximate Longitudinal Crossection of the SAS-A

c. Star Shutter - The main purpose is to protect the photomultiplier's cathode (attached to the star sensor) from light coming from the sun when the star sensor is pointing towards the sun.

d. Power System - The power system is mainly provided from solar cells connected to the solar paddles. There are 4 solar paddles aligned as shown in Figure 10. Only 2 appear in Figure 10. The 2 other solar paddles are also aligned and perpendicular to the ones shown in Figure 10. The paddles have the same length (approximately 6 feet long) and with their axis in a plane perpendicular to the Z axis of the satellite. The cross-section of the SAS-A is circular with its center located at the Z axis.

Coming back to the power system it consists, as we said before, mainly of the solar array, but there are also a nickel cadmium battery (6 amp-hr) and a shunt regulator. Some loads receive power from the main bus and the shunt regulator. Unregulated loads receive power through a DC-DC converter. The logic microcircuits of the command and telemetry systems are powered through a 5 volt regulator. The command system is also provided by another regulator to increase reliability.

When the power system is operating normally the solar array will be sufficient to power the load and charge the battery when it is in the sun light phase of the orbit.

The assembly of the satellite was done at APL research center. F. F. Mobley and B. E. Tossman from the APL staff were in charge of the stage of the process. They were also in charge of the test plan for the SAS-A Pre-Vibration Test. Some innovations were also made by the personnel of APL. For example, the nutation-damper system, whose main purpose is to contribute to the stabilization of the satellite while flying, was designed by B. E. Tossman. J. A. Ford was responsible for the operation of the magnetic-trim system related to the attitude control of the SAS-A. To sum up, APL took care of and designed the proper hardware for attitude and stabilization controls of the satellite.

In addition to the magnetic testing conducted at the Magnetic Test Site (GSFC), the satellite will be submitted to Vibration, Thermal and Mechanical Tests.

The magnetic testing was conducted by personnel of the Magnetic Test Site under supervision of J. C. Boyle (GSFC) and personnel of APL under direction of F. F. Mobley.

The testing was done in the 40 Foot Braunbeck Coil Facility.

A brief description of the Magnetic Testing follows. Data is not included for the following reasons:

a. Data obtained must be reduced, processed and interpreted by personnel of GSFC (Magnetic Test Site) and also by APL.

b. Complete reports on the conclusions of the Magnetic Testing will be prepared by personnel of the Magnetic Test Site and APL, but step a, above, must be conducted first.

c. The total number of magnetic tests was over 200. Evidently a description of the whole process will make this report excessively long.

For those interested in a complete description of the whole procedure, they can be referred to APL Report S2P-2-367, F. F. Mobley and B. E. Tossman.

MAIN STAGES OF THE PRE-VIBRATION MAGNETIC TESTING

The whole procedure was divided into four phases:

Phase 1 - Test-Dipole Moment Measurement by Near-Field Analysis. The goal of this phase was to extract the dipole from the other multipoles associated with the satellite. Reference is made to report X-325-69-350, W. L. Eichhorn (Magnetic Test Site).

Phase 2 - Test-Dipole Moment on the Torque Table. The main goal of this stage was to obtain the dipole-moment associated with the satellite.

Phase 3 - Test-Magnetometer Alignment, Calibration and Investigation of Biases. This phase, that was by far the longest, (2.5 days), was conducted primarily by the APL staff with the assistance of the Magnetic Test Site personnel. The main goals of this phase are explicitly stated in the title.

Phase 4 - Spin-Despin System. This took just 0.5 days and the main goals were:*

*F. F. Mobley, B. E. Tossman, APL Report S2P-2-367

a. Confirm proper torque levels.

b. Check insensitivity to bias field.

GENERAL ADDITIONAL COMMENTS

a. Launching date: About November 1970.

b. Launching Site: Launching Platform, San Marco Island, near Kenya, Africa.

c. Orbit: Circular and Equatorial (300 miles radius).

d. Expected Life Gathering Data: From 6 months to one year.

e. Prime Data Gathering and Command Issuing Station: STADAN "Space Tracking and Data Acquisition Network," Quito, Ecuador, Central America.

f. Inclination of Orbit: 2.9°

g. Spin Rate: 1/12 RPM

h. Period: 96 min.

i. Time Spend on Preparatory Calibration for the SAS-A Pre-Vibration Test: 6 days.

j. Time Spent on Pre-Vibration Magnetic Testing of SAS-A Spacecraft: 7 days.

6. ACKNOWLEDGEMENTS:

The author of this report would like to acknowledge the organizers of this program, Dr. F. P. Emad (University of Maryland) and Dr. J. Morakis (GSFC) for the excellent organization of this Faculty Summer Fellowship. I have really benefited from it, and consider myself really very fortunate in having participated in it. Thanks should be extended to the sponsoring institutions (University of Maryland, Catholic University of America, NASA/GSFC and the ASEE.

Special thanks should be given to C. L. Parson, Head of the Magnetic Test Section, GSFC, for his valuable advice and kind friendship, and to W. G. Brown, Head of the Functional Test Branch, GSFC, for his encouragement and assistance. Also to W. L. Eichhorn, and Tom Roy of the Magnetic Test Site staff, for their excellent collaboration.

Last, but not least, I would like to express my gratitude to J. C. Boyle of the Magnetic Test Site staff, for his continuous dedication, patience, invaluable help, and friendship. Without his assistance and competence, this modest effort would have been impossible.

7. BIBLIOGRAPHY

1. M. Townsend (GSFC), Report on "Project Development Plan (SAS-A)."

2. G. R. Springham (GSFC), Report, "Facility Development plan, Attitude Control Test Facility."

3. Charles A. Harris (GSFC), Report X-325-67-70.

4. J. C. Boyle (GSFC), Report X-325-69-105.

5. J. C. Boyle (GSFC), Report X-325-69-536.

6. L. Page, Theoretical Physics, Second Edition, D.Van Nostrand Co., Inc., New York, N.Y. (1935).

7. A. F. Kip, Fundamentals of Electricity and Magnetism, McGraw-Hill Book Co., New York, N.Y. (1969).

8. D. Halliday and R. Resnick, Physics for Students of Science and Engineering, J. Wiley and Sons, Inc., New York, N.Y. (1964).

STABILITY OF SAS-A DUAL SPIN SPACECRAFT WITH ENERGY DISSIPATION ON THE MOMENTUM WHEEL

Peter M. Bainum
Department of Mechanical Engineering
Howard University
Washington, D. C.

ABSTRACT*

The attitude stability of the SAS-A satellite with damping in the momentum wheel as well as the "despun" portion is analyzed. Wheel energy dissipation is modeled by assuming the wheel can flex with two degrees of freedom relative to the hub. The nonlinear attitude equations are derived for small wheel flexural motion and are a ninth order nonautonomous set. If the main body damper mass and wheel transverse moment of inertia are assumed small when compared with main satellite masses and inertias, an averaging process can be used to determine the zeroth and first order secular perturbations on the behavior of the system nutation angle. From this a general analytic stability criterion is established. A numerical evaluation of this criterion using SAS-A parameters and measured wheel damping data indicates that stability about a zero degree nutation angle is insured by a factor of 128 under normal operating conditions.

This work was published in X-732-70-344.

LI, K, RB, SR, BA AND RARE-EARTH CONCENTRATIONS, AND RB-SR AGE OF LUNAR ROCK 12013

Michale L. Bottino
Department of Geology
Marshall University
Huntington, West Virginia

The bulk of this summer's activity evolved working on lunar samples. The investigation included trace element geochemistry and Rb-Sr geochronology on Apollo 12 soils, rocks, and mineral separates. The trace elements studied were Li, K, Rd, Sr, Ba and the rare-earth elements. In addition, the Sr isotropic composition was measured. My primary area was the Rb-Sr geochronology.

One paper has been accepted and will be published by the end of August in the journal "Earth and Planetary Science Letters." A second, more complete paper will be finished by early fall. This work was done jointly with Drs. Charles C. Schnetzler, Paul D. Fullagar and John A. Philpotts. The introduction and abstract of the paper are reproduced below.

INTRODUCTION

The concentrations of Li, K, Rb, Sr, Ba and nine rare-earth elements (REE) and the isotropic composition of Sr have been determined, by mass spectrometric stable isotope dilution, in a number of fractions of lunar rock 12013, 10. The primary purpose of this paper is to present the data obtained to date, and secondarily discuss some preliminary conclusions and speculations concerning this rock.

Examination of this rock in the Lunar Receiving Laboratory showed that it was quite high in a number of trace elements, and the mineralogy and general chemical composition led the Preliminary Examination Team to the conclusion that it resembled a late-stage basaltic differentiate (1). To a first approximation of this rock is a complicated mixture of light and dark-colored material. Our first analyses of two prepared, homogeneous powders representing these types indicated that some trace elements had markedly different concentrations in the light and dark-colored portions. We therefore decided that analyses of the complete small chips we received would not be as instructive as a study of separated dark and light-colored portions and some mineral concentrates.

ABSTRACT

The light and dark-colored portions of 12013 are characterized by two distinct trace element patterns. The light-colored portions are lower in rate earths, slightly lower in Sr, the same in Li and higher in K, Rb and Ba when compared to the dark-colored portions. The dark material appears to represent a late liquid in the normal igeneous differentiation scheme suggested by the other lunar rocks; the light-colored material may have had a more complex history. Comparisons of trace element abundances of Apollo 12 igneous rocks and 12 soil suggest that the dark material of 12013 may constitute an important component of the soil. The best-fit isochon to nine data points yields a Rb-Sr age of 4.1 + 0.2 b.y. with an initial rate of 0.704 + 0.002.

INFERENCES REGARDING THE CHEMICAL EVOLUTION OF IGENEOUS LUNAR ROCKS

John H. Carman
Geology Department
The University of Iowa
Iowa City, Iowa

A new graphic technique was developed to examine the chemical evolution of igneous lunar rocks. The general components for this technique are the metal (M)-oxygen (0) complexes M_20, M0, M_20_3 and $M0_2$. These components represent a quaternary system in which the bulk of all rocks and minerals may be plotted. For lunar rocks two important exceptions are iron (Fe°) and troilite (FeS). These are both treated as the component M0 which generalizes it to M, M0, MS. Within this general quaternary the mutually exclusive and exhaustive molecular components Kaliophyilite ($KA1Si0_4$), Nepheline ($NaA1Si0_4$) Anorthite ($CaAl_2si_20_8$), the M, M0, MS component and the $M0_2$ ($Si0_2$, $Ti0_2$, $Zr0_2$, etc.) component have been employed. Most of the compositions examined contained Ca0 in excess of that required to constitute anorthite. This excess, signified as "Ca0" was combined with Mg0, Fe0, Ni0, etc. in the M0 component. Only in the case of lunar glasses (interstitual and spheres) and, so called, "anorthosites" was these excess M_20_3, mainly Al_20_3, over the amount necessary to constitute kaliophyilite, nepeline and anorthite. These peraluminous compositions are of special importance in regard to the concentration of trace elements as indicated below.

Projections onto the following component planes, Anorthite + M, M0, MS + $M0_4$, Kaliophyilite + Nepheline + M, M0, MS + $M0_4$, $Ti0_2$ + M, M0, MS + $Si0_2$, Nepheline + $M0_4$ + Kaliophyilite and Fe0 + Mg0 + "Ca0" suggest the conclusions that:

1. The compositional variations of Apollo 11 and 12 igneous rocks (lavas) may be explained on the basis of subtractive - and reactive crystallization in which minor accumulation of early crystals or separation of early formed crystals are the two most important (and opposing) effects. Accumulation or separation of spinel (essentially ulvospinel) and olivine appears to have been important in Apollo 11 samples whereas assumulation or separation of troilite and/or iron and olivine was most important in Apollo 12 samples.

2. There is no evidence that there has been any significant early accumulation or separation of either plagioclase or ilmenite as has previously been inferred to explain the Europium content of these rocks and mascons, respectively.

3. Maria compositions inferred from these two landing sights are very similar in composition and resemble tschermakitic and titaniferous augite cores of Apollo 11 samples. Available data from experimental studies at high pressures and high temperatures suggest that such a pyroxene may be expected to occur in the moon's mantle. Thus it seems that such a pyroxenite mantle may be the best source material for the maria lavas, assuming complete melting of such material during the maria forming stage of lunar evolution. Others have suggested a pyroxenite mantle on the basis of density considerations.

4. The accumulation of troilite and/or iron in Apollo 12 samples suggests that these dense minerals may account for the mascons associated with maria centers. It cannot be ascertained whether or not the iron and sulfur involved in these minerals is primary or metoritic in origin, however it seems apparent that both are

homogeneously distributed within the rocks in which they occur. Significant amounts of iron and troilite were also encountered in the Apollo 11 igneous rocks.

5. The K_2O/Na_2O ratio has been shown to correlate positively with Th, Rb, La, Ce, Ba, Y and Zr. Potassium and these trace elements are known to be concentrated in residual liquids (now interstitual glasses) which commonly line vesicules of these lunar lavas. Analysis of these glasses indicate a surprisingly low sodium content relative to most terrestrial analogs of this type of fractional crystallization in which the glasses approach rhyolite in composition. It is suggested that the low sodium contented of these glasses resulted from a fractionation of sodium into the gas phase during vesiculation and subsequent separation. This loss of sodium enriches these glasses in potassium and the other elements mentioned and if loss is extensive it results in excess Al_2O_3 in the glass's normative composition. In light of the minerals encountered on the moon there is not other known mechanism for obtaining such peraluminous compositions except via the fractionation of alkalis into such a exsolving gas phase or the remelting of lunar rocks and minerals under the near perfect lunar vacuum. Correlation of K_2O/Na_2O with porosity, degree of vesiculation and bulk density, where data are available, suggests that it increases in rocks according to their proximity to the lunar surface during solidification. These observations and deductions indicate that those compositions with low potassium and low trace element abundance more nearly represent primary lunar lavas.

LOSS TANGENT IN CdTe AT 3.7 GHZ

Kenneth H. Carpenter
Physics Department
East Tennessee State University
Johnson City, Tennessee

Frederic M. Davidson
Electrical Engineering Department
University of Houston
Houston, Texas

ABSTRACT

An upper limits was found on the loss tangent (imaginary divided by real part of dielectric coefficient) of CdTe by placing a CdTe crystal in a microwave cavity resonate at 3.7 ghz. The value of loss tangent was less than 0.2 for a newly prepared crystal, but increased to 0.6 after the crystal was subjected to high microwave power. The same results were obtained for a second crystal specimen.

A CdTe crystal of dimensions $3 \times 1 \times 1$ mm was placed inside a microwave resonant cavity in such a manner as to have the microwave electric field directed along the 0,0,1 direction in the crystal–one of the long faces of the crystal. The long dimension of the crystal was the 1,1,0 direction. The entire crystal was situated in the cavity so as to experience essentially the peak microwave electric field. The crystal was supported in the cavity by being placed inside a dielectric tube of glass or teflon inserted across the cavity. The cavity reflection coefficient was measured for frequencies near 3.7 ghz, the resonant frequency, with and without the crystal inside the cavity (but with the support tube always inside the cavity). From these measurements an estimate of the dielectric loss tangent of CdTe can be made at the 3.7 ghz frequency region.

The loss tangent of a lossy dielectric is defined as follows (see: S. Ramo & J. R. Whinnery, Fields and Waves in Modern Radio, 2nd ed., John Wiley & Sons, 1953, p. 309). For loss expressed as imaginary part of dielectric constant, $\epsilon = \epsilon_0 (\epsilon' + j\epsilon'')$, the loss tangent is ϵ'' / ϵ'. Now $\epsilon'' = \sigma / \omega \epsilon_0$ where σ is volume conductivity. A uniform conductor in a uniform electric field of effective (rms) magnitude E has a power dissipation per unit volume of $E^2 \sigma$. If the conducting volume is v, the total power dissipated is $E^2 \sigma v$. The cavity Q is given by

$$Q = 2\pi \frac{\text{peak energy stored}}{\text{energy lost per cycle}}$$

For a rectangular cavity in a 1,1,0 mode we have

$$\text{peak energy stored} = \frac{1}{8} \epsilon_0 \mathcal{E}_{max}^2 V$$

where V is cavity volume and $\mathcal{E}_{max}$ is peak value (in time and space) of electric field in the cavity. Also $\mathcal{E}_{max} = \epsilon' E_{max} = \sqrt{2}\, \epsilon' E$ provided we neglect the distortions in the field

caused by the crystal and its supporting tube. Thus

$$\frac{1}{Q} = \frac{\text{power absorbed} \times \frac{2K}{\omega}}{2\pi \frac{1}{4} \epsilon' \epsilon_0 E^2 V} = \frac{\text{power absorbed} \times \frac{2K}{\omega}}{\frac{1}{4} \omega \epsilon' \epsilon_0 E^2 V}$$

But

$$\frac{1}{Q} = \frac{1}{Q_0} + \frac{1}{Q_{xtal}}$$

or

$$\frac{1}{Q} - \frac{1}{Q_0} = \frac{\sigma v E^2}{\frac{1}{4} \omega \epsilon' \epsilon_0 E^2 V} = \frac{4\sigma}{\omega \epsilon' \epsilon_0} \frac{v}{V}$$

or the loss tangent is

$$\frac{\epsilon''}{\epsilon'} = \frac{\sigma}{\omega \epsilon' \epsilon_0} = \frac{1}{4} \frac{V}{v} \left(\frac{1}{Q} - \frac{1}{Q_0} \right)$$

where Q is cavity quality factor at angular frequency ω with the crystal inside, and Q_0 is the value with the crystal removed. The value of Q was measured by observing variation of reflection coefficient with frequency and hence finding the half power frequencies and thereby Q from $Q = f/\Delta f$. We thus find

$$\frac{\epsilon''}{\epsilon} = \frac{1}{4} \frac{V}{v} \frac{1}{f} \left[(\Delta f)_{xtal} - (\Delta f)_0 \right]$$

Two essentially identical CdTe crystals were supplied by James Keifer of Hughes Aircraft Company. The loss tangent was measured for one of the crystals in the condition in which it was received. Both crystals were used in a laser modulation experiment during which they were subjected to microwave powers on the order of one to less than ten watts. During this time the loss tangent increased significantly. Measurement of the loss tangent for each of the crystals following the application of high power showed essentially the same loss tangent, which was at least three times the initial value.

Application of the formula for loss tangent to the crystals as received is difficult since loss in the tube used for support was much greater than in the crystal. Hence change in Δf was less than the accuracy with which Δf was determined. Assuming a ten percent accuracy in Δf, we can bound the loss tanget in the new crystal as

$$\frac{\epsilon''}{\epsilon'} < 0.1 \left(\frac{1}{4} \frac{V}{v} \right) \frac{1}{Q}$$

The numerical values are

$$v = 1 \times 1 \times 3 \times (10^{-3})^3 \text{ m}^3$$

$$V = 2.5 \times 5 \times 5 \times (10^{-2})^3 \text{ m}^3$$

$$\frac{1}{4}\,\frac{V}{v} = 5.2 \times 10^3$$

$$Q \approx 2 \times 10^3$$

Hence

$$\frac{\epsilon''}{\epsilon'} < 0.1 \times \frac{5 \times 10^3}{2 \times 10^3} \approx 0.2.$$

After the crystal had been irreversibly damaged when between one and ten watts of power was incident on it, the losses were increased and measurements gave $F f_0 \approx 1.7$ mhz and $\Delta f_{xtal} \approx 2.1$ mhz at f = 3.7 ghz. Thus

$$\frac{\epsilon''}{\epsilon'} \approx \frac{5.2 \times 10^3}{3.7 \times 10^9} [2.1 - 1.7] \times 10^6 = 0.6$$

Thus the loss tangent had been increased by at least a factor of three, and probably much more, by whatever mechanism resulted when high fields and, or temperatures were reached by the crystals.

INTERNAL MODULATION OF SINGLE MODE LASERS AT FREQUENCIES EXCEEDING OPTICAL CAVITY LINE-WIDTH

Kenneth H. Carpenter
Physics Department
East Tennessee State University
Johnson City, Tennessee

Frederick M. Davidson
Electrical Engineering Department
University of Houston
Houston, Texas

ABSTRACT

Mode coupling in an optical resonant cavity is examined from the viewpoint of modulation of a single mode laser. It is shown that an intercavity modulator can achieve enchancement of the modulation index over external modulation by a factor on the order of the passive Q of the cavity. Such internal modulation may be achieved over bandswidths exceeding that of a single resonator mode by coding the modulating singal into frequency bands about successively higher resonant modes.

Amplitude modulation of laser beams through the use of external modulators has been reported at various frequencies up to several gigahertz.[1,2,3,4] Internal modulation of single mode lasers, either AM or FM for information coding purposes, has generally been limited to frequencies less than the optical cavity line width of a few hundred megacycles. The use of internal modulation techniques is preferred because a lower modulator drive power is required for a given power in the sidebands. Hence it is desirable to extend internal modulation techniques to larger bandwidths than that of a single optical cavity mode. In the following we will consider internal modulation in an optical resonator from a mode coupling viewpoint, and will derive an expression for the modulation index which explicitly shows modulation is enhanced over external modulation by the Q of the resonator.

GENERAL EQUATIONS FOR INTERNAL LASER MODULATION

Internal modulation of a laser can be understood from the viewpoint of mode coupling in a resonator. This problem has been extensively studied by Yariv and others.[5,6,7,8] In the following we use the method and notation of Yariv[5], corrected and adapted as necessary to fit our application.

First, we define for the optical resonator (cavity) the orthonomal sets of vector functions $\bar{E}_a(\bar{r})$ and $\bar{H}_a(\bar{r})$ satisfying

$$k_a \bar{E}_a = \nabla \times \bar{H}_a, \; k_a \bar{H}_a = \nabla \times \bar{E}_a \tag{1}$$

$$\nabla \cdot \bar{E}_0 = \nabla \cdot \bar{H}_a = 0 \tag{2}$$

and the boundary condition $\bar{n} \times \bar{E}_a = 0$. Orthonormality implies

$$\int_{V_c} \bar{E}_a \cdot \bar{E}_b \, dv = \int_{V_c} \bar{H}_a \cdot \bar{H}_b \, dv = \delta_{ab} \tag{3}$$

Either set $\bar{E}_a$ or set $\bar{H}_a$ is complete for expansion of a vector field in the cavity that satisfies the same boundary condition as $\bar{E}_a$ or $\bar{H}_a$. Now for an optical cavity with walls of perfect conductors the electric field vector satisfies the $\bar{n} \times \bar{E} = 0$ boundary condition. We will assume this is the case to a good approximation and account for actual losses in the walls by a fictitious contribution to volume conductivity. Hence, we expand the electromagnetic fields inside the optical resonant cavity as

$$\bar{E}(\bar{r}, t) = -\sum_a \frac{1}{\sqrt{\epsilon}} p_a(t) \bar{E}_a(\bar{r}) \tag{4}$$

$$\bar{H}(\bar{r}, t) = \sum_a \frac{1}{\sqrt{\mu}} \omega_a q_a(t) \bar{H}_a(\bar{r}) \tag{5}$$

where ϵ and μ are the effective homogeneous constant total permeability and permittivity with the modulator present in the cavity but with no drive to the modulator.* By definition, $\omega_a = k_a / \sqrt{\mu\epsilon}$, and, for example, in a Fabry-Perot interferometer of length L, $k_a = \pi n_a / L$.

Next we use Maxwell's equations

$$\nabla \times \bar{E} = -\mu \frac{\partial \bar{H}}{\partial t} \tag{6}$$

$$\nabla \times \bar{H} = \bar{J} + \frac{\partial}{\partial t} [\epsilon(\bar{r}, t) \bar{E}(\bar{r}, t)] \tag{7}$$

with expansions (4) and (5) to show

$$p_a(t) = \frac{d}{dt} [q_a(t)] \tag{8}$$

and

$$\sum_b \left\{ \omega_b^2 q_b + \frac{\sigma_b(r, t)}{\epsilon} p_b + \frac{\partial}{\partial t} \left[\frac{\epsilon(\bar{r}, t) p_b}{\epsilon} \right] \right\} E_b(\bar{r}) = 0 \tag{9}$$

*When the modulator does not fill the entire cavity the static ϵ is not homogeneous. However, the net effect is that of a homogeneous ϵ of appropriate value since static inhomogeneities do not couple modes.

where we have expanded current density as

$$\bar{J} = -\sum_a \frac{\sigma_a p_a \bar{E}_a}{\sqrt{\epsilon}} \tag{10}$$

Now

$$\frac{\sigma_b(\bar{r}, t)}{\epsilon} = \frac{\omega_b}{Q_b} + \frac{\sigma_{1b}(\bar{r}, t)}{\epsilon} \tag{11}$$

with Q_b being the total effective Q of the resonator in mode b in the absence of modulator drive (including losses due to finite conductivity walls, output coupling, and constant volume conductivity) and σ_1 being the time varying conductivity induced by modulator drive. Also we define $\epsilon_1(\bar{r}, t)$ by

$$\epsilon(\bar{r}, t) = \epsilon + \epsilon_{1b}(\bar{r}, t). \tag{12}$$

The b subscript is placed on ϵ_{1b} and σ_{1b} in (11) and (12) to indicate that if the modulator medium is dependent on optical frequency, then in each mode of the expansion in (9), ϵ_1 or σ_1 must be evaluated at the actual frequency present in the mode bandwidth. Thus on taking a scalar product of Eq. (9) with $\bar{E}_a$ and integrating over the cavity volume we find

$$\dot{p}_a + \frac{\omega_a}{Q_a} p_a + \omega_a^2 q_a = \sum_a \{R_{ab} p_b + S_{ab} \dot{p}_b\} \tag{13}$$

where

$$S_{ab} = \frac{1}{\epsilon} \int_{V_c} \epsilon_{1b}(\bar{r}, t)\, \bar{E}_a \cdot \bar{E}_b \, dv \tag{14}$$

and

$$R_{ab} = \frac{d}{dt}(S_{ab}) + \frac{1}{\epsilon} \int_{V_c} \sigma_{1b}(\bar{r}, t)\, \bar{E}_a \cdot \bar{E}_b \, dv \tag{15}*$$

Equations (8), (13), (14) and (15) form the general basis for mode coupling in a resonator due to internal modulation. We next specialize to the case of sinusoidal modulation of a single mode laser and proceed to solve the resulting equations. In order to obtain the solution the following assumptions are made:

---

*The effect of loss in a dielectric at optical frequencies is often stated by giving an imaginary part to $\epsilon(\bar{r}, t)$. This follows from an assumption of a single frequency complex form for $\bar{E}(\bar{r}, t) = C e^{j\omega t}$ and from the time derivative operator in Maxwell's equations yielding a factor $j\omega$. Thus when a complex $[\epsilon(\bar{r}, t)$ is given one must use Re $[\epsilon_1(\bar{r}, t)$ for $\epsilon_1(\bar{r}, t)$ in Eq. (14) and use ω Im $[\epsilon_1(\bar{r}, t)$ for $\sigma_1(\bar{r}, t)$ in (15).

1. $S_{ab} = S^0_{ab} \sin v\,t = -\frac{1}{2} j\, S^0_{ab} (e^{jvt} - e^{-jvt})$ (16)

2. $R_{ab}(t) = R^0_{ab} \cos (v\,t + Q) = \frac{1}{2} R^0_{ab} (e^{j(vt+Q)} + e^{-j(vt+Q)})$ (17)

3. The single mode laser oscillation is on mode a = L and has constant amplitude, $q_L(t) = A \cos \omega_L\, t$ (18)

4. The upper sideband frequency $(\omega_L + v)$ lies within the pass band of mode a = u, i.e., $\omega_L + v$ falls in $\omega_u (1 \pm 1/Q_u)$, and all other possible frequency components, e.g., $\omega_L - v$, ω_L, $\omega_L \pm 2v$, etc. lie outside $\omega_u (1 \pm 1/Q_u)$. The corresponding assumption is made for the lower sideband in mode a = ℓ.

Using these assumptions we proceed to specialize the differential equation for the upper sideband mode. First we eliminate p_a from (13) with (8) and then write (8) for a = u to obtain

$$\ddot{q}_u + \frac{\omega_u}{Q_u} \dot{q} + \omega_u^2 q_u = R_{uL} \dot{q}_L + S_{uL} \ddot{q}_L + R_{uu} \dot{q}_u + S_{uu} \ddot{q}_u + R_{u\ell} \dot{q}_\ell + S_{u\ell} \ddot{q}_\ell \tag{19}$$

With the assumed values of q_L, R_{ab}, S_{ab} we have

$$\begin{aligned} \ddot{q}_u + \frac{\omega_u}{Q_u} \dot{q}_u + \omega_u^2 q_u = &- A \omega_L R^0_{uL} \cos (v\,t + Q) \sin \omega_L\, t \\ &- A \omega_L^2 S^0_{uL} \sin v\,t \cos \omega_2\, t \\ &+ \text{terms involving } \sin v\,t \text{ or } \cos v\,t \text{ times } \sin (\omega_2 t\, v)\, t \text{ or } \cos \omega_2\, t\, v)\, t \end{aligned} \tag{20}$$

By assumption 4 above the only driving terms on the right of (20) that need be retained are those of frequency $(\omega_L + v)$. Hence we may approximate (20) by

$$\begin{aligned} &\ddot{q}_u + \frac{\omega_u}{Q_u} \dot{q}_u + \omega_u^2 q_u \\ &= -\frac{1}{2} A \omega_L \{\omega_L S^0_{uL} \sin [(\omega_L + v)] + R^0_{uL} \sin \{(\omega_L + v)\, t + Q]\} \end{aligned} \tag{21}$$

Equation (21) is the standard driven harmonic oscillator with the solution

$$q_u(t) = \frac{A G \sin [(\omega_L + v)\, t + \psi]}{\left\{[(\omega_L + v)^2 - \omega_u^2]^2 + \frac{(\omega_L + v)^2 \omega_u^2}{Q_u^2}\right\}^{1/2}} \tag{22}$$

where

$$G = \frac{1}{2}\,\omega_L \left\{\omega_L^2 \,(S_{uL}^0)^2 + (R_{uL}^0)^2 + 2\,\omega_L\, S_{uL}^0\, R_{uL}^0 \cos\phi\right\}^{1/2} \tag{23}$$

and

$$\psi = \tan^{-1}\left(\frac{R_{uL}^0 \sin\phi}{R_{uL}^0 \cos\phi + \omega_L\, S_{uL}^0}\right) + \tan^{-1}\left(\frac{(\omega_L + v)\,\omega_u}{Q_u\,([\omega_u + v]^2 - \omega_u^2)}\right) \tag{24}$$

Details of this solution are given in Appendix A.

The ratio of electric or magnetic field strength magnitude at the upper sideband to that of the carrier (laser oscillation) may now be calculated. From (5) and (22) this ratio is

$$M_{uL} = \frac{\omega_u}{\omega_L}\, G \left\{\left[(\omega_L + v)^2 - \omega_u^2\right]^2 + \frac{(\omega_L + v)^2\,\omega_u^2}{Q_u^2}\right\}^{-1/2} \tag{25}$$

Using G from (23) we find

$$M_{uL} = \frac{\frac{1}{2}\,Q_u \sqrt{\left(\frac{R_{uL}^0}{\omega_L}\right)^2 + (S_{uL}^0)^2 + 2\left(\frac{R_{uL}^0}{\omega_L}\right) S_{uL}^0 \cos\phi}}{\sqrt{\left(1 + \frac{v}{\omega_2}\right)^2 + Q_u^2\left[\frac{\omega_u^2 - (\omega_L + v)^2}{\omega_u\,\omega_L}\right]^2}} \tag{26}$$

The value of M_{uL} in (26) gives the ratio of field strengths inside the laser cavity. To find the ratio outside we must multiply by the ratio of output coupling for the two modes. In (26), Q_u is the total effective Q for mode u including the effect of losses in the modulator. Thus the ratio of field strengths outside the cavity will not be $Q_u/Q_u\, M_{uL}$ because the Q_u and Q_L values include losses other than coupling. Instead we can write for the ratio of field strengths outside the laser $m_{u\ell_0} = m_{uL}\,(t_u/t_L)$ where t_a is the transmission coefficient of the output mirror at the appropriate frequency.

Essentially identical results will be obtained for the lower sideband by substituting the appropriate values into Eq. (26).

DISCUSSION OF INTERNAL MODULATION

The expression for resultant modulation index for internal modulation given in Eq. (26) shows the advantages to be achieved by this method of modulation. First, we should note that at the center of the cavity mode, $\omega_u = \omega_L + v$, the ratio of power in the upper sideband to power in the carrier in the external beam is

$$m_{u\ell_0}^2 = \frac{1}{4}\,Q_u^2 \left(\frac{t_a}{t_L}\right)^2 \left\{\left(\frac{R_{uL}^0}{\omega_L}\right)^2 + (S_{uL}^0)^2 + 2\,\frac{R_{uL}^0}{\omega_L}\, S_{uL}^0 \cos\phi\right\} \tag{27}$$

The significance of this ratio is in the presence of the factor Q_u^2 which can be quite large for an optical resonator. However, for loss modulation, $\sigma(\bar{r}, t) \neq 0$, the effective Q_u could be small if there are a D.C. (unmodulated) component of $\sigma(\bar{r}, t)$ at the uppersideband frequency. Hence, if the enhancement of modulation due to presence of the resonator is to occur with loss modulation the loss mechanism must be frequency dependent and losses must be confirmed to a band containing ω_L but not containing $\omega_L + \nu$. In fact, when the modulation index is calculated assuming a frequency independent loss mechanism the factor of Q cancels in the result. From this argument we see that the Q_u^2 factor in (27) enhances the sideband power significantly (i.e., by a factor of 10^8 to 10^{10}) over that obtained by external modulation with the same modulator and modulator drive provided the modulator losses are low at the sideband frequencies. The method should therefore be useful for both Stark effect loss modulation,[9,10] and for electro-optic modulation of $\epsilon(\bar{r}, t)$ when the electro-optic modulator is oriented so as not to produce losses due to polarization effects.

Although internal modulation enhances the modulation index by the resonator Q when the sideband frequency falls on a resonator mode center frequency, for other sideband frequencies the modulation is reduced by the factors in the denominator of Eq. (26) in the manner of a second order resonant circuit with quality factor Q_u and center frequency ω_u. Thus in a given mode of the resonator the bandwidth of modulation frequencies that can be used is ω_u/Q_u and the enhancement of the gain-bandwidth product for the modulation is $Q_u(\omega_u/Q_u) = \omega_u$ and is independent of Q_u. Hence in this sense no enhancement is achieved by internal modulation over external. But, with high Q, the bandwidth limitation on internal modulation may be circumvented by coding of information to place the modulation frequencies in successive bands of width ω/Q at successive resonator modes, thereby achieving both unlimited bandwidth and the enhancement of modulation by Q. Thus internal modulation appears attractive for gigahertz frequencies where modulators are inefficient without such an enhancement.

One may foresee problems with maintaining stable laser oscillations with an intercavity modulator, particularly a loss modulator. However, the derivations above will apply equally as well to the case where the modulator is placed in a separate optical resonator from the laser resonator thereby isolating the modulator from the active medium. (This would also be necessary if the active medium has gain at sideband frequencies if distortion is to be avoided.)

In summary, one may achieve an enhancement of laser amplitude modulation by the Q factor of an optical resonator by placing the modulator inside the resonator (provided the resonator Q at the sideband frequencies is not significantly degraded by the modulator). Such internal modulation may be achieved over bandwidths exceeding that of a single resonator mode by coding the modulating signal into frequency bands about successively higher resonator modes. Thus it should be possible to achieve gigahertz and higher modulation of lasers with internal modulators.

REFERENCES

1. Riesz, R. P., and M. R. Biazzo: Gigahertz Optical Modulation. Applied Optics, Vol. 8, No. 7, July 1969, pp. 1393-1396.

2. Chow, K. K., R. L. Comstock, W. B. Leonard: 1.5 - GHz Bandwidth Light Modulator, IEEE Journal of Quantum Electronics (Correspondence), Vol. QE-5, No. 12, Dec. 1966, pp. 618-620.

3. Auth, D. C.: Half-Octave Bandwidth Traveling - Wave X-Band Optical Phase Modulator. IEEE Journal of Quantum Electronics (Correspondence) Vol. QE-5, No. 12, Dec. 1966, pp. 622-623.

4. Brand, H., B. Hill, E. Holtz, G. Wencker: External Light Modulation with Low Microwave Power. Electronics Letters, Vol. 2, No. 8, Aug. 1966, pp. 317-318.

5. Yariv, A.: Parametric Interactions of Optical Modes. IEEE Journal of Quantum Electronics, Vol. QE-2, No. 2, Feb. 1966, pp. 30-37.

6. Yariv, A.: Internal Modulation in Multimode Laser Oscillators. Journal of Applied Physics, Vol. 36, No. 2 Feb. 1965, pp. 388-391.

7. DiDomenico, M.: Small-Signal Analysis of Internal (Coupling-Type) Modulation of Lasers. Journal of Applied Physics, Vol. 35, No. 10, Oct. 1964, pp. 2870-2876.

8. Louisell, W. H.: Coupled Modes and Parametric Electronics. New York, Wiley, 1960.

9. Landman, A., H. Marantz, and V. Early: Light Modulation by Means of the Stark Effect in Molecular Gases - Application to CO Lasers. Applied Physics Letters, Vol. 15, No. 11, 1 Dec. 1969, pp. 357-360.

10. Claspy, P. C. and Yoh-HanPao: High Frequency Modulation of the CO Laser Using the Stark Effect in Molecular Gases.

APPENDIX A

Details of solution of driven harmonic oscillator differential equation. Solution of (21):

$$\text{Consider} \quad \ddot{q} + \frac{\omega}{Q}\dot{q} + \omega^2 q = \alpha \sin \omega' t + \beta \cos \omega' t. \tag{A1}$$

$$\left.\begin{aligned} &\text{Assume} \quad q = A \sin \omega' t + B \cos \omega' t \\ &\text{Then} \quad \dot{q} = \omega' A \cos \omega' t - \omega' B \sin \omega' t, \; \ddot{q} = -\omega'^2 q \end{aligned}\right\} \tag{A2}$$

Substitution of (A2) in (A1) gives

$$(\omega^2 - \omega'^2)(A \sin \omega' t + B \cos \omega' t) + \frac{\omega \omega'}{A}(-B \sin \omega' t + A \cos \omega' t) = \alpha \sin \omega' t + \beta \cos \omega' t$$

which on equating coefficients of cos $\omega' t$ and sin $\omega' t$ yields

$$\begin{bmatrix} (\omega^2 - \omega'^2) & -\frac{\omega \omega'}{Q} \\ \frac{\omega \omega'}{Q} & (\omega^2 - \omega'^2) \end{bmatrix} \begin{bmatrix} A \\ B \end{bmatrix} = \begin{pmatrix} \alpha \\ \beta \end{pmatrix} \tag{A3}$$

or on inverting the matrix

$$\begin{pmatrix} A \\ B \end{pmatrix} = \frac{1}{\Delta} \begin{bmatrix} (\omega^2 - \omega'^2) & \frac{\omega \omega'}{Q} \\ -\frac{\omega \omega'}{Q} & (\omega^2 - \omega'^2) \end{bmatrix} \begin{pmatrix} \alpha \\ \beta \end{pmatrix}$$

$$\Delta = (\omega^2 - \omega'^2)^2 + \left(\frac{\omega \omega'}{Q}\right)^2$$

$$\frac{B}{A} = \frac{-\frac{\omega \omega'}{Q}\alpha + (\omega^2 - \omega'^2) B}{(\omega^2 - \omega'^2)\alpha + \frac{\omega \omega'}{Q}\beta}$$

$$A^2 + B^2 = \frac{1}{\Delta^2}(\alpha \; \beta) \begin{pmatrix} (\omega^2 - \omega'^2) & -\frac{\omega \omega'}{Q} \\ \frac{\omega \omega'}{Q} & (\omega^2 - \omega'^2) \end{pmatrix} \begin{pmatrix} (\omega^2 - \omega'^2) & \frac{\omega \omega'}{Q} \\ -\frac{\omega \omega'}{Q} & (\omega^2 - \omega'^2) \end{pmatrix} \begin{pmatrix} \alpha \\ \beta \end{pmatrix} \tag{A4}$$

$$= \frac{1}{\Delta^2}(\alpha \; \beta) \begin{pmatrix} \Delta & 0 & \alpha \\ 0 & \Delta & \beta \end{pmatrix} = \frac{\alpha^2 + \beta^2}{\Delta}$$

Next we substitute the appropriate values for ω, ω', α, β for Eq. (21) to find G, ψ of (23) (24):

$$\alpha = -\frac{1}{2} A \left[\omega_L S^0_{uL} + R^0_{uL} \cos\phi\right] \quad \beta = -\frac{1}{2} A \omega_L R^0_{uL} \sin\phi$$

$$\alpha^2 + \beta^2 = \frac{1}{4} A^2 \omega_L^2 \left\{\omega_L^2 (S^0_{uL})^2 + (R^0_{uL})^2 + 2 \omega_L S^0_{uL} R^0_{uL} \cos\phi\right\} \tag{A5}$$

$$\frac{B}{A} = -\frac{-(\omega_L + v)\,\omega_u \left[\omega_L S^0_{uL} + R^0_{uL} \cos\phi\right] + Q_u \left[\omega_u^2 - (\omega_L + v)^2\right] R^0_{uL} \sin\phi}{+ Q_u \left[\omega_u^2 - (\omega_2 + v)^2\right] \left[\omega_L S^0_{uL} + R^0_{uL} \cos\phi\right] + (\omega_L + v)\,\omega_u R^0_{uL} \sin\phi}$$

Since $\tan\psi = B/A$ we may write

$$\tan\psi = \frac{\dfrac{R^0_{uL} \sin\phi}{\omega_2 S^0_{uL} + R^0_{uL} \cos\phi} + \dfrac{(\omega_L + v)\,\omega_u}{Q_u \left[(\omega_L + v)^2 - \omega_0^2\right]}}{1 - \left(\dfrac{R^0_{uL} \sin\phi}{\omega_L S^0_{uL} + R^0_{uL} \cos\phi}\right)\left(\dfrac{(\omega_2 + v)\,\omega_u}{Q_u \left[(\omega_2 + v)^2 - \omega_u^2\right]}\right)} \tag{A6}$$

and use the trigonometric identity

$$\tan(A + B) = \frac{\tan A + \tan B}{1 - \tan A + \tan B}$$

to obtain (24) from (A6). Eqs. (22) and (23) follow at once from (A4) and (A5).

EVALUATION OF COMPUTER STRUCTURES FOR THE STADAN AUTOMATED DATA HANDLING AND CONTROL SYSTEM

Stephen W. Ching
Department of Electrical Engineering
Villanova University
Villanova, Pennsylvania

This summer I am working in the evaluation of computer structures for the STADAN automated data handling and control system. My GSFC associate is Mr. John C. Rodgers.

The STADAN automated data handling and control (STADAC) system is an automated system consisting of special purpose hardware, computers and system softwares planned for more effectively perform data handling, station operation and equipment control at the remote station of the world-wide space tracking and data acquisition network (STADAN). The need for evaluation of computer structures arises initially when the need for a computer facility is determined. The need for evaluation is never satisfied completely thereafter. The plans for implementing a computer facility at the remote station of a space tracking and data acquisition network involve the following basic question: "What kind of computer configuration is required to perform the anticipated data handling and system control task within a required response time?" It is clear that many different computer configurations could satisfy the STADAC requirements. The objective then, is to determine which computer configuration is optimal. The optimal computer structure of STADAC must be considered relative to the six STADAC functional subsystems such as data handling subsystem (DHS), schedule display subsystem (SDS), equipment status reporting subsystem (ESRS), equipment set-up and control subsystem (ESCS), link control monitor subsystem (LCMS) and link readiness and verification subsystem (LRVS). In order to make a meaningful evaluation of various computer configurations, standard measures of system capabilities must be employed. Some of the measures related to the STADAC requirements are turn-around-time, throughout, cost, system reliability and the combination of these factors. Throughout of STADAC system is measured in time units as the capability of the system to accept data from orbiting spacecrafts and transmitting the data back to GSFC.

A detailed study of STADAC functional subsystems revealed the following computer structure characteristics;

1. The major computer design crtieria will be optimal (effective) use of available communication and control interfaces. The system will be classified as a communication and control computer and will be capable of handling mass data base.

2. The system will be controlled primarily by data rather than by program.

3. Use of hardware to govern communication and control interface will be emphasized; microprogramming facility is highly recommended.

4. Most processing will be executed in real time.

5. The system will be readily expandable. Hardware and software will be modular in design. Computing power will be modified without redesign of the system.

6. The operating system will be designed to operate efficiently. The system will include an analysis of I/0 buffering requirement, page characteristics or memory fragmentation, time slicing algorithms for multiprogramming, quening disciplines as applied to scheduling and dynamic allocation of system resources.

Three kinds of computer configuration are considered in this evaluation. The first configuration is a dual processors multi-link computer system which contains a data-handling central processor unit and a station control CPU. A second configuration is a link-oriented design using mini-computers. Array computer with micro-facility is then considered. Evaluation results of the above computer configurations will appear in my final technical report.

MODULATION OF A CO_2 LASER AT GIGACYCLE FREQUENCIES – EXPERIMENTAL RESULTS

Frederic M. Davidson
Electrical Engineering Department
University of Houston
Houston, Texas

Kenneth H. Carpenter
Physics Department
East Tennessee State University
Johnson City, Tennessee

Nelson McAvoy
Goddard Space Flight Center
Greenbelt, Maryland

I. INTRODUCTION

Modulation of a CW CO_2 laser at gigacycle modulating frequencies was attempted in two ways. The first was through the use of a crystal that exhibits a linear electro-optic effective, i.e., on that has an index of refraction that can be varied linearly with applied electric field strength. The second method involved the use of a gas cell modulator containing a gas that exhibits a Stark Effect energy level splitting for energy levels that give rise to absorption lines in the 10.6 micrometer band of CO_2 laser transitions. Theoretical considerations for both types of modulation will not be considered here, but a general theoretical discussion of laser modulation techniques can be found in the section of this report entitled "Internal Modulation of Single Mode Lasers at Frequencies Exceeding Optical Cavity Line-Width."

II. LINEAR ELECTRO-OPTIC EFFECT MODULATOR

Modulation of CW visible laser beams at gigacycle frequencies has been demonstrated with the use of Li $Nb0_3^1$ and also with KDP [2]. Modulation of a CW CO_2 laser at 10.6 micrometers has been accomplished with the use of GaAs [3]. It was the purpose of this investigation to attempt modulation of 10.6 micrometer radiation with the use of CdTe since it has a larger electro-optic coefficient than GaAs and hence would require less modulator power to achieve the same depth of modulation[4].

Two crystals of CdTe, approximately 1 mm × 1 mm × 3 mm, were obtained from the Hughes Aircraft Corporation. CdTe belongs to the 43 m crystal symmetry class and is a cubic crystal. The linear variations of $(1/\eta^2)_i$ with applied electric field is described by the electrooptic tensor[5] where i = 1, 2, 3, 4, 5, 6, and j = 1, 2, 3.

$$\Delta\left(\frac{1}{\eta^2}\right)_i = r_{ij} E_j$$

Repeated indices are to be summed over are respectively

$$2\left(\frac{1}{\eta^2}\right)_4, \quad 2\left(\frac{1}{\eta^2}\right)_5, \quad \text{and} \quad 2\left(\frac{1}{\eta^2}\right)_6.$$

The coefficients of the yz, xz, xy of the index ellipsoid written in a nonprincipal coordinate system. Since the crystal is cubic, the coefficients of the X^2, Y^2, and Z^2 terms of the index ellipsoid are equal and may be denoted by $1/\eta_0^2$. The electrooptic tensor for 43 m symmetry class crystals is of the form

$$\begin{pmatrix} 0 & 0 & 0 & r_{41} & 0 & 0 \\ 0 & 0 & 0 & 0 & r_{41} & 0 \\ 0 & 0 & 0 & 0 & 0 & r_{41} \end{pmatrix}$$

CdTe has a value of $r_{41} = 5.7 \times 10^{-12}$ meters/volt.

The crystals were cut so that their long axis corresponded to the [110] crystal direction, and two of the long parallel faces corresponded to planes perpendicular to the [001] crystal direction. The orientation of the optical field electric vector with respect to the modulating r-f electric field vector is determined by finding in which direction the maximum change of index of refraction with applied electric field occurs. This is found by finding the intersection ellipse between the plane through the origin perpendicular to the direction of propagation of the optical field and the index ellipsoid. To obtain maximum modulation the optical field should propagate along the long crystal axis. The r-f modulating field can conveniently be applied along the z direction [001] crystal direction. The changes of the index of refraction with applied electric field are consquently determined by the intersection of the plane

$$X + Y = 0$$

and the index ellipsoid

$$\frac{X^2 + Y^2 + Z^2}{\eta_0^2} + 2\, r_{41}\, E_z\, x\, y = 1$$

The intersection ellipse is given by

$$\frac{2\, y^2}{\eta_0^2}\,(1 - r_{41}\, E_z\, \eta_0^2\,) + \frac{Z^2}{\eta_0^2} = 1$$

or by

$$\frac{2\, X^2}{\eta_0^2}\,(1 - r_{41}\, E_z\, \eta_0^2) + Z^2/\eta_0^2 = 1$$

Hence modulation results only for the X and Y components of the optical electric field, and the change in the index of refraction in the X or Y direction is given by

$$\Delta \eta = \frac{1}{4}\, \eta_0^3\, r_{41}\, E_z$$

The phase change of the X and Y components of the optical field produced by a crystal of length L are given by

$$\frac{2\pi}{\lambda} L \Delta\eta = \frac{\pi L}{2\lambda} \eta_0^3 r_{41} E_z$$

If the modulating field, Ez is of the form $Ez = E_{z0} \sin \omega_M^t$ the X and Y components of the incident optical field are phase modulated and the resultant optical field components are given by

$$E_{opt} = E_{L0} \sin\left(\omega_{opt} t + \frac{\pi L}{2\lambda} \eta_0^3 r_{41} E_{z0} \sin \omega_M t\right)$$

E_{L0} is the maximum aplitude of the optical field electric vector after passing through the crystal of length L. The ratio of the power in the first side band of the optical field to the power in the optical carrier is given by

$$\left[2 J_1\left(\frac{\pi L \eta_0^3 r_{41} E_{20}}{2\lambda}\right) \Big/ J_0\left(\frac{\pi L \eta_0^3 r_{41} E_{z0}}{2\lambda}\right)\right]^2$$

λ is the wavelength of the incident optical field, and $\eta_0^3 r_{41} = 10^{-10}$ meters/volt for CdTe.

The apparatus used to modulate a CO_2 laser with the CdTe crystals is shown in Figure 1. The laser used was a frequency stabilized Honeywell flowing gas system. The CdTe crystal was placed inside a r-f cavity, resonant at 3.77 GHz with a loaded Q of approximately 2000. The modulating electric field was applied through the use of a stable r-f oscillator and traveling wave tube amplifier capable of supplying 10 watts to the resonant cavity. The frequency components of the modulated laser beam were determined with the use of a scanning Fabry-Perot interferometer and gold doped germanium photo conductive detector operated at 77°K.

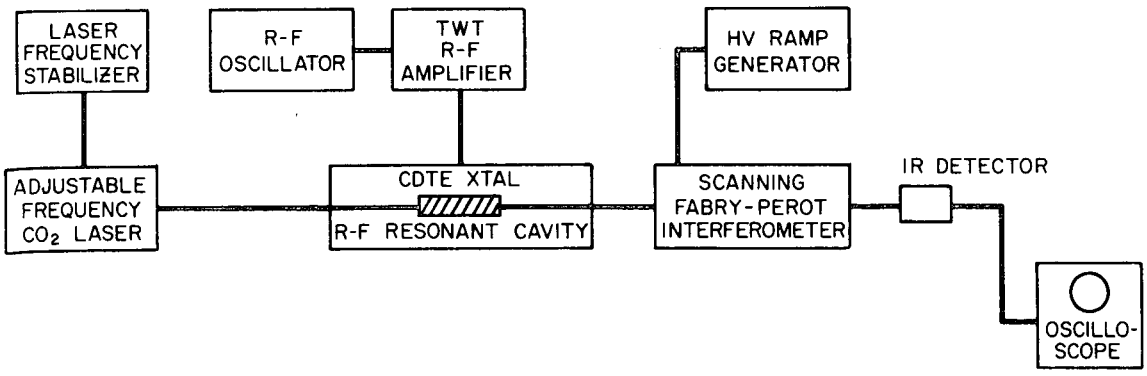

Figure 1. Apparatus used to phase modulate a CW CO_2 laser beam using CdTe electrooptic modulator.

The electric field, E_{zo}, that could be applied to the CdTe crystal is given by

$$E_{z0} = \left[\frac{4\,Q\,(1 - P_r)\,P_{iN}}{\pi\, f_0\, \epsilon_0\, V} \right]^{1/2}$$

where

P_{in} = power incident on the r-f resonant cavity

P_r = power reflection coefficient

Q = Cavity quality factor

$\epsilon_0 = 8.85 \times 10^{-12}$ farads/meter

f0 = cavity resonant frequency

V = cavity volume

The power reflection coefficient and cavity Q were determined with the tuning curve shown in Figure 2, and a spectrum analyzer. These measurements yielded a value of E_{zo} given by $E_{z0} = 360 \times P_{in}$ volts/cm where P_{in} is the r-f power in watts incident on the resonant cavity. The maximum expected value of the ratio of the power in the first sideband to power in the carrier obtainable with the experimental apparatus is given by

$$[2\,J_1\,(0.016)\,/J_0\,(0.016)]^2 \simeq 2.6 \times 10^{-4}$$

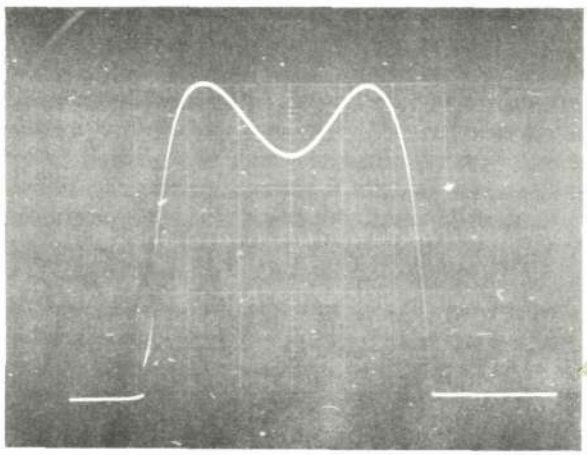

Figure 2. RF resonant cavity tuning curve. The cavity contained a CdTe crystal that had not been damaged by high RF power levels. Horizontal scale is approximately 1.5 MHz per centimeter.

As r-f power was applied to the crystal of CdTe, both crystals were observed to become more lossy after the absorbed r-f power levels exceeded 1 watt. The loaded cavity Q was observed to change slightly (by less than 10%), but more importantly, the power reflection coefficient increased from 0.1 to 0.8, as shown by the tuning curve in Figure 3. This substantially reduced the maximum value of E_{z_0} that could be applied to the crystal.

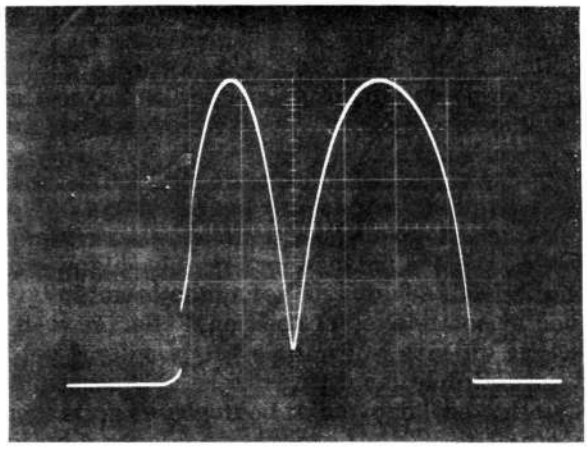

Figure 3. RF resonant cavity tuning curve after the CdTe crystal dielectric properties had been altered by RF power levels in excess of 1 watt. Horizontal scale is approximately 1.5 MHz per centimeter.

The crystals were also observed to absorb heat more rapidly after the applied r-f power levels had exceeded one watt. The crystal ends were parallel, polished surfaces, and hence the crystal acted as an etalon. The thermal expansion of the crystal caused the transmitted optical field to undergo variations in intensity that were easily observable. The rate at which these variations occurred increased by more than a factor of 10 after the change of cavity Q and power reflection coefficient had been observed. The change in the crystals' dielectric properties was irreversible.

Figure 4 indicates the output form the scanning Fabry-Perot interferometer. The peak corresponds to the laser carrier. Sidebands, if present, would be indicated by small peaks somewhere on the trace. The translateable mirror in the interferometer was attached to a piezoelectric cylinder whose maximum extension with applied voltage was only 1 micrometer. The entire translateable mirror assembly could be moved with a differential screw, allowing the interferometer to be manually scanned through one complete free spectral range (5.3 microns, or 600 MHz). No evidence of sidebands was ever seen. This was due to the extremely low values of the ratio of power in the sidebands to power in the carrier and the inability of the CdTe crystals to withstand applied electric field strengths of sufficient magnitude to produce sufficient, phase modulation in order to create detectable power in the sidebands.

The optical insertion loss was measured for both crystals, and found to be approximately 30%. This insertion loss was unchanged after the crystals were subjected to r-f power levels in excess of one watt. The high optical insertion loss precluded the possibility of modulation with the CdTe crystal inside the laser resonant cavity.

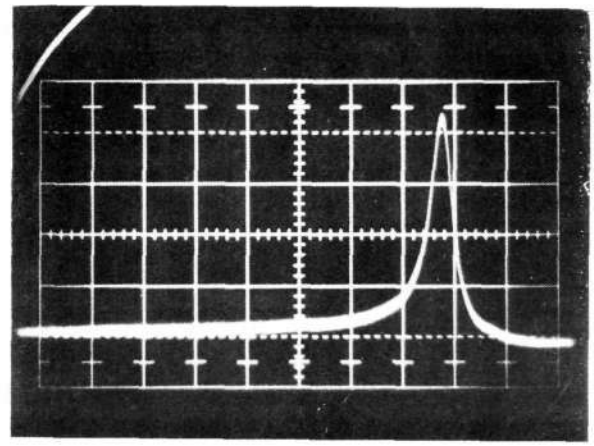

Figure 4. Output of scanning Fabry Perot interferometer. The large peak corresponds to the laser carrier frequency. Vertical scale is 1 mv per centimeter. Horizontal scale is approximately 12 MHz per centimeter.

III. GAS CELL MODULATORS

Modulation of CW CO_2 lasers oscillating at wavelengths of 9.6 and 10.6 micrometers at megacycle modulation frequencies has been observed with the use of low pressure gas cells[6]. Modulation is achieved by variations in time of the absorption coefficient of the gas caused by an applied, time varying electric field[7,8]. If the gas modulator is not located inside an optical resonant cavity and the laser beam simply passes through it, the ratio of the power in the first sideband to the power in the fundamental is given by[6]

$$[2\ J_1(\omega'/\nu)\,\tau\,\bar{\omega}/J_0(\omega'/\nu)]^2.$$

where

ω' = maximum Stark Effect energy level splitting

ν = modulation frequency

τ = mean collision time of gas molecules

$\bar{\omega}$ = frequency difference between optical radiation frequency and dc Stark Effect absorption frequency.

The Stark Effect energy level splitting is given by $\mu EM/\eta J(J+1)$ where μ is the dipole moment of the gas molecule for a particular electric dipole transition, E the applied electric field, h is Planck's Constant, J the total angular momentum of the gas molecule and M the Z component of J. In the event that $\bar{\omega} = 0$, no odd harmonic sidebands appear. The ratio of the power in the first even harmonic sideband (at frequency 2ν) to the power in the fundamental is given by

$$[2\ J_2(\omega'/\nu)/J_0(\omega'/\nu)]^2.$$

If the gas modulator is located inside an optical resonant cavity, the ratio of power in the sidebands to power in the carrier may be enhanced by a factor

$$\frac{1}{4} Q_{SB}^2 \left(\frac{t_{SB}}{t_L}\right)^2$$

(see the section of this report dealing with internal modulation of single mode lasers). Q_{SB} is the Q of the optical resonator at the sideband frequency and t_{SB}, t_L the transmissivity of the resonator mirrors at the sideband and laser fundamental wavelengths, respectively.

The gas cell used in the experiments consisted of a RF cavity resonant at approximately 3.8 GHz that had two salt windows set at the Brewster angle for 10.6 micrometer radiation attached to it. The cavity could be evacuated and filled with an absorbing gas at low pressure. The gas cell was of sufficient dimensions that it could be fitted inside a laser resonant cavity.

The apparatus used to modulate a CO_2 laser with the gas cell inside the laser optical resonant cavity is shown in Figure 5. The laser oscillation frequency could be adjusted through the use of a mirror attached to a piezoelectric cylinder (PZT). Total available mirror motion was 12 micrometers. Spectral analysis of the optical field with a scanning Fabry-Perot interferometer was again used to detect the presence of modulation of the laser beam. The gas used to modulate the laser was 1,1, difluorethane, $C_2H_4F_2$, which has two very strong absorption lines in the 10.6, micrometer CO_2 laser transition band, one at 944 cm^{-1} (P(20)) and one at 939 cm^{-1} (P(26)).

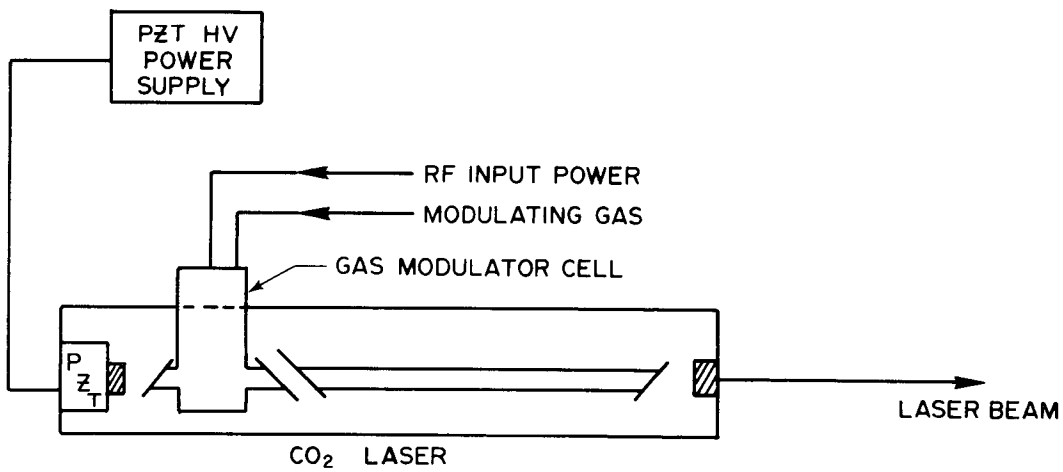

Figure 5. Apparatus used to modulate CO_2 laser with a gas modulator cell located inside the laser optical resonator.

An investigation was carried out to determine the effects on the CO_2 laser signature caused by the presence of the gas cell inside the laser resonator. Figure 6 gives the laser output power as a function of the position of the moveable mirror with no $C_2H_4F_2$ in the gas cell. The portion of the signature contained in the fifth box from the left and at the extreme right of the trace corresponds to the P(20) laser transition.

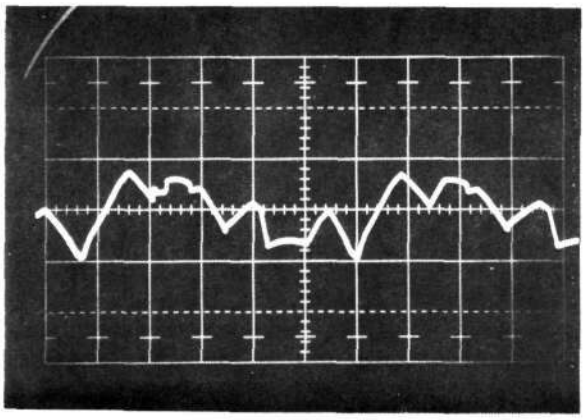

Figure 6. Laser signature for the case of an evacuated gas modulator cell.

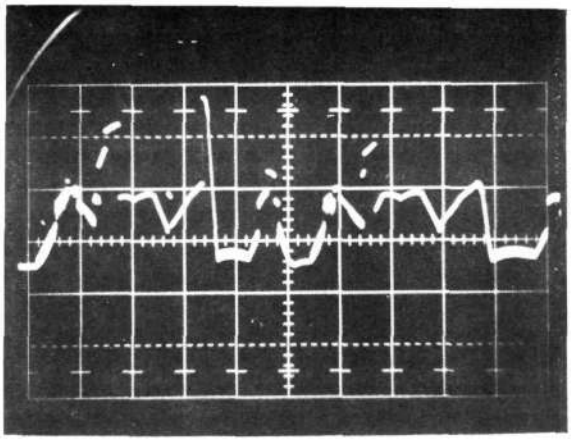

Figure 7. Laser signature when the gas modulator cell contains $C_2H_4F_2$ at a pressure of 0.2 mm Hg.

Figure 7 shows the effect on the laser signature of the presence of $C_2H_4F_2$ at a pressure of 0.2 mm Hg in the gas absorption cell. The presence of the gas causes the laser to oscillate on frequencies that are not absorbed by the gas, or to oscillate on a frequency that is absorbed by the gas but with a reduced amplitude of oscillation. The laser will, of course, oscillate at the frequency that has the highest gain in the laser resonant cavity. This is determined by the exact length of the cavity, the doppler profiles of the laser transitions, and the absorption losses of the gas modulator cell. The P(20) laser transition corresponds to the portion of the signature contained in the fourth, fifth and tenth boxes from the left. As the $C_2H_4F_2$ gas pressure in the modulator cell was increased, the laser output power at the P(20) oscillation frequency was reduced, as shown in Figures 8 and 9 ($C_2H_4F_2$ pressures of 0.3 mm Hg and 0.7 mm Hg respectively). A $C_2H_4F_2$ pressure of 1.2 mm Hg was sufficient to cause the laser to stop oscillating on the P(20) transition altogether, as indicated by the laser signature shown in Figure 10.

The laser output at frequencies absorbed by the $C_2H_4F_2$ was observed to be amplitude modulated at a low rate (10 - 100 KHz) as indicated by the signature shown in Figure 11. No externally applied electric field was applied to the gas in the modulator cell to cause this amplitude modulation. The pertinent features of this effect are summarized below.

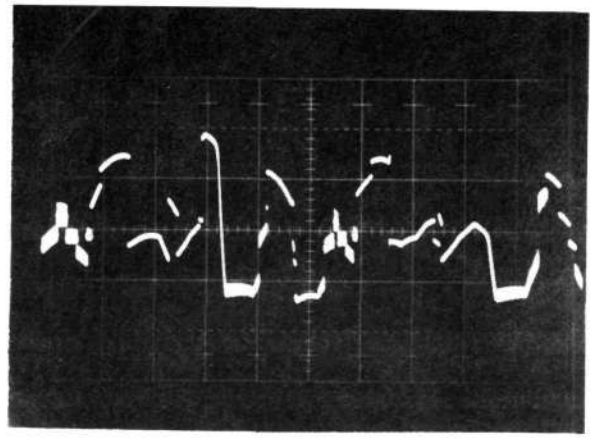

Figure 8. Laser signature when the gas modulator cell contains $C_2H_4F_2$ at a pressure of 0.4 mm Hg.

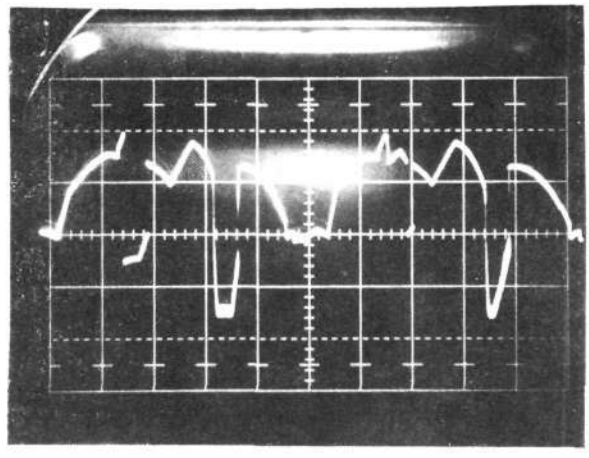

Figure 9. Laser signature when the gas modulator cell contains $C_2H_4F_2$ at a pressure of 0.7 mm Hg.

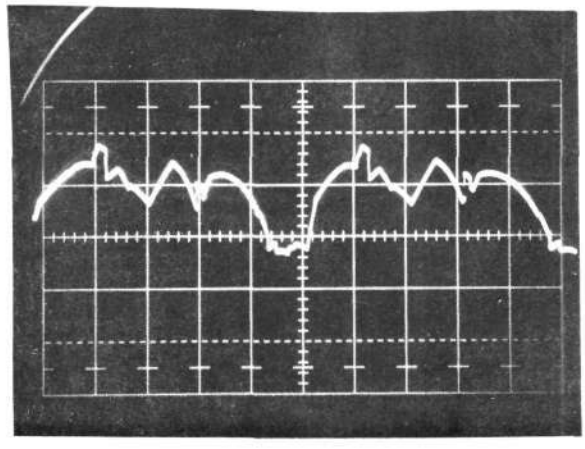

Figure 10. Laser signature when the gas modulator cell contains $C_2H_4F_2$ at a pressure of 1.2 mm Hg.

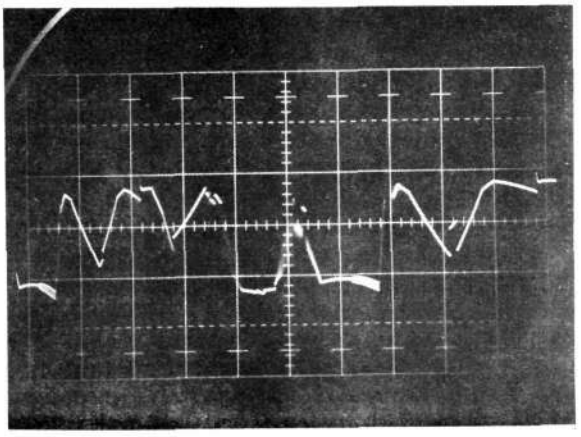

Figure 11. Laser signature showing kilocycle amplitude modulation of laser output frequencies that are absorbed by the gas in the modulator cell. The cell contained $C_2H_4F_2$ at a pressure of 0.2 mm Hg.

1. The amplitude modulation occurs only at frequencies absorbed by the gas in the modulator cell.

2. The frequency and wave shape of the amplitude modulation were extremely sensitive to the exact length of the laser resonant cavity. A change of a approximately 0.1 micrometers in the length of the laser resonant cavity caused the modulation frequency to change by a factor of 10, and the modulation wave shape to go from triangular to sinusoidal.

3. The modulation depends on the absorption line width of the gas. If the absorption lines are pressure broadened by mixing the gas with air, the amplitude modulation does not occur. Figure 12 gives the laser signature with the modulator cell containing $C_2H_4F_2$ at a partial pressure of 0.1 mm Hg and air at a partial pressure of 10 mm Hg. The signature is nearly identical to the signature shown in Figure 8, and differs only in the lack of kilohertz amplitude modulation of the laser oscillation frequencies absorbed by the $C_2H_4F_2$.

No satisfactory explanation for this low frequency amplitude modulation was found. It is not likely that it is due to the laser switching between different oscillation frequencies, since once it switched to an oscillation frequency for which the cavity gain was increased, it would remain oscillating at that frequency. The modulation is not due to a laser oscillation line shape containing two dominant frequency components separated by less than the laser cavity linewidth. Such an output line shape would require that the absorbing gas have an absorption line width of the same order of magnitude as the observed amplitude modulation frequency. The doppler broadened 944 cm^{-1} absorption line linewidth of $C_2H_4F_2$ at 300°K is 15 MHz.

Attempts were made to amplitude modulate the laser oscillating at the P(20) oscillation frequency with the gas cell inside the laser resonant cavity. The cell contained air at a partial pressure of 15 mm Hg and $C_2H_4F_2$ at a partial pressure of 0.2 mm Hg. This mixture could withstand an incident r-f power level of about one watt before the gas molecules became ionized. This corresponded to an applied electric field strength of about 300 volts/centimeter. The resultant Stark energy level splitting, ω' was of the order 10^7 Hz. The modulation frequency, ν, was 3.8×10^9 Hz. The expected ratio of

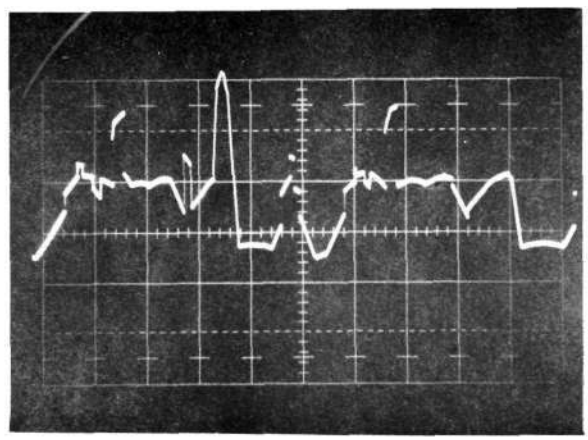

Figure 12. Laser signature when gas modulator cell contained $C_2H_4F_2$ at a partial pressure of 0.1 mm Hg and air at a partial pressure of 10 mm Hg.

power in the first sideband to power in the fundamental was of the order $Q_{SB}^2 \bar{\omega}\tau \times 10^{-6}$. Even though no dc electric field could be applied $\bar{\omega}$ could be varied over several megahertz by tuning the CO_2 laser over the doppler broadened P(20) laser transition. The transmissivity of the resonator mirrors was the same for both the sideband and laser fundamental frequencies. The optical resonator Q for the sideband, Q_{SB}, may have been low since the sideband frequency may not have been close to multiple of the axial mode spacing of the laser resonator.

The scanning Fabry Perot interferometer was used for spectral analysis of the modulated laser beam. No evidence of modulation was ever seen. This was probably due to the condition $\bar{\omega}\tau\, Q_{SB}^2 << 10^6$. This factor could not be increased since neither the modulating frequency ν nor the length of the laser resonator cavity could be varied so that the sideband frequencies coincided with the multiples of the laser resonator axial mode spacing. If the sideband frequencies did coincide with a resonant frequency of the optical cavity, Q_{SB}^2 could easily be of the order 10^{10} to 10^{12}.

IV. CONCLUSIONS

Although neither attempt at modulation of a CO_2 laser at gigahertz modulation frequencies proved successful, both methods could be made to work. In the case of modulation with CdTe crystals, more work is needed to determine techniques for producing CdTe crystals that can withstand high r-f power levels.

Gas cell modulators have been demonstrated to effectively modulate CO_2 lasers at frequencies for which $\omega'/\nu \simeq 1$. Modulation at frequencies for which $\omega'/\nu << 1$ is impractical for modulator cells outside an optical resonant cavity due to the extremely low ratio of power in the sidebands to power in the laser carrier. Location of the gas modulator inside the laser resonant cavity drastically alters the laser signature and could prevent frequency stabilization of the laser with the use of the power profile feedback type stabilization schemes. However, a gas cell modulator located in a properly designed passive optical resonant cavity could prove to be an efficient method of modulation at multiples of the optical cavity axial model spacing.

REFERENCES

1. K. K. Chow, et. al., IEEE J. Quant. Elect. QE-5, 12. 618 (1969)

2. D. C. Auth. IEEE J. Quant. Elect. QE-5 12 622 (1969)

3. A. Yariv, et. al., IEEE J. Quant. Elect. QE-2, 243 (1966)

4. J. Keifer, IEEE J. Quant. Elect. QE-5 309 (1969)

5. A. Yariv, Quantum Electronics, John Wiley & Sons, N.Y., N.Y., p. 301.

6. Y. A. Pao, et al., "High Frequency Modulation of CO_2 Laser Using Stark Effect on Molecular Cases," Case Western Reserve Univ. preprint.

7. R. Karplus, J. Schwinger, Phys. Rev. 73 1020 (1948)

8. R. Karplus, Phys. Rev. 73 1027 (1948).

SCATTERING AND PROPAGATION

Garabet J. Gabriel
Electrical Engineering Department
University of Notre Dame
Notre Dame, Indiana

1. RESEARCH

The research effort was addressed to the problem of scattering of electromagnetic waves from earth and its effects in multipath communication between two satellites such as in the proposed Data Relay Satellite System and Navigational Satellite. To date no rigorous or semirigorous analyses of the problem, appropriate to conditions of DRS system, exist in the literature. The need for a fresh approach became apparent. Principal conclusions of this attempt are summarized next; details will appear in a GSFC document:

(a) The method of current distribution, heretofore considered an approximation which is strictly valid only on infinite flat surface illuminated by a plane wave, is proved to be one of the weakest foundations of treatments of scattering from the real earth.

(b) When a large, conducting, irregular object is illuminated with a plane wave, only the point on the surface which is directly below the receiver contributes significantly to the scattered field at the receiver. The asymptotic method used here is not conclusive at this stage when the illumination is from a finite source.

2. GSFC COMPUTER APPROACH

An existing program at GSFC was being adapted for numerical integration of the rigorous integrals for it was found, the field oscillates erratically as the integration area is increased, no criteria for truncation could be determined. Requested to resolve this difficulty, I demonstrated analytically that the scattered field should oscillate with increasing area, and that integration must extend over entire illuminated region. Accordingly, it was concluded that it would be impractical and uneconomical from the standpoint of time and cost to integrate numerically over the entire illuminated region.

3. CONSULTATION

I was invited as consultant-observer to a conference with representatives of GSFC, TSC, and FAA to resolve differences in treatments of data on polar cap absorption, scintillation absorption, and multipath effects as pertinent to the proposed Aircraft Navigational Satellite. Of principal concern was the relative merits and demerits of L-band vs. VHF frequency. Assistance was also given in explaining differences in statistical processing of scintillation data by AFCRL and COMSAT.

In summary, the Fellowship Program afforded a valuable opportunity for research and exchange of ideas and viewpoints.

ELECTRON IMPACT IONIZATION OF HYDROGEN NEAR THRESHOLD

Yukap Hahn
Department of Physics
University of Connecticut
Storrs, Connecticut

The study reported here has been carried out in collaboration with Dr. A. Temkin and Dr. A. Bhatia of the Lab. for Space Studies, NASA.

When electrons of about 1 Ryd. energy collide with a hydrogen target, there are an infinite number of channels opening up, and reactions of the following forms are possible:

$$e_1^- + (e_2^- + p^+) \rightarrow e_i^- + (e_j^- + p^+)_0 \quad \text{elastic}$$

$$\rightarrow e_i^- + (e_j^- + p^+)_n \quad \text{inelastic}$$

$$\rightarrow e_i^- + e_2^- + p^+ \quad \text{ionization}$$

Theoretical analysis of this multichannel problem is complicated further by the long-range character of the interactions involved and also by the presence of three-particle (ionization) channels.

The ionization problem near the threshold has been discussed by many people in the past, and these studies indicate the correct threshold behavior of the ionization cross section depends critically on the dynamical screening of the proton charge by one of the electrons as they come away from the proton. The first ingenious classical argument of Wannier[1] gave the yield Y to depend on E as $E^{1.127}$, while the assumption of complete screening[2] gives the behavior $Y(E) \sim E^{1.5}$ as $E \rightarrow 0$ and the case of no screening[3] $Y(E) \sim E^{1.0}$. More recent investigations[4,5] of the problem using the WKB-type wave functions seem to reproduce the Wannier result. In all cases, however, the most probable configuration of the two electrons as they move away from the proton is given by $\theta_{12} = \Pi$, i.e., the electrons are coming out in the opposite directions.

In an attempt to treat the problem completely quantum mechanically, we have introduced a model in which the interelectron potential e^2/r_{12} is replaced by $e^2/(r_1 + r_2)$, which is in fact exactly the same as the original potential for $\theta_{12} = \Pi$. This new potential simplifies the analysis a great deal since, e.g., for the zero total partial wave L = 0, each $\ell_1 = \ell_2$ component uncouples. And yet, the all-important dipole terms are still present, as $- r_1^{-1} + (r_1 + r_2)^{-1} \simeq - r_2/r_1^2$ for $r_1 >> r_2$.

The general formalism adapted for this problem is the projection method of Feshbach[6] for the low energy problem at $E = -n^{-2}$ (Ryd.), where n is the principal quantum number and large. One of the motivating reasons for this approach is the earlier calculation by Temkin, Bhatia and Sullivan[2] in which they showed that the resonance states arising from the degeneracy of levels for each n and different $\ell \leq n$ are the dominant components of the optical potential and can be represented by unscreened Coulomb wave functions. This in principle allows one then to construct a reliable potential.

We have analytically solved the problem in the one-level approximation, and found that $Y(E) \sim E$ for this case, with or without the one-term optical potential. However, there are of course an infinite number of levels contributing to the potential, and thus the result has to be generalized to include all the levels. Their inclusion requires a detailed examination of the dependence on n of the widths and shifts of these levels. Preliminary indications are that their total contribution may not change much the one-level result insofar as the threshold behavior is concerned, but it is not yet clear what the precise magnitude of the change would be. We have not completed the study of this model, but we feel that many of the conceptual difficulties in the formulation of the theory have been cleared up by the present study. We hope to continue the work on the model and also to be able to apply the approach to the real physical case.

REFERENCES

1. G. H. Wannier, Phys. Rev. 90, 817 (1953)

2. A. Temkin, A. K. Bhatia, and E. Sullivan, Phys. Rev. 176, 80 (1968); A Temkin, Phys. Rev. Letters, 16, 835 (1966).

3. M. Rudge and M. J. Seaton, Proc. Roy. Soc. (London) A283, 262 (1965).

4. Liepinsh and Peterkop, unpublished, 1968.

5. A. R. P. Rau (unpublished).

6. H. Feshbach, Ann. Phys. (N.Y.) 19, 287 (1962).

ANALYSIS OF DATA FROM THE FILTER WEDGE SPECTROMETER (FWS) ON NUMBUS D

Edward A. Harms
Department of Physics
Fairfield University
Fairfield, Connecticut

The summer was spent investigating data received from the Filter Wedge Spectrometer (FWS) on Nimbus D. The spectrometer scans the wavelength interval from 1.26 to 2.45 microns. The general idea was to determine how much useful information (from a remote sensing point of view) is contained in this interval.

Two subprograms were investigated. The first was the determination of ground truth data available. The second was to determine the information content in this interval. The quality of the ground truth data determines to a great intent the possibilities for success in the second problem.

Various methods were developed to aid in the interpretation of the data. As a result the general qualitative nature of the spectra are felt to be fairly well understood. Some preliminary results were also obtained from a statistical analysis of the spectra. Results were encouraging although inconclusive due mainly to the lack of sufficiently detailed ground truth data.

PRECEDING PAGE BLANK NOT FILMED

X-RAY STUDY ON MATERIALS

Ernest H. Henninger
Department of Physics
DePauw University
Greencastle, Indiana

Some techniques and theories related to X-Ray studies of materials were studied. The work fell in four categories: (1) Preparing and examining powder samples from a nickel-titanium alloy; (2) Learning the principles and operating techniques of a Buerger precession camera; (3) Studying the techniques of X-Ray stress topography; (4) Studying the Kinematical and Dynamical Theories of X-Ray diffraction.

(1) Powder samples from the bulk ingot were readily identified as being a Nizti alloy by indexing the forword reflection Debyescherrer-lines. Of more interest was the composition and structure of small fibers which formed on the surface. Attempts to remove individual fibers by etching and cutting failed, but filings from the surface were examined. Also back reflection lines from the fibrous surface were recorded. All patterns showed the Ni_3Ti series of lines[1] with no evidence of the pure Ni or NiTi phases. Only one observed line was unaccounted for. The only metal which could fit both that line and a companion group consistent with the other experimental lines is Josephenite, a nickel-iron alloy. The sample alloy is Ni_3Ti with some possible iron contamination.

(2) The direct goal was to learn how to take and index precession photographs. These are direct magnifications of reciprocal lattice planes.[2] Confusing photographs early on led to closer examination of the physics of the effects. It was found that usable cone-axis and upper level precession photographs could not be obtained using copper radiation unless the associated crystal axis has a parameter greater than 10 A°. Molybdenum radiation was not available. Hence the early samples were replaced with a $CaWO_4$ crystal with large lattice constant, c = 11.4 A°. Although a very thin slice was cut the absorption was too high to give good pictures. Nevertheless the symmetry of the crystal and the lattice parameters were confirmed. The study did teach the method and emphasized the requirements of proper wavelength, crystal size and absorption, camera settings, film type and exposure, and crystal alignment.

(3) X-Ray Stress topography covers a number of techniques[3] for detecting individual dislocations in perfect or slightly strained crystals. Such stdies have become valuable with the availability of perfect crystals for semiconductor devices technology. Defects introduced during processing are known to degrade the performance of such devices[4].

Defects are made visible either by the direct image contrast due to kinematical scattering from disturbed lattice planes in the vicinity of a defect, or by dynamical effects, including the disruption by a defect of anomoulous scattered inten sity[5]. The author hopes to initiate work in this area in connection with his colleague.

(4) The X-Ray diffraction theories[6] were studied in order to better understand the precession method and the stress topography. The more familiar kinematical theory is known to be fundamentally incorrect, but it is useful nonetheless for structure determinations, since most crystals have a mosaic structure. Scattering from imperfect crystals, is best understood in terms of the Ewald construction. In a perfect crystal multiple scattering must be taken into account, and the resultant energy transfer pattern through the crystal is determined by the complex electromagnetic wave field which can exist, subject to Maxwell's equations and the electron distribution. The possible waves

are still related to those reciprocal lattice points very near the Ewald sphere, but the single Laue point is replaced by a set of points located on sheets of a dispersion surface.

REFERENCES

1. ASTM Powder Diffraction File.

2. M. J. Buerger; The Precession Method, Wiley, 1964.

3. Bouse, Hart and Newkirk; Encyclopedia Dictionary of Physics, Supplement 1, 1966, p. 391-9.

4. G. H. Schwattke; IBM Research Report, AFCRL-67-0564 (1967)

5. E. S. Meieran; Siemens Review, Vol. 37 (1970).

6. R. W. James; Solid State Physics, Vol. 15, Academic Press, 1963.

A QUASI-OPTIMAL CONTROL SYSTEM FOR STEERABLE STRUCTURES

Eugene W. Henry
Department of Electrical Engineering
University of Notre Dame
Notre Dame, Indiana

1. ACKNOWLEDGMENT

This research was performed at the NASA Goddard Space Flight Center (GSFC) in the Control Section of the Antenna Systems Branch of the Advanced Development Division, under the supervision of NASA Colleague George C. Winston, with the encouragement and assistance of Don Griffin, Nick Raumann, Jim Lombardo, Arnold Abbott, and Jim Vinson. Experimental work was accomplished at the Goddard Network Test and Training Facility (NTTF), and at the Goddard Optical Research Facility (GORF).

2. INTRODUCTION

The precise and reliable control of mechanically steerable antennas and telescopes under a variety of environmental conditions is essential for the successful operation of the NASA Satellite Tracking and Data Acquisition Network (STADAN) and the Manned Space Flight Network (MSFN). STADAN has 73 steerable antennas in 16 locations throughout the world and MSFN has 47 steerable antennas at 21 sites [1].

GSFC directs continuing in-house and contracted research on control systems for antennas and telescopes. Recent supported research includes the application of on-line optimal digital control[3], and model-reference adaptive control[4] to the antenna control problem. A significant in-house development was a precise digital-analog control system for an optical mount[2]. This mount, consisting of a two-axis drive for a 24-inch diameter telescope 10 feet long, was available for experimentation with the quasi-optimal control system as described in this report.

This work consisted of three concurrent interrelated efforts: development of a model of the plant (system to be controlled) from theory and from experimental data; simulation of the model and the quasi-optimal control on an analog computer at NTTF; and implementation of the control system on the optical mount at GORF.

3. STATEMENT OF THE PROBLEM

The problem is stated in terms of controlling one axis of the 24-inch telescope at GORF, but similar specifications obtain for steerable structures in general. The slew mode is used for acquisition of a target, after which the track mode is employed for precise following. The controlled system must meet the following specifications:

Maximum acceleration:	2 deg/sec^2 slew, 0.2 deg/sec^2 track
Velocity range:	5 deg/sec maximum slew, .0005 to 5 deg/sec track
Tracking accuracy:	±1 arc second

These requirements are to be maintained with noise of specified properties on the tachometer and error signals, and with variations of X-axis inertia between 1900 and 4600 lb-ft-sec^2 caused by motion of the Y-axis.

4. THE QUASI-OPTIMAL CONTROL

In the slew mode, it is desired to acquire the target in minimum time, subject to the constraints on maximum acceleration and velocity. It is well known that the time optimal control of a double-integral plant is accomplished by means of a relay servo with a quadratic switching curve. Time optimal control of higher order plants, although theoretically possible, require extensive on-line computation.

The quasi-optimal control method employs appropriate compensation networks between the tachometer and the servo amplifier so that the resulting minor loop has a transfer function approximating a double integration. The outer loop contains a relay controller with the quadratic switching criterion. Velocity limiting is provided by a dead-zone feedback circuit from the tachometer in the minor loop.

In response to a step input in the slew mode, this sytem will cause the mount to accelerate at 2 deg/sec^2 until the velocity reaches 5 deg/sec, and maintain that velocity until the controller commands an acceleration of -2 deg/sec^2 to bring the mount to the commanded position in minimum time without overshoot.

In the track mode three gains are changed simultaneously in the controller to reduce the maximum commanded acceleration to 0.2 deg/sec^2 and to change the dynamic operating region of the quadratic switching curve circuit.

Advantages of this quasi-optimal controller are.

a. It is relatively simple to implement with either analog or digital devices.

b. It essentially provides time-optimal control for step inputs in the slew mode.

c. The system will reject torque disturbances within the capacity of the motor.

d. It has low sensitivity to changes in load inertia.

e. No transient disturbance is caused by switching between track and slew modes.

5. DEVELOPMENT OF THE MODEL

The model was developed from theory and experimental data as a fifth order plant to include an oscillatory structural mode as well as the electrical and mechanical aperiodic modes. Static friction, coulomb friction, and power amplifier saturation were also included in the model. Methods were developed to readily determine the values of friction, inertia, and other plant parameters from simple experiments on the mount.

6. SIMULATION AT NTTF

The model of the plant and the quasi-optimal controller were simulated on an Electronics Associates, Inc. TR-48 Analog Computer at NTTF. The simulation included provision for studying the effects of random disturbances on the tachometer signal, the error signal and the output (torque disturbance). This simulation was used to determine optimal settings of controller parameters and to investigate the behavior of the system in both track and slew modes with various disturbances and reference inputs.

7. IMPLEMENTATION AT GORF

The controller circuitry was implemented on another EAI TR-48 Analog Computer at GORF. The tachometer and position-potentiometer signals from the telescope were connected to the computer, and the computer provided the driving signal to the servo amplifier.

8. RESULTS

The results of the computer simulation indicate that the quasi-optimal control is feasible and can meet the specifications while providing the advantages listed in Paragraph 4. Limited experiments at GORF verified the desired system behavior in the slew mode and the absence of transients in switching between track and slew modes. Performance of the telescope in the track mode was not satisfactory due to excessive noise.

9. SUGGESTIONS FOR FURTHER RESEARCH

a. The sources of noise in the physical system should be isolated and analyzed so that appropriate filters can be incorporated.

b. Implementation of quasi-optimal control by digital rather than analog techniques should be investigated as a means for providing precise control while eliminating much of the drift and noise which plagues the analog controller.

c. Alternative approaches to the design of compensation for the inner loop and the possible inclusion of another minor loop enclosing the relay element to provide a system which is stable for all values of gain[5] should be investigated.

A FEEDBACK COMMUNICATION SYSTEM USING CONVOLUTIONAL CODES

Joseph L. Katz
Department of Electrical Engineering
Purdue University
Lafayette, Indiana

In recent years the application of feedback to communication systems has received a generous amount of attention in the literature and certain theoretical aspects of feedback systems has been studied in detail. Two-way communication systems have the capability of transmitting information about the current state of a message being decoded at the receiver back to the transmitting point. The returned information can be used to simplify the coding and decoding operations in the forward channel and to provide a lower probability of error for a given coding delay than could be achieved without feedback. A potentially useful application of feedback communication systems is in the design of efficient data retrieval systems for space vehicles, where the transmitter power of the spacecraft is restricted to be several orders of magnitude less than the transmitting power of the based equipment.

In general communication feedback systems can be classified according to the type of information carried by the feedback channel. The term "decision feedback" is used when the feedback channel is used only to report the decision of the receiver as to the acceptability of each received message unit, and "information feedback" when the feedback channel is employed to report information about each received message unit to the transmitter, the decision to accept, or reject and correct, subsequently being made at the transmitter.

In either type of system once a decision is made that the message cannot be interpreted, the transmitter may repeat, in whole or in part, the ambiguous message unit either using the same code and transmitter power or by agreement, shifting to a higher redundancy code and transmitter power or any combination of the two. The adaptive nature of feedback systems permit the efficient matching of the signals to variations in the channel conditions. This in turn permits the setting of an upper limit on the probability of error, whereas for a unidirectional link the signals must be chosen such that the error probability will not be excessive at the poorest signal-to-noise ratio which is anticipated.

During the fellowship period a decision feedback communication system, using convolutional encoding in the forward channel, was studied. Results were obtained for the case of sequential decoding and partial results for maximum likelihood decoding of a 1/2 rate systematic convolutional code.

The feedback system incorporating convolutional encoding-sequential decoding used a simple request repeat strategy in which repeats are requested for frames in which a computation overflow occurred. The repeated frames are retransmitted using a 1/2 rate non-systematic code and a 1/4 rate code is formed from the first and retransmitted information. Decoding is attempted a second time using the resulting 1/4 rate code. It an overflow occurs the second time a detected error is declared. A full scale computer simulation of this sytem revealed substantial improvement in the computational overflow rate over the unidirectional system for $E_b/No < 2.0$ db.

The problem of computational overflow does not exist for maximum likelihood decoders but decoders of this type can only be built for short-constraint length convolutional codes. This limits the amount of improvement in bit error over no coding which can be achieved. A feedback system similar to the one described earlier was implemented using a maximum likelihood decoder. Repeats are requested for frames in which the metric falls below a given threshold. Indications are that this system will improve the bit error rate of the short constraint length code; however, results are sketchy at this time. Work on this topic will continue under a NASA grant.

INVESTIGATION OF WALSH FUNCTIONS FOR SIGNAL PARAMETER EXTRACTION

Thomas F. Krile
Department of Electrical Engineering
Rose Polytechnic Institute
Terre Haute, Indiana

I. INTRODUCTION

As signal processing systems consume ever increasing amounts of data, much of it having low information content, the problems of bandwidth reduction and signal parameter extraction become more important. Spacecraft in particular are required to gather large amounts of data and transmit it to earth. Due to the inherent power restrictions aboard spacecraft, and the complex coding required to minimize errors, it becomes apparent that some signal processing should be done on board so that only the most significant signal parameters are transmitted.

Other signal processing systems, such as in ECM or surveillance, require essentially real time data processing. In such cases, it is useful to examine only a few specific signal parameters, and the problem is to determine which parameters are the most significant and most quickly and easily obtained.

One well-known way to analyze signal parameters is to use a given set of basis functions to transform the signal to another representation. Then the new signal space is examined to see if any important information is more apparent than it was in the original space. A typical example of this process is the Fourier transform analysis of signals. The resulting frequency spectrum has long been used in single-dimensional signal analysis, and more recently has shown itself to be a powerful tool for two-dimensional image processing[9] (i.e., parameter extraction for pattern recognition). The Fourier transform has also been proposed for bandwidth reduction schemes in which only a selected portion of the spectrum is transmitted and the signal is reconstructed for this truncated spectrum.[3]

Progress in integrated circuit technology has made the hitherto academic Walsh transform into a practical tool for digital signal processing.[5] With suitable definitions for the Dirac delta function and the convolution operation, one can show many properties of the Walsh transform which are analogous to those of the Fourier transform. Also, relationships analogous to Parseval's theorem and the Wiener-Khinchin theorem can be shown to hold. This means that one can perform data reduction and filtering in the Walsh domain.

The first part of this report presents definitions and properties of the one- and two-dimensional Walsh functions and Walsh transforms. The primary part of this paper is devoted to uses of the Walsh spectrum of two-dimensional images for parameter extraction. A set of "correlation masks" is shown which, when applied to the image, result in the individual elements of the Walsh transform. The same masks can be applied to the transform to recover the original image.

As in the Fourier transform case, the orientation and separation of line structure in an image can be determined from the Walsh transform. However, there is an angle ambiguity, since all the amplitude information in the Walsh plane is contained in one quadrant, whereas in the Fourier plane it is in two quadrants.

The most troublesome aspect of the Walsh transform is that it is not translation invariant, as the Fourier transform is. A form of power spectrum is developed which is translation invariant and which reduces the number of spectral data points from $(2^p)^2$ to $(p + 1)^2$ where 2^p is the order of the Walsh matrix. This power spectrum preserves the angle information contained in the original transform. Its other pattern recognition aspects have yet to be investigated.

II. DEFINITIONS

Walsh functions form a closed set of orthogonal functions, bounded in time (or space), which can be used as bases for signal representation.[6] In this report, the discrete version of the Walsh functions is used.

Each Walsh function can be viewed as a row vector Wal(i) of dimensionality $N = 2^p$ where p is an integer. Let Wal(i,m) refer to the m^{th} component of the i^{th} function, i = 0, N - 1 and m = 0, N - 1. The vector components consist of +1's and -1's, so the functions are binary in nature, and Wal(1), is (1,1,1, . . . , 1) by definition.

Walsh functions are ordered according to the number of zero crossings (transitions from ± 1 to ∓ 1) in the interval of definition. This gives rise to the generalized frequency concept of "sequency" where, if j > i, then Wal(j), will have a greater sequency (greater number of zero crossings per unit interval) than Wal(i). Using this ordering, the Walsh transform sequency plane will be roughly analogous to the Fourier transform frequency plane.

The functions themselves may be defined via several routes. They may be written as products of Rademacher functions taken in a certain order.[7] They may also be obtained as the solutions of a difference equation[4] (as the Fourier sine and cosine components arise from a differential equation). We consider here a function generating method proposed by Swick[11] which allows one to obtain individual functions independently by taking advantage of the sequency ordering and the symmetries inherent in the functions.

The first step in forming Wal(i) is to express the sequency number i in binary form as $b_0 b_1 \ldots b_{p-1}$ where the decimal value of i is given by

$$i = b_0\, 2^{p-1} + b_1\, 2^{p-2} + \ldots + b_{p-1}\, 2^0. \qquad (1)$$

We let Wal(i,0) be +1 for all i. Now if b_0 is 1, the m = 0 and m = 1 components of Wal(i) are skew symmetric, otherwise they are symmetric. If b_1 is 1, the (0,1) and (2,3) components of Wal(i) are skew symmetric, otherwise they are symmetric. If b_2 is 1, the (0, 1, 2, 3) and (4, 5, 6, 7) components of Wal(i) are skew symmetric, otherwise they are symmetric. In general, if b_k is 1, the $(0, 1, \ldots, 2^k - 1)$ and $(2^k, \ldots, 2^{k+1} - 1)$ components of Wal(i) are skew symmetric, otherwise they are symmetric. An APL function using this generating method is included in the Appendix.

As an example of this procedure, consider a system of order N = 8 (p = 3) and the function Wal (6). First we have $i = 6 = 110 = b_0 b_1 b_2$. Since $b_0 = 1$, we find 1 = Wal (6, 0) = - Wal (6, 1). Also, $b_1 = 1$, so Wal (6,0) = -Wal (6,3) = 1 and Wal (6,1) = -Wal (6,2) = -1. Finally, $b_2 = 0$, so Wal (6,0) = Wal (6,7) = 1, Wal (6,1) = Wal (6,6) = -1, Wal (6,2) = Wal (6,5) = 1, and Wal (6,3) = Wal (6,4 = - 1. Thus we have Wal (6,) - (1, -1, 1, -1, -1, 1, -1, 1).

An important property of the Walsh functions is that they are orthogonal, i.e.

$$\sum_{j=0}^{N-1} \mathrm{Wal}\,(i,\, j)\,\mathrm{Wal}\,(k,\, j) = \begin{cases} 0, & i \neq k \\ N, & i = 1. \end{cases} \tag{2}$$

In order to obtain the Walsh transform, a matrix is set up composed of rows which are the individual Walsh functions in ascending sequency. As an example, consider the case for $N = 2^3 = 8$. The Walsh matrix is:

$$\underset{\sim}{W} = \begin{bmatrix} 1 & 1 & 1 & 1 & 1 & 1 & 1 & 1 \\ 1 & 1 & 1 & 1 & -1 & -1 & -1 & -1 \\ 1 & 1 & -1 & -1 & -1 & -1 & 1 & 1 \\ 1 & 1 & -1 & -1 & 1 & 1 & -1 & -1 \\ 1 & -1 & -1 & 1 & 1 & -1 & -1 & 1 \\ 1 & -1 & -1 & 1 & -1 & 1 & 1 & -1 \\ 1 & -1 & 1 & -1 & -1 & 1 & -1 & 1 \\ 1 & -1 & 1 & -1 & 1 & -1 & 1 & 1 \end{bmatrix} \begin{matrix} \text{Sequency} \\ 0 \\ 1 \\ 2 \\ 3 \\ 4 \\ 5 \\ 6 \\ 7 \end{matrix} \tag{3}$$

Note that the matrix is symmetric, it is in fact a re-ordering of a symmetric Hadamard matrix (a related signal processing operator is the Hadamard transform[12]).

If the signal to be transformed is an N-dimensional column vector $\vec{X} = (x_1, x_2, \ldots, x_N)$, then the Walsh transform is defined as

$$\vec{T} = (1/N)\, \underset{\sim}{W}^t\, \vec{X} = (1/N)\, \underset{\sim}{W}\, \vec{X} \tag{4}$$

where t denotes the transpose. The inverse operation is given by

$$\vec{X} = \underset{\sim}{W}\, \vec{T}. \tag{5}$$

When the signal is an N^{th} order square matrix X, the transform is found from:

$$\underset{\sim}{T} = (1/N)\, \underset{\sim}{W}^t\, \underset{\sim}{X}\, \underset{\sim}{W} = (1/N)\, \underset{\sim}{W}\, \underset{\sim}{X}\, \underset{\sim}{W}. \tag{6}$$

The inverse is then

$$\underset{\sim}{X} = (1/N)\, \underset{\sim}{W}\, \underset{\sim}{T}\, \underset{\sim}{W}, \tag{7}$$

and we see that the two-dimensional Walsh transform is self-inverse.

III. PROPERTIES

By making suitable definitions, one can show several properties of the Walsh transform which are analogous to those of the Fourier transform.[8] These properties can give us a hint as to what features or parameters will be significant in the sequency plane.

The discussion to follow will consider one-dimensional signals and transforms; extension to two dimensions is straight-forward. Let a delta function be defined as a vector $\vec{\delta} = (1,0, \ldots, 0)$. Then the Walsh transform of $\vec{\delta}$ is the vector $\vec{T} = (1/N, 1/N, \ldots, 1/N)$, where N is the order of the system. Thus we see that a delta function in time (or space) transforms into a constant in the sequency domain, and vice versa. In general, a compression in the time domain results in expansion in the sequency domain. This same result occurs in the Fourier case. It should be pointed out, however, that the time-sequency bandwidth product is always finite for the Walsh system (because both the signal and basis functions must be finite), but the time-frequency bandwidth product is infinite for the Fourier transform.

Using a special relationship due to Gibbs[2], we can define "logical convolution" of two sequences (vectors) X and Y as

$$Z_L(s) = (1/N) \sum_{i=0}^{N-1} X(i)\, Y(s \oplus i);\ s = 0,\ N-1; \tag{8}$$

where $\oplus$ indicates addition modulo 2. We abbreviate this to $\vec{Z}_L = \vec{X} \oplus \vec{Y}$. Now letting the Walsh transforms of $\vec{X}$ and $\vec{Y}$ be $\vec{T}_x$ and $\vec{T}_y$, respectively, and using the addition formula for Walsh transforms (Wal(i,m) Wal(j,m) = Wal(i $\oplus$ j, m)), we have

$$Z_L(s) = \sum_{i=0}^{N-1} T_x(i)\, T_y(i)\, \mathrm{Wal}(i, s). \tag{9}$$

Thus we obtain the logical convolution of two functions, $\vec{X}$ and $\vec{Y}$, by taking the Walsh transform of the term-by-term (scalar) product of their transforms, $\vec{T}_x$ and $\vec{T}_y$. The same procedure is applied to find the normal convolution of two functions using Fourier transforms.

Using the definition of logical convolution, we can define the logical autocorrelation of a function X as

$$\vec{L}_x = \vec{X} \oplus \vec{X}. \tag{10}$$

Also, we can define a Walsh power spectrum $\vec{S}_x$ for $\vec{X}$ where

$$S_x(i) = [T_x(i)]^2,\ i = 0,\ N-1. \tag{11}$$

This is analogous to the Fourier power spectrum definition. Now using Eq. (10), we find that the logical autocorrection of $\vec{X}$ and the Walsh power spectrum of $\vec{X}$ are a Walsh transform pair. This statement is the analog of the Wiener-Khinchin theorem in the Fourier case.

The results given above can also be combined to show a Walsh analog to Parseval's theorem, i.e.

$$(1/N)\sum_{i=0}^{N-1}[X(i)]^2 = \sum_{j=0}^{N-1}[T_x(j)]^2. \tag{12}$$

These Walsh transform analogs of the familiar Fourier transform theorems justify the investigation of the Walsh spectrum for filtering, bandwidth reduction, and parameter extraction operations.

IV. PARAMETER EXTRACTION

A set of correlation mask operators has been found which is useful for determining parameter extraction properties in the Walsh sequency domain. Consider a matrix mask $\underset{\sim}{M}_{ij}$, consisting of +1's and -1's, which is of order N. The mask is obtained by modulating the column vector Wal (i) by the row vector Wal(j). An example of the masks $\underset{\sim}{M}_{00}$, $\underset{\sim}{M}_{01}, \ldots, \underset{\sim}{M}_{33}$ for a fourth order Walsh system is shown in Figure 1.

Let $\underset{\sim}{C} = \underset{\sim}{M} \times \underset{\sim}{X}$ be the scalar (term-by-term) matrix product of mask $\underset{\sim}{M}_{ij}$ and the image matrix $\underset{\sim}{X}$. We find that

$$(1/N)\sum_{n=0}^{N-1}\sum_{m=0}^{N-1} C(n, m) = T(i, j) \tag{13}$$

where $\underset{\sim}{T} = (1/N)\,\underset{\sim}{W}\,\underset{\sim}{X}\,\underset{\sim}{W}$. Thus, using $\underset{\sim}{M}_{ij}$ as a template on the image, and summing the elements of the resultant matrix scalar product, we obtain the (ij) term of the image's Walsh transform. If the image pattern correlates highly, either positively or negatively, with the mask $\underset{\sim}{M}_{ij}$ pattern, the (ij) term of the transform will be high. If the correlation is slight, the corresponding transform term will be small. This means that the patterns embodied in the masks can be studied to determine what image parameters will be detectable in the sequency plane.

Since $\underset{\sim}{M}_{00}$ consists of all +1's, we observe that the transform's T(0,0) terms must contain the average, or DC, value of the image X. This parameter is useful both in pattern recognition and statistical signal processing.

A study of the masks also tells us how lines or edges in the image plane appear in the sequency plane. A vertical line in the image plane will correlate most highly with masks $\underset{\sim}{M}_{00}$, $\underset{\sim}{M}_{01}$, $\underset{\sim}{M}_{02}$, etc., and thus will appear as a horizontal line in the sequency plane. Similarly, a horizontal line in the image plane transforms to a vertical line. In general, a line at angle θ_1 (θ_2) in the image plane will transform to a spectrum whose largest magnitudes fall along a line of angle ψ in the sequency plane (see Figure 2) with the following relationships:

$$\begin{aligned} &\text{for} \quad 0 \le \theta_1 \le -90°;\ \psi = -(90° + \theta_1), \\ &\text{for} \quad -90° \le \theta_2 \le -180°;\ \psi = 90° + \theta_2. \end{aligned} \tag{14}$$

$$\underset{\sim}{M}_{00} = \begin{bmatrix} 1 & 1 & 1 & 1 \\ 1 & 1 & 1 & 1 \\ 1 & 1 & 1 & 1 \\ 1 & 1 & 1 & 1 \end{bmatrix} \quad \underset{\sim}{M}_{01} = \begin{bmatrix} 1 & 1 & -1 & -1 \\ 1 & 1 & -1 & -1 \\ 1 & 1 & -1 & -1 \\ 1 & 1 & -1 & -1 \end{bmatrix} \quad \underset{\sim}{M}_{02} = \begin{bmatrix} 1 & -1 & -1 & 1 \\ 1 & -1 & -1 & 1 \\ 1 & -1 & -1 & 1 \\ 1 & -1 & -1 & 1 \end{bmatrix} \quad \underset{\sim}{M}_{03} = \begin{bmatrix} 1 & -1 & 1 & -1 \\ 1 & -1 & 1 & -1 \\ 1 & -1 & 1 & -1 \\ 1 & -1 & 1 & -1 \end{bmatrix}$$

$$\underset{\sim}{M}_{10} = \begin{bmatrix} 1 & 1 & 1 & 1 \\ 1 & 1 & 1 & 1 \\ -1 & -1 & -1 & -1 \\ -1 & -1 & -1 & -1 \end{bmatrix} \quad \underset{\sim}{M}_{11} = \begin{bmatrix} 1 & 1 & -1 & -1 \\ 1 & 1 & -1 & -1 \\ -1 & -1 & 1 & 1 \\ -1 & 1 & 1 & 1 \end{bmatrix} \quad \underset{\sim}{M}_{12} = \begin{bmatrix} 1 & -1 & -1 & 1 \\ 1 & -1 & -1 & 1 \\ -1 & 1 & 1 & -1 \\ -1 & 1 & 1 & -1 \end{bmatrix} \quad \underset{\sim}{M}_{13} = \begin{bmatrix} 1 & -1 & 1 & -1 \\ 1 & -1 & 1 & -1 \\ -1 & 1 & -1 & 1 \\ -1 & 1 & -1 & 1 \end{bmatrix}$$

$$\underset{\sim}{M}_{20} = \begin{bmatrix} 1 & 1 & 1 & 1 \\ -1 & -1 & -1 & -1 \\ -1 & -1 & -1 & -1 \\ 1 & 1 & 1 & 1 \end{bmatrix} \quad \underset{\sim}{M}_{21} = \begin{bmatrix} 1 & 1 & -1 & -1 \\ -1 & -1 & 1 & 1 \\ -1 & -1 & 1 & 1 \\ 1 & 1 & -1 & -1 \end{bmatrix} \quad \underset{\sim}{M}_{22} = \begin{bmatrix} 1 & -1 & -1 & 1 \\ -1 & 1 & 1 & -1 \\ -1 & 1 & 1 & -1 \\ 1 & -1 & -1 & 1 \end{bmatrix} \quad \underset{\sim}{M}_{23} = \begin{bmatrix} 1 & -1 & 1 & -1 \\ -1 & 1 & -1 & 1 \\ -1 & 1 & -1 & 1 \\ 1 & -1 & 1 & -1 \end{bmatrix}$$

$$\underset{\sim}{M}_{30} = \begin{bmatrix} -1 & 1 & 1 & 1 \\ -1 & -1 & -1 & -1 \\ 1 & 1 & 1 & 1 \\ -1 & -1 & -1 & -1 \end{bmatrix} \quad \underset{\sim}{M}_{31} = \begin{bmatrix} 1 & 1 & -1 & -1 \\ -1 & -1 & 1 & 1 \\ 1 & 1 & -1 & -1 \\ -1 & -1 & 1 & 1 \end{bmatrix} \quad \underset{\sim}{M}_{32} = \begin{bmatrix} 1 & -1 & -1 & 1 \\ -1 & 1 & 1 & -1 \\ 1 & -1 & -1 & 1 \\ -1 & 1 & 1 & -1 \end{bmatrix} \quad \underset{\sim}{M}_{33} = \begin{bmatrix} 1 & -1 & 1 & -1 \\ -1 & 1 & -1 & 1 \\ 1 & -1 & 1 & -1 \\ -1 & 1 & -1 & 1 \end{bmatrix}$$

Figure 1.

This gives rise to an angle ambiguity. If φ is known, the image plane angle ψ is either $-(\psi + 90^\circ)$ or $\psi - 90^\circ$, i.e. θ is a double-valued function of φ. A slight rotation of the image could be used to resolve the ambiguity in practice.

It should be noted here that the correlation masks can be applied to the transform plane and used to obtain the individual elements of the image, since the transform has been shown to be a self-inverse operation. Thus any algorithm or physical device to use these masks will be bi-directional.

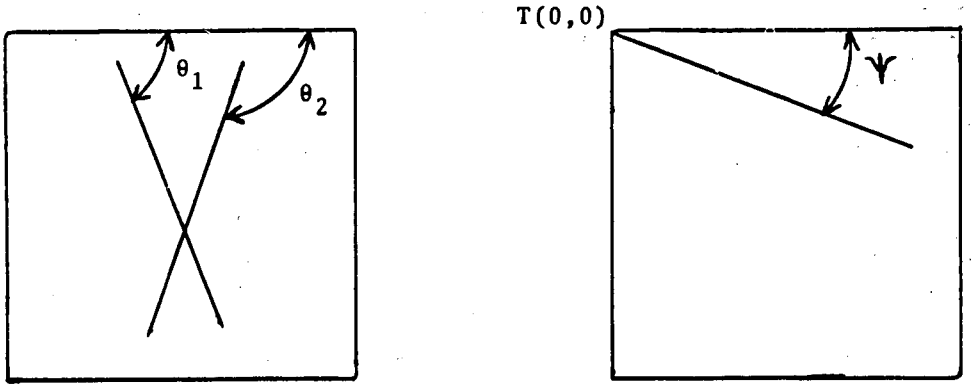

Image Plane $\underset{\sim}{X}$ Sequency Plane $\underset{\sim}{T}$

Figure 2.

One of the primary operations done in the frequency plane is filtering, and we would like to extend the concept to the sequency domain. As a common example, consider the application of high-pass filters in the frequency domain to bring out lines and edges in the reconstructed signal. The analogy between sequency and frequency leads to the idea of trying the same thing in the sequency domain. Here we run into a primary difference between the Walsh and Fourier transforms. High pass sequency filtering will indeed bring out edges, but the edges which are enhanced depend on where the image is located in the image plane. Thus, while the Fourier transform is translation invariant, the Walsh transform is not. If the image is moved vertically or horizontally, all the values in the sequency plane will change, in general.

In an attempt to get around this problem, a two-dimensional power spectrum was evolved which is translation invariant and which reduces the number of spectral data points from $(2^p)^2$ to $(p + 1)^2$ where $N = 2^p$ is the order of the Walsh matrix. The power spectrum is obtained via a matrix operator which sums the energies of certain frequency groups, namely the odd harmonics of 1, 2, 4, 8, 16 etc. cycles (not zero crossings). If we let $\underset{\sim}{V} = \underset{\sim}{T} \times \underset{\sim}{T}$ be the scalar matrix product of the Walsh transform matrix with itself, the power spectrum $\underset{\sim}{P}$ can then be defined as:

$$\underset{\sim}{P} = \underset{\sim}{A}\,\underset{\sim}{V}\,\underset{\sim}{A}^t. \tag{14}$$

Here the matrix operator $\underset{\sim}{A}$ is of order $p + 1$ by N. As an example, for $N = 16$, the matrix $\underset{\sim}{A}$ is defined in the function INPWR16 in the Appendix.

This power spectrum is translation invariant and preserves the average value and line angle information of the original transform. Its other pattern recognition aspects have not yet been studied.

V. CONCLUSIONS

In this paper, several properties of the Walsh transform have been noted which, by analogy to Fourier transform properties, show that the Walsh sequency plane has potential uses in filtering and bandwidth reduction schemes.

The pattern recognition aspects of the sequency plane were also investigated. It was shown that lines and edges in the image plane can be detected in the sequency plane. A set of "correlation masks" was developed which one can use to find certain other image patterns which can be identified in the Walsh spectrum. Since the Walsh transform is not translation invariant, it is difficult to get results which hold for arbitrary patterns. A type of power spectrum was evolved which is translation invariant and which preserves some of the parameter extraction properties of the original transform.

The characteristics reported here, along with the features of simplicity and efficient representation of digital signals, show the Walsh transform to be an important candidate for signal processing applications. A technique has recently been proposed [1] for obtaining the Walsh transform of an image optically, and as other physical implementations for taking the transform are devised, its use in signal processing is certain to grow.

BIBLIOGRAPHY

1. Decker, J. A. Jr., "Hadamard-Transform Image Scanning," Applied Optics, Vol. 9, No. 6, pp. 1392-1395, June, 1970.

2. Gibbs, J. E., "Walsh Spectrometry, A Form of Spectral Analysis Well Suited to Binary Digital Computation," Nat'l. Physics Lab. Rept., Teddington, Middlesex, England, 1968.

3. Habibi, A., and Wintz, P., "Optimum Linear Transformations for Encoding 2-Dimensional Data," Purdue Technical Report TR-EE69-15, May, 1969.

4. Harmuth, H. F., "A Generalized Concept of Frequency and Some Applications," IEEE Trans. on Information Theory, Vol. IT-14, pp. 375-382, May, 1968.

5. Harmuth, H. F., "Applications of Walsh Functions in Communications," IEEE Spectrum, Vol. 6, No. 11, pp. 82-91, November, 1969.

6. Harmouth, H. F., Transmission of Information by Orthogonal Functions, Springer-Verlag, New York/Berlin, 1969.

7. Henderson, K. W., "Some Notes on the Walsh Functions," IEEE Trans. on Electronic Computers, Vol. EC-13, pp. 50-52, February, 1964.

8. Kennett, B.L.N., "A Note on the Finite Walsh Transform," IEEE Trans. on Information Theory, Vol. IT-16, No. 4, pp. 489-491, July, 1970.

9. Lendaris, G., and Stanley, G., "Diffraction-Pattern Sampling for Automatic Pattern Recognition," IEEE Proceedings, Vol. 58, pp. 198-216, February, 1970.

10. Pratt, W. K., Kane, J., and Andrews, H. C., "Hadamard Transform Image Coding," IEEE Proceedings, Vol. 57, pp. 58-68, January, 1969.

11. Swick, D. A., "Walsh Function Generation," IEEE Trans. on Information Theory, Vol. IT-15, No. 1, p. 167, January, 1969.

12. Whelchel, J. E. Jr., and Guinn, D. F., "The Fast Fourier-Hadamard Transform and Its Use in Signal Representation and Classification," EASCON 68 Record, pp. 561-573, 1968.

APPENDIX

This portion of the paper contains the main APL programs which were used during the study. Some of them have been referenced in the text as examples of the operations performed. The whole set of functions is included to provide continuity and to show the simplicity and utility of the APL system for vector and matrix calculations. The first functions were written and running after only two day's introduction to the APL language and terminal. The functions are not optimized in terms of length or time, but they get the job done with a minimum of experience required.

INIT16 initializes the variables needed to work with Walsh functions of order 16. $N = 2^p$ is the order, M = p, and V is a row vector of length M, composed of 2's.

WALSH is the function which generates the Walsh matrix, IWALSH, of order N, according to the algorithm given in the text.

XFRM takes the Walsh transform of a square image matrix P of order N. The transform appears as the matrix TRANS.

FILTER initiates a filter mask matrix composed of all +1's. Appropriate elements are then set to zero to provide the desired filtering.

NEGINV takes the Walsh transform of the filtered sequency spectrum and reconstructs the filtered image amplitude.

INPWR16 initiates the matrix operator for obtaining the power spectrum (as developed in part IV) of an order 16 system. POWER16 then finds the power spectrum and displays it.

APPENDIX

APL Functions For Walsh Image Processing

```
      ∇INIT16[□]∇
    ∇ INIT16
[1]   N←16
[2]   M←4
[3]   V←4⍴2
[4]   IWALSH← 16 16 ⍴0
[5]   IWAL←16⍴1
    ∇
```

```
      ∇WALSH[□]∇
    ∇ WALSH
[1]   ORDER←¯1
[2]   ORDER←ORDER+1
[3]   IA←V⊤ORDER
[4]   ND←1
[5]   NN←2
[6]   MM←1
[7]   II←0
[8]   II←II+1
[9]   NND←NN
[10]  MULT←(1×(IA[MM]=0))+(¯1×(IA[MM]=1))
[11]  I←0
[12]  I←I+1
[13]  IWAL[NND]←MULT×IWAL[I]
[14]  NND←NND-1
[15]  →(12×(I<ND))+(16×(I=ND))
[16]  NN←NN×2
[17]  MM←MM+1
[18]  ND←ND×2
[19]  →(8×(II<M))+(20×(II=M))
[20]  IWALSH[ORDER+1;]←IWAL
[21]  →(2×(ORDER<(N-1)))+(22×(ORDER=(N-1)))
    ∇
```

```
      ∇XFRM[□]∇
    ∇ XFRM
[1]   INTER←P+.×IWALSH
[2]   TRANS←IWALSH+.×INTER
[3]   I←0
[4]   I←I+1
[5]   TRANS[I;]
[6]   →4×(I<N)
    ∇
```

```
      ∇FILTER[□]∇
    ∇ FILTER
[1]   F← 16 16 ρ1
    ∇
```

```
      ∇NEGINV[□]∇
    ∇ NEGINV
[1]   S←TRANS×F
[2]   IMED←S+.×IWALSH
[3]   IMAGEN←IWALSH+.×IMED
[4]   IMAGEN←(IMAGEN÷(N*2))
[5]   IMAGEN←⌊(10×IMAGEN)
[6]   'SIGNED IMAGE'
[7]   I←0
[8]   I←I+1
[9]   IMAGEN[I;]
[10]  →8×(I<N)
    ∇
```

```
      ∇INPWR16[□]∇
    ∇ INPWR16
[1]   A←16ρ 1 0 0 0 0 0 0 0 0 0 0 0 0 0 0 0
[2]   B←16ρ 0 1 1 0 0 1 1 0 0 1 1 0 0 1 1 0
[3]   C←16ρ 0 0 0 1 1 0 0 0 0 0 0 1 1 0 0 0
[4]   D←16ρ 0 0 0 0 0 0 0 1 1 0 0 0 0 0 0 0
[5]   E←16ρ 0 0 0 0 0 0 0 0 0 0 0 0 0 0 0 1
[6]   PT← 5 16 ρA,B,C,D,E
[7]   PTT←⍉PT
    ∇
```

```
      ∇POWER16[□]∇
    ∇ POWER16
[1]   TRSQR←TRANS×TRANS
[2]   G←TRSQR+.×PTT
[3]   POWER←PT+.×G
[4]   POWER
    ∇
```

PROPAGATION DELAY IN THE ATMOSPHERE

David M. Levine
Electrical Engineering Department
University of Maryland
College Park, Maryland

ABSTRACT*

The structure of the lower atmosphere and the ionosphere are discussed and an introduction to ray tracing the atmosphere is given. Models for each region appropriate for satellite-to-earth communication in the frequency range 1 GHz are discussed. Assuming a spherically symmetric atmosphere, propagation delay is computed for the lower atmosphere and for the ionosphere. The total atmospheric delay is also computed as a function of atmospheric conditions, frequency and altitude of the signal source.

*This work was published in X-521-70-404.

CURRENT INSTABILITIES IN OXYGEN-DOPED GALLIUM ARSENIDE

Alfred George Lieberman
Department of Electrical Engineering
University of Maryland
College Park, Maryland

RESEARCH SUMMARY

Electrical current passing through prepared gallium arsenide was observed to display large amplitude, low frequency oscillations when suitably illuminated and properly refrigerated. Oxygen-doped gallium arsenide samples having a room-temperature, dark resistivity of $8.6 \times 10^4\ \Omega$ cm were found, at 100°K, to exhibit at least two distinct modes of oscillation. The threshold electric field required to sustain oscillation is determined by the wavelength of the incident light and the mode of oscillations. The lower threshold mode exhibits a sinusoidal current waveform. At larger electric field intensities a second threshold exists at which the current waveform abruptly changes into a repetitive spike of slower periodicity. Pronounced photoexcitation is observed for wavelengths between $0.9\ \mu$ and 1.6μ, corresponding to the energies separating the conduction band from the valence band and the oxygen dopant levels. For a given mode, the threshold field is observed to depend upon the wavelength of the incident light; the frequency of oscillation is determined by the intensity of the light and the length of the crystal sample. Threshold field intensities vary from a few tens of volts/cm for the sinusoidal mode to several hundreds of volts/cm for the spike mode. Crystal samples were cut and polished to dimensions typically 0.5 mm × 1 mm × 2 mm.

ACKNOWLEDGMENT

The author is grateful for having had an opportunity to work with the Materials Research and Development Branch. In particular, he is indebted to his colleague, Tom Sciacca, for providing laboratory facilities and for many stimulating discussions relating to present and future research problem areas. Many thanks are also due to Walter Viehmann for suggesting the problem summarized above and for acquainting the author with the intricate laboratory techniques of crystal preparation.

SPACECRAFT POWER SYSTEMS

Frederick H. Morse
Department of Mechanical Engineering
University of Maryland
College Park, Maryland

My research colleague at NASA was Mr. Joseph Epstein, Head Advanced Power Sources Section, Code 761. Two projects were selected for study.

One project was to develop a method to predict the change in the specific power of the various satellite energy conversion systems, presently being used or under various stages of development, as the satellite power level increases. In this study specific power is defined to be the orbit average regulated system weight. A set of relationships were to be developed that would show, for any energy conversion system, how the weight of the power system changed as the load requirement increased. The predicted variation in specific power with power level was to be compared with data from actual satellite power systems. A survey of satellite power systems was conducted to provide such data.

The analysis, covering solar cell, isotope, thermoelectric, thermionic, magneto-hydrodynamic and dynamic cycle energy conversion systems, has not been completed. The survey of satellite power systems, all utilizing solar cells as the primary energy conversion device, has been completed. Of the approximately one hundred twenty non-military satellites launched since 1959 sufficient power system data was found for only fifteen. Additional data on five satellites presently being built were also obtained. Several preliminary observations can be made.

1. The maximum specific power is 1.5 watts/1 bm.

2. For earth orbiting satellites (with the exception of the Intelsat satellites) a maximum specific power of approximately 1.1 watts/1 bm occurs at the 100 watt power level. Low power satellites (20-40 watts) have a typical specific power of 0.6 watts/1 bm while high power satellites (100-300 watts) have a typical specific power of 0.9 watts/1 bm.

3. Over the last ten years the specific power has gradially increased. Satellites in any series, such as the Nimbus series, always show an increase in specific power with power level.

The second project was to investigate the feasibility of a hybrid thermoelectric-thermionic power system. In order to prevent back emission, resulting in a decrease in output power, the anode of a thermionic generator must be cooled. At present this cooling is accomplished by heat rejection to space. In the hybrid system this heat will pass thru a thermoelectric generator thereby converting a portion of this rejected energy into electrical energy. The analysis of this system is continuing.

ELECTRONS IN AURORA

Victor J. Newton
Fairfield University
Fairfield, Connecticut

and

Lennart R. Peterson
University of Florida
Gainesville, Florida

An experimental program for measuring auroral atmospheric emissions in the infrared, visible, and ultraviolet wavelength regions has been developed by D. F. Heath at this Center. The program includes ground based as well as rocket and satellite instruments. Of particular interest is Heath's 1 meter Ebert-Fastie spectrometer, which is capable of rapid scanning at high resolution over an auroral band, as viewed from the ground. This is a rather useful measurement to make since it has been shown that the temperature of the emitting region can be reasonably well inferred from the data. For this purpose the N_2^+ 3914 Å (0,0) band is especially well suited.

A complete theoretical analysis of auroral phenomena involves detailed knowledge of the density and temperature structure of the atmosphere, the electron- and to some extent ion-impact cross sections for exciting each state, the magnetic and electic field components, and finally the incident particle flux spectrum. For most auroras, electrons are the dominant source of excitation as they degrade from their initial incident energies. Thus, for example, in order to predict the height profile of the 3914 Å (0,0) band, one must know how electrons deposit their energy as a function of altitude.

The initial work in the overall problem has been to find a simple way of correlating a given incident electron spectrum to the resulting 3914Å emissions and to examine how these emissions, integrated along a line of sight are seen from the ground. For simplicity, initially we have assumed that a mono-directional steady-state beam of electrons is incident on a layer of gas, thin with respect to the total range of the electrons in the gas. After passage through the gas, the electrons will have lost some of their energy through excitation and ionization processes, and what emerges is a flux distribution. For the most part, inelastic collisions are predominantly forward scattering; thus, we assume no deviation from a straight line path. Although this is not completely realistic it is hoped that phenomenological corrections can be brought in to produce agreement with experiment and with more detailed Monte Carlo calculations. As a test, the results should be somewhat consistent with a Landau distribution.

We consider the energy spectrum to be divided into a series of bins of specified width ΔE, and write the density $N_i(\vec{r})$ of electrons in the ith bin, as a function of the position $\vec{r}$. We expect this density to follow a continuity equation including a source term to account for electrons being deposited in the ith energy bin through deposition from higher energy bins, and a loss term to account for deposition from the ith bin to lower energy bins. We can write, therefore:

$$\frac{\partial N_i(\vec{r})}{\partial \tau} = \vec{v}_i \nabla \vec{N}_i(\vec{r}) = -\frac{N_i(\vec{r})}{\tau_i(\vec{r})} + \sum_{j<i} \frac{N_j(\vec{r})}{\tau_j(\vec{r})} \frac{\Delta \sigma_{ji}}{\sigma_j} \tag{1}$$

where we have labeled the bins consecutively such that j = 1 corresponds to the highest energy bin. The collision time $\tau_j(\vec{r})$ of an electron of energy E is related to the mean free path $\lambda_j = v_j \tau_j$. In this equation the ratio of partial to total cross sections $\Delta\sigma_{ji}/\sigma_j$ represents the probability that an electron will go from bin j to bin i.

Considering a one-dimensional steady state solution for a mono-energetic beam of electrons impinging on a slab of gas of density n(x), the continuity equation simplifies to

$$\frac{d N_i(x)}{d x} = -\frac{N_i(x)}{\lambda_i(x)} - \sum_{j<i} \frac{v_j}{v_i} \frac{N_j(x)}{\lambda_j(x)} \frac{\Delta\sigma_{ji}}{\sigma_j} \tag{2}$$

where $\lambda_i(x)$ represents the mean free path for particles in bin i. Since $\lambda_i(x) = 1/\sigma_i n(x)$ and since the electron flux $I_i(x)$ is just $N_i(x)v_i$, it is convenient to translate Eq. 2 into the flux equation:

$$\frac{d I_i(y)}{d y} = -I(y)\sigma_i + \sum_{j<i} I_j(y)\Delta\sigma_{ji} \tag{3}$$

in which a change of variable dy = n(x)dx has been introduced. The procedure is to solve Eq. 3 to obtain the electron flux, and thereby the volume excitation and ionization rates as a function of altitude and incident energy flux.

Equation 3 can be solved analytically, in the case where no two cross-sections σ_j are exactly equal, by a finite series solution:

$$I_i(y) = \sum_{j\le i} A_{ij} e^{-\sigma_j y} \tag{4}$$

where the coefficient A_{ij} satisfy the recursion relation:

$$A_{ij} = \frac{1}{\sigma_i - \sigma_j} \sum_{j\le k\le i} A_{kj}\Delta\sigma_{ki}, \quad i > j \tag{5}$$

and the boundary condition:

$$\sum_{j\le i} A_{ij} = I_i(0) \tag{6}$$

The advantage of this solution is its simplicity; numerically however, sizeable round-off errors can occur which makes it difficult to work with. An alternative solution may be obtained by solving for the Green's Function of Eq. 3. Here the solution to the source equation

$$\left(\frac{d}{d\,y} + \alpha_i\right) g_i\,(y,\ y') = \delta\,(y - y') \tag{7}$$

subject to the boundary condition of particles traveling in the positive direction is:

$$g_i\,(y,\ y') = \begin{cases} e^{-\sigma_i (y-y')}, & y > y' \\ \\ 0, & y < y' \end{cases} \tag{8}$$

which yields a solution to Eq. 3 of the form

$$I_i\,(y) = \left[I_i\,(0) + \sum_{j<i} \int_0^y d\,y'\ I_j\,(y')\ e^{\sigma_i y'}\ \Delta\sigma_{j\,i} \right] e^{-\sigma_i y} \tag{9}$$

which can be solved numerically. The advantages of this solution are that the terms within the sum in Eq. 9 are all positive, resulting in a negligible round-off error, and that the terms in the solution can be interpreted physically.

The analytical form of the solution to Eq. 3 has been programmed using recent cross-sections in phenomenlogical form. These studies have not yet produced concrete results, but preliminary indications are encouraging for many conditions.

CODING AND THE SPACEBORNE ATOMIC CLOCK*

Jacob C. Sabto
Department of Electronic Engineering
California State Polytechnic College
San Luis Obispo, California

ABSTRACT**

A satellite-borne atomic clock would be the crucial component in a communications network which could be synchronized to an accuracy approaching one microsecond. With such synchronization accuracy, the technology of time and frequency measurement would take a leap which, when translated into practical achievements, would open new vistas to the solution of problems in such fields as submicrosecond world-wide time synchronization, space communication, navigation, air traffic control, etc.

Mr. A. R. Chi has proposed the orbiting of such a clock in a report* submitted to NASA Headquarters. We describe in this document a typical implementation of Mr. Chi's proposal and consider one particular aspect of the system, namely coding techniques for transmitting information. Before discussing these techniques, it is useful to briefly describe the overall system in order to better appreciate the role of coding within the system.

*A proposal for the Support of the Development of a Space Borne Atomic Clock," May 1970, submitted to the Advanced Applications Flight Experiments Program Office, NASA Headquarters, Washington, D.C.

**This is being published under X-521-71-81.

A RANDOM DISTRIBUTION OF RADIAL MOTIONS

William R. Thickstun
Department of Mathematics
Clarkson College of Technology
Potsdam, New York

ABSTRACT

Two quite unrelated problems motivated the efforts described in this report. One pertains to the question of whether a singularity in space time can develop from an initially non-singular distribution of matter. The other problem pertains to the initial distribution of comet orbits about the sun from which certain "capture" theories attempt to predict the observed number of short period comets. For both of these problems it is instructive to start with a model consisting of a random distribution of particles constrained, however, to strictly radial motion in a central gravitational field.

*This paper was published under X-643-70-303.

ELECTRON PARAMAGNETIC RESONANCE OF V^{2+}, Mn^{2+}, Fe^{3+} AND OPTICAL SPECTRA OF V^{3+} IN ZOISITE $Ca_2 Al_3 Si_3 O_{12}$ (OH)

Tung Tsang
Department of Physics
Howard University
Washington, D. C.

and

Subrata Ghose
Planetology Branch
Goddard Space Flight Center
Greenbelt, Maryland

ABSTRACT*

Electron paramagnetic resonance and optical absorption spectra have been used to clarify the local environments of transition metal ions and their distributions among various Al- and Ca-sites in a gem quality zoisite crystal from Tanzania. The EPR spectra due to Mn^{2+}, Fe^{3+} and two types of V_{2+} have been interpreted by the spin Hamiltonian

$$\beta \mathbf{H}\cdot\mathbf{g}\cdot\mathbf{S} + \mathbf{I}\cdot\mathbf{A}\cdot\mathbf{S} + D\left[S_g^2 - \frac{1}{3}S(S+1)\right] + E(S_x^2 - S_y^2)$$

in the principal axes system x, y, z. The Mn^{2+} ions occupy one of the Ca-sites, probably Ca(1), with point group symmetry m; $g = 2.003 \pm 0.005$ and $|A| = (85 \pm 2) \times 10^{-4}$ cm^{-1}, both isotropic and also $|D| = (103 \pm 5) \times 10^{-4}$ cm^{-1}, $|E| = (34 \pm 2) \times 10^{-4}$ cm^{-1}, in general agreement with other oxides and hydrates. Highly anisotropic hyperfine and small zero-field splittings ($|D| < 0.014$ cm^{-1}) are observed for V^{2+}, which is the opposite of the usual situation. One of the two types of V^{2+} apparently occupies the same site as Mn^{2+}; the other V^{2+} ion is in a general position, and probably occupies a double minima potential around the Ca(2) site. The Fe^{3+} ions occupy the Al_{II} site, since the point group symmetry is m; the principal axes, however, are displaced approximately 45° from the NMR axes of ^{27}Al. Apparently, the local environment changes when Al^{3+} ions are replaced by Fe^{3+}. For Fe^{3+}, we found $|D| = 0.14 \pm 0.03$ cm^{-1} and $|E| \sim 0.1\ |D|$. The optical absorption of V^{3+} and the trichroism of the zoisite single crystal are consistent with the two types of Al^{3+} site symmetries, with crystal field parameters Dq = 1850 and 1400 cm^{-1} at Al_I and Al_{II} sites.

---

*This X644-70-319 to be published in: The J. Chem. Phys. (Spring 1971).

REDUCTION OF OAO-II STAR TRACKER FLIGHT DATA

Robert E. Wilson
Department of Astronomy
University of South Florida
Tampa, Florida

With the help of programmer Sy Lee, I have been attempting to analyze data from OAO history tapes to ascertain the dependence of measured star brightness on electron temperature telescope temperatures, catalog magnitude, and other parameters. Difficulties in data retrieval have prevented completion of this project, so we plan to communicate by telephone for the next several months until it's satisfactorily concluded. When it is in the production stage, it will be possible to quickly determine the sensitivities of the trackers as functions of any relevant variable.

I have also been making use of the 360-01 computer for a project which is too large for the 360-65 in Tampa. This involves fitting a new binary star model to observations of MR Cygni, a well observed eclipsing system. This was done in two stages - by intuitive adjustments and by differential corrections, and the final corrected set of parameters gives a very good representation of this data. I have been invited to speak about this work at the XIV General Assembly of the International Astronomical Union, in Brighton, England. The paper will be given in late August.

DIGITAL SIMULATION OF FCFB LOOP OPERATION IN RFI AND SPECULAR MULTIPATH

Rodger E. Ziemer
Electrical Engineering Department
University of Missouri - Rolla
Rolla, Missouri

ABSTRACT*

A digital computer simulation of an FCFB loop operating in interference and specular multipath is developed. Results from several test simulations of the loop operating under various conditions are presented to demonstrate the usefulness of the model and give an indication of the effectiveness of FM spread spectrum in combatting multipath and interference. Comparisons are made with an ideal discriminator, using normalized mean-square error between the output with and without interference present at the input as the performance measure. These preliminary results indicate that the FCFB loop is about 100 times better than the discriminator in suppressing the deleterious effects of RFI and multipath under the conditions simulated. The results also are intuitively satisfying in that increasing the modulation index of the signal and feedback factor of the loop generally lowers the mean-square error assuming suitable choices are made which avoid extraneous distortion effects.

*This paper was published under X-525-70-329.

ERFRAC: A COMPUTER PROGRAM FOR RESEARCH INTO THE CORRECTION OF ERRORS IN SATELLITE RADIO TRACKING DUE TO ATMOSPHERIC REFRACTIONS

Bruce H. Morgan
U. S. Naval Academy
Annapolis, Maryland

* This work was performed in a previous year.

ERFRAC: A Computer Program for Research into the Correction of Errors in Satellite Radio Tracking Data Due to Atmospheric Refraction

Table of Contents

Appendices

ERFRAC: A COMPUTER PROGRAM FOR RESEARCH INTO THE CORRECTION OF ERRORS IN SATELLITE RADIO TRACKING DUE TO ATMOSPHERIC REFRACTIONS

Bruce H. Morgan
U. S. Naval Academy
Annapolis, Maryland

1. INTRODUCTION

My previous report on this project appeared in the Final Report of the 1968 ASEE-NASA Summer Faculty Fellowship Program (X-520-69-30) on pages 111-132. This report is cited below as Reference (1). A brief introduction to the problem dealt with is given in this section, but the reader is referred to that previous paper for detailed derivations and a list of citations to the literature.

Because of refraction, radio waves transmitted from an earth satellite follow a curved path down through the atmosphere. Consequently, the direction in which they are traveling when they reach an observer on the ground is in general different from the direction of a straight line from the satellite source to the observer.

The difference between these directions, is called the angular error at the observer. Its magnitude depends in general upon the frequency of the radio signal, the state of the atmosphere – troposphere and ionosphere – at the time of observation, and upon the angular elevation of the radio source above the observer's horizon. At the Minitrack System operating frequency of 136 MHz, is is on the order of one or two minutes of arc for an elevation angle of 60°. Since apart from this refraction error, the Minitrack operational accuracy is about 20 seconds of arc, it is clearly desirable to apply a refraction correction to the tracking data. The problem is how to determine this correction. Synoptic ionospheric predictions are not adequate for this purpose, particularly in view of the frequent occurrence of "TIDs," traveling ionospheric disturbances, which cause irregular fluctuation of perhaps one or two minutes of arc in the apparent position of a (136 MHz) radio source with a period of half an hour or so. Clearly, then, some method of determining the refraction error at the time and place of observation is needed if the potential operational accuracy of the Minitrack system is to be attained in practice.

One possible approach is to observe the directions of arrival of radio waves from the same source at two different frequencies. Because the ionosphere is dispersive, these two directions will not be the same. The difference between them is a measure of the state of the ionosphere along the path from source to observer and hopefully enable the observer to determine what correction should be applied for refraction.

My fellowship time this summer (1969) has been devoted to developing a computer program (ERFRAC) to trace the path of a radio wave through a model atmosphere which includes optionally, a "wedge" of election density at an arbitrary location and orientation, simulating the presence of an ionospheric irregularity. The program is based on the differential equations for the ray path (Euler-Lagrange equations) that derive from Fermat's Principle of geometrical optics. This derivation is set forth in Appendix B. By making a small change in just two lines of the program, the user can employ either of two standard subroutines DRKGS or DHPCG, from the IBM Scientific Subroutine Package, to carry out the step by step numerical integration of these differential equations: Subroutine DRKGS uses a Runge-Kutte technique, while DHPCG employs a predictor-corrector method. Both are written in double-precision mode, which means that 16 significant figures are carried in all the calculations.

The program as presently written uses only the simplest approximation for the relation between electron density and refractivity in the ionsophere. In particular, the effect of the earth's magnetic field, which causes double refraction, is not included. A better approximation could be incorporated into the existing program and corresponding effects, such as Faraday rotation, could be computed.

The author will be happy to talk with anyone who is interested in making use of ERFRAG, in whole or in part. Mail address: Physics Department, U. S. Naval Academy, Annapolis, Md. 21402. Telephone: 301-268-7711, extension 393.

2. GEOMETRY OF THE CALCULATION

Figure 1 shows the coordinate system used in the present work. The origin of coordinates is taken at the center of the earth. The x axis is oriented to pass through the point of observation; this direction is referred to in this paper as the observer's vertical. The y-axis is taken parallel to the observer's east, and the z-axis, north. This choice was made because in the Minitrack system, the direction cosines of the line to a satellite source are computed with respect to the observing station's eastward and northward base lines. These direction cosines are by convention called L and M, respectively.

The radio signal originates at the satellite and travels downward through the atmosphere to the observer's receiving antenna. For purposes of computation, however, it is convenient to consider a hypothetical "reversed ray" which originates at the observer

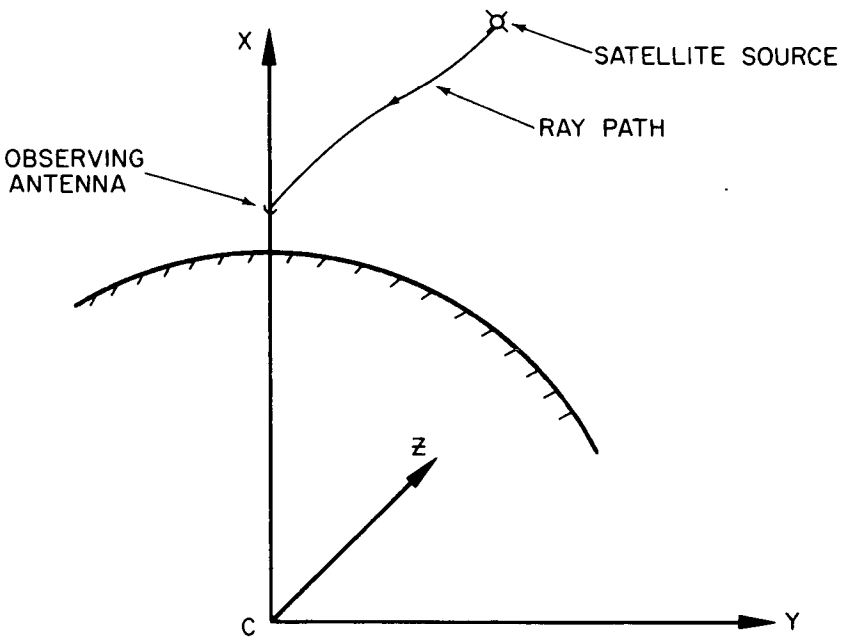

Figure 1. Basic Geometry of the Calculation.

and travels upward. This reversed ray will follow exactly the same path as would a downward-traveling ray, since by Fermat's Principle, both will travel that path which makes the transmission time an extremum. We simply must start the reversed ray off from the observer with an azimuth and elevation angle equal to those that the downward-traveling ray has when it reaches him. The path of the reversed ray is described by taking x as the independent variable and finding the y and z coordinates of the path as functions of x.

3. SUBROUTINE PERFORMANCE: DRKGS AND DHPCG

The Euler-Lagrange equations for the ray path are a pair of simultaneous second-order differential equations which can be solved algebraically to give formulas for $y_{xx} = d^2y/dx^2$ and $z_{xx} = d^2z/dx^2$ where the functions y(x) and z(x) are the y and z coordinates of a point on the ray path as functions of x.

In order to carry out the integration of these equations to determine y(x) and z(x), I decided to make use of one of the subroutines provided in the IBM Scientific Subroutine Package. Using the Goddard 360/91 computer, these subroutines are accessible directly from the RITS, or CRBE, remote terminals at Goddard. Preliminary calculation had indicated that double precision (16 significant figure) accuracy might be needed. Two suitable subroutines were available in the Package: DRKGS and DHPCG. The first utilizes a Runge-Kutta procedure; the second, a predictor-corrector method.

To check out and compare the operation of these two subroutines, and to become familiar with their use, I wrote programs which employed them to integrate a pair of second order equations which have simple analytic solutions namely:

$$y_{xx} = -y \tag{12-1}$$

$$z_{xx} = -z \tag{12-2}$$

These were integrated from x = 0, to x = 7. For the initial conditions which J specified, y(0) = 0.0, $y_x(0) = 1$, z(0) = 1, and $z_x(0) = 0.0$, the analytic solutions are, of course,

$$y_{EXACT} = \sin x \tag{12-3}$$

$$z_{EXACT} = \cos x \tag{12-4}$$

Therefore, the errors in the computer's calculated values were simply

$$\delta y = y(x) - \sin x, \tag{12-5}$$

and

$$\delta z = z(x) - \cos x \tag{12-6}$$

Trials showed that, as might be expected, these errors, at any given value of x tended to become smaller as the step size, $h = x_{i+1} - x_i$, used by the integrating subroutine, was made smaller. Also, δy and δz tended to increase with x, which also would be expected. Although each one individually oscillates as a function of x, the sum of their absolute values,

$$E = (|\delta y| + |\delta z|),$$

exhibited a fairly steady increase with x.

The results of the trials are summarized in Figure 2. This shows the magnitude of the combined error E at x = 6.0 as a function of integration step size h. E is plotted on the vertical axis in a quasi-logarithmic manner. On the horizontal axis is plotted the subroutine variable IHLF which is the number of times that an initial input parameter is cut in half to arrive at the step size used by the integrating subroutine. In all trials shown, this parameter was 0.1, so the step-size that was used by the computer is $0.1/2^{IHLF}$. In a few trials, the computer gave IHLF one value for some steps and a different value for others. The point on the graph for such trials is plotted half-way between the two values used. Both DRKGS and DHPCG assign a value to IHLF by comparing a "truncation error" which they compute at each integration step with an "upper error bound," which is supplied by the user as an input parameter, called PRMT(4). This parameter affects the computation only through its role in setting the value of IHLF.

The graph, Figure 2, confirms that the error in the result decreases as the integration step size is made smaller (IHLF larger) for both DRKGS (circles) and DHPCG (triangles). However, both curves flatten out at an error, E, of about 10^{-13}. To check

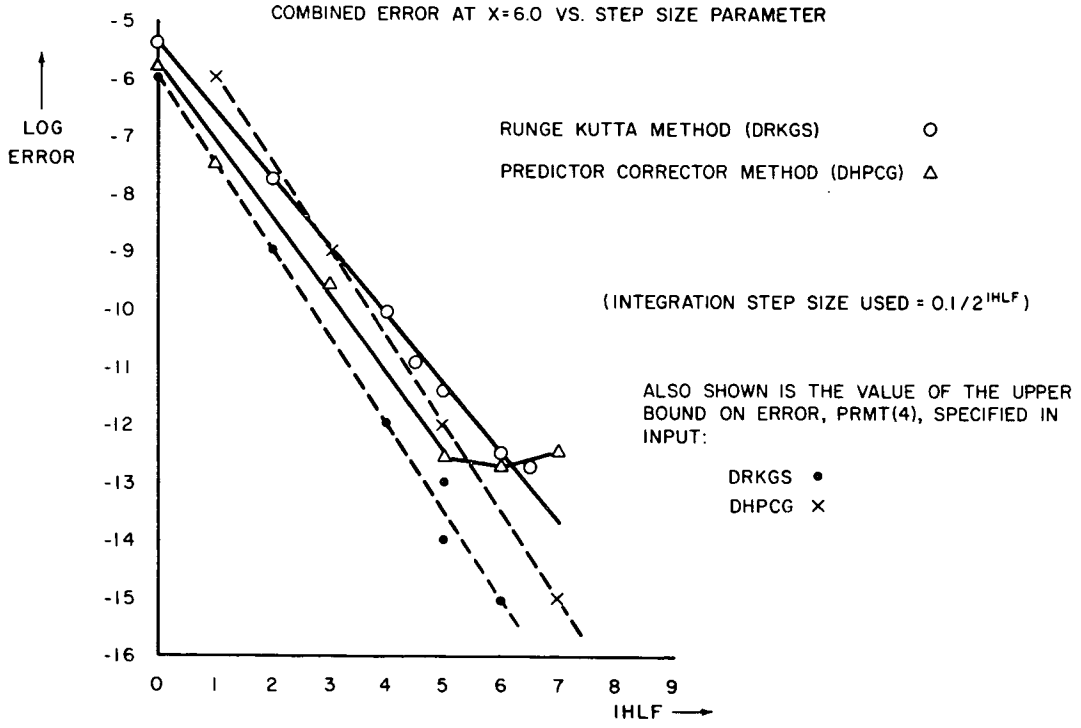

Figure 2. Combined Error at X = 6.0 vs Step Size Parameter.

this behavior, similar curves were plotted in Figure 3, for the error E in the results at x = 4.0 radians. (Recall that in figure 2, the error plotted was that at x = 6.0 radians.) Again, the two curves each bottom at an E of about 10^{-13}. The DRKGS curve reaches its minimum at a stepsize of about 0.1/2 .

At both x = 4 and x = 6, then, the result obtained by integration of the differential equation is good only to 13 significant figures, although the calculations are all carried out with 16 figures.

Figure 4 shows a similar behavior when DRKGS was used to integrate the equation $d^2y/dx^2 = e^x$ with initial conditions y(0) = 1.0 and y (0) = 1.0, for which the analytic solution is $y = e^x$. In this case, the error at x = 4.0 reaches a minimum of about 10^{-11}, where the step size used is about $0.1/2^5$.

It would be of interest to continue these curves to still smaller step size by making additional computer runs. The time available for the project did not permit this. However, it appears clear that in all cases, accuracy does not improve when the step-size is reduced beyond a certain point. Whether it actually becomes worse to a significant extent is not known, but is quite possible.

This optimum step size in the cases studies was such that from one thousand to four thousand steps filled the range of integration. This suggests that in ERFRAC, where

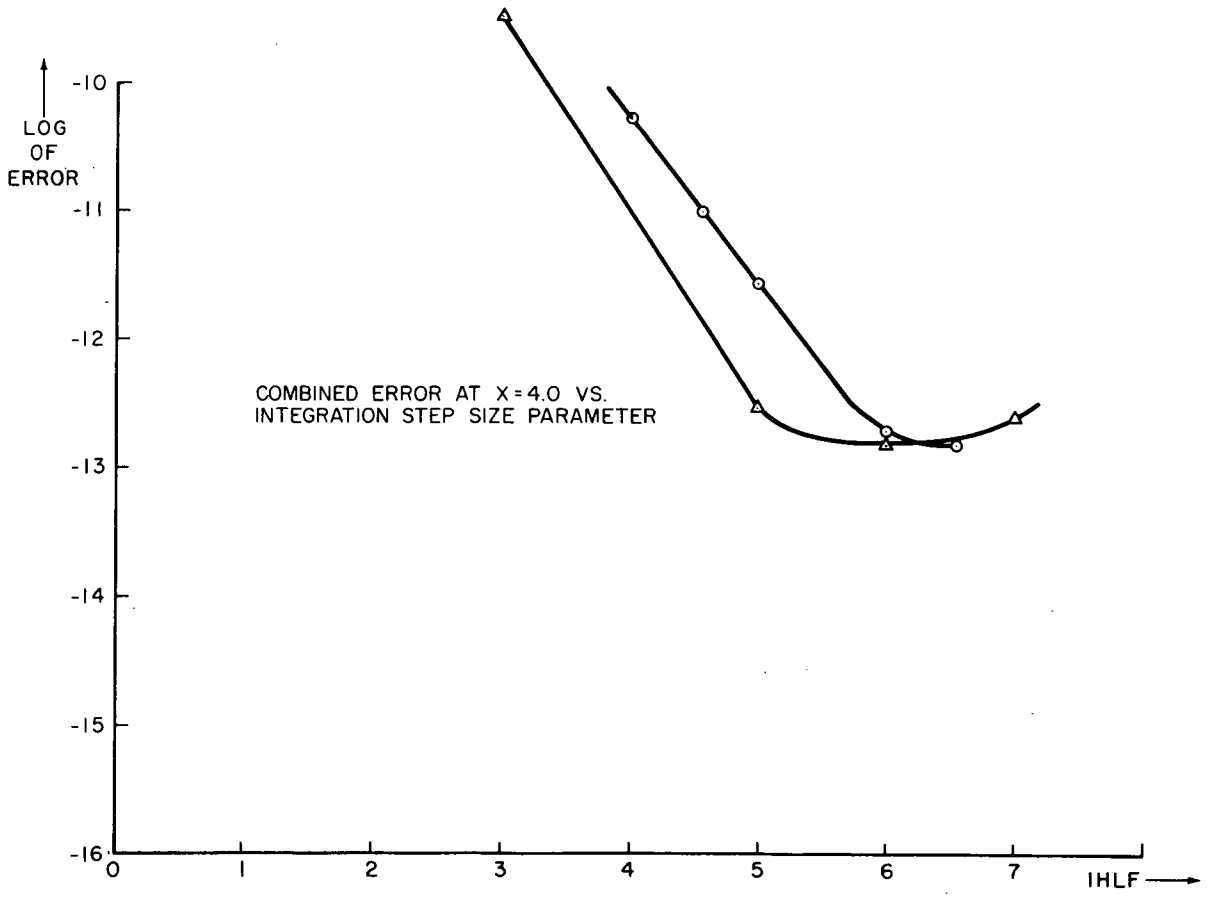

Figure 3.

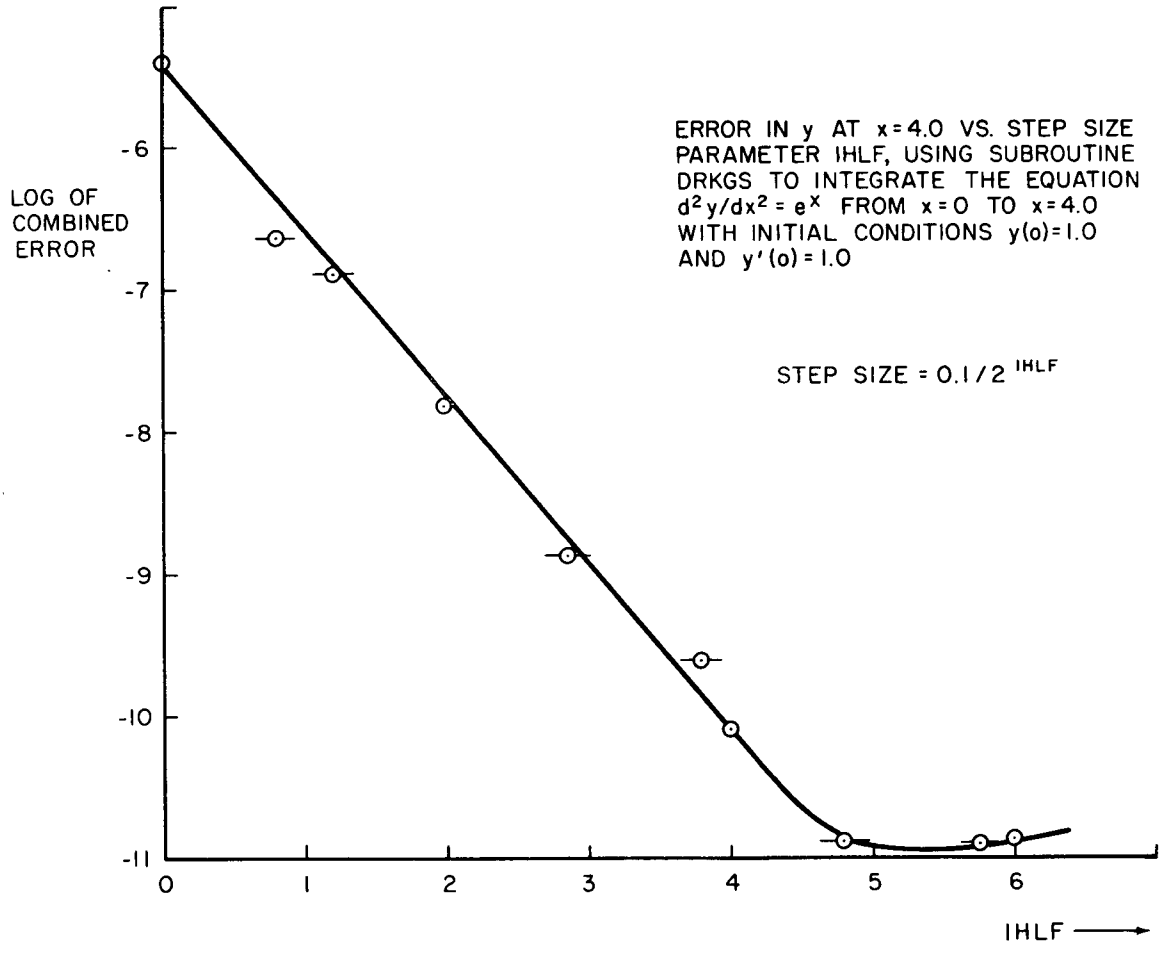

Figure 4. Error in y at x = 4.0 vs. Step Size Parameter IHLF, Using Subroutine DRKGS to Integrate the equation $d^2y/dx^2 = e$ from x = 0 to x = 4.0 with initial conditions y(0) = 1.0 and y (0) = 1.0

the range of interest of the independent variable x is from zero to a few hundred or perhaps to one or two thousand kilometers, a step size of one kilometer might be a good choice so far as accuracy of the computed ray path is concerned.

4. COMPARISON OF SUBROUTINES DRKGS AND DHPCG

A primary objective of the trials described in the previous section was to compare the performance of the subroutines DRKGS and DHPCG in order to decide which one to use in ERFRAC. Possible criteria that could be used in making this comparison include the degree of accuracy which is attainable; the amount of computer time required to produce a given degree of accuracy in the output; and the dependability or predictability of achieving a given degree of accuracy. The trials indicate that DHPCG and DRKGS are about equal under the first criterion, DHPCG is definitely superior under the second criterion, and DRKGS is perhaps somewhat superior under the third. My conclusion from these trials was to utilize DHPCG.

With regard to the first criterion, Figures 2 and 3 show that, while the error in the output of DHPCG using a given integration step-size was less than that of DRKGS, both DRKGS and DHPCG appear to have about the same ultimate limit of accuracy. This limit for each was at a "combined error," E, equal to about 10^{-13} and occurred for both at about the same step-size, namely $h = 0.1/2^6$.

With regard to the second criterion, we note first from Figure 2 that for a given step-size, the error in the output of DRKGS is from five to ten times as large as that of DHPCG, at least down to a step-size where both subroutines approach their ultimate limit of accuracy. (This limit, as pointed out above, is about the same for each.) Secondly, calculations in Appendix G, using the computer time charged to the trial run jobs, indicate that, again for a given step size, the time required by DHPCG to complete a run over a given range of x is about one third less than that required by DRKGS. So for a given step size, DHPCG is both more accurate and takes less time.

This comparison can be made somewhat more quantitative; by the following reasoning: Since the time required by DHPCG at a given step-size is 1/3 less than that required by DRKGS, DHPCG could use a step-size 1/3 smaller than DRKGS does and finish in the same time. But from Figure 2, a step-size 1/2 as large leads to an error of only about 1/12 as much. A reduction in step-size of 1/3 should therefore reduce error by a factor of about 2/3 of 12, or 8. Since the error of DHPCG at the original step-size was already only 1/5 to 1/10 of that of DRKGS, the conclusion is that in a given time, DHPCG could produce results with errors only some 1/40 to 1/80 as great as DRKGS.

Finally, with regard to the third criterion, it appears from Figure 2 that the trend toward smaller error with smaller step size is somewhat more regular for DRKGS than for DHPCG. In other words, the data points plotted there for DRKGS fall more nearly on a straight line than do those for DHPCG, until the ultimate limit of accuracy is approached. This indicates that the accuracy of DRKGS is somewhat more predictable than that of DHPCG. I believe, however, that the difference in this respect shown by Figure 2 is not large and is not very important, and that therefore this factor is not entitled to much weight.

5. THE BASIC ALGORITHM OF ERFRAC

As mentioned above, the basis for ray tracking used in this project is a pair of second order differential equations for the ray path derived in Appendix B of Reference (1). These equations relate the curvature of the path, expressed in rectangular coordinates, to the slope of the path and the magnitude and space derivatives of the local radio refractive indeix, μ. The subroutines DRKGS and DHPCG are each designed to integrate a system of first-order differential equations. But two second-order equations can easily be written as a system of four first-order ones by a well-known reformulation.

First, since the refractive index μ and its derivatives are functions of position; we can write our two second order equations as follows:

$$d^2 y/d^2 x = \dot{g}(x, y, z, y_x, z_x) \qquad (18\text{-}1)$$

$$d^2 z/d^2 x = h(x, y, z, y_x, z_x) \qquad (18\text{-}2)$$

In order to conform with the variable names used in DRKGS and DHPCG, we now define:

$$y = y_1 \quad \text{and} \quad z = y_3, \tag{18-3}$$

and we also introduce:

$$y_x = d\,y/d\,x = y_2 \quad \text{and} \quad z_x = d\,z/d\,x = y_4 \tag{18-4}$$

Then we can write

$$d\,y_1/d\,x = d\,y/d\,x = y_2 \tag{18-5}$$

$$d\,y_2/d\,x = d^2\,y/d\,x^2 = g\,(x,\ y_1,\ y_3,\ y_2,\ y_4) \tag{18-6}$$

$$d\,y_3/d\,x = d\,z/d\,x = y_4 \tag{18-7}$$

$$d\,y_4/d\,x = d^2\,z/d\,x^2 = h\,(x,\ y_1,\ y_3,\ y_2,\ y_4) \tag{18-8}$$

These last four equations are a set of first order equations with independent variable x and dependent variables y_1, y_2, y_3, and y_4. They constitute the basis of the actual computer program.

6. PROGRAM LOGIC IN ERFRAC

The purpose of this section is to provide an explanation of the logic in ERFRAC. A flow chart of the program is given in Fig. 5 and a listing of the source deck in Fig. 6. The reader may also refer to the list of variable names and other program terminology given in Appendix A.

The explanation in this section is keyed to the "ISN" numbers which appear in the left margin of the source deck listing in Fig. 6.

(Note: The argument lists for both of the user-provided subroutines; FCT and OUTP, are specified by the IBM subroutine DHPCG. My program ERFRAC, as written, uses variables in these lists to pass initialization data from the main program to the subroutines and from one subroutine to another. This could alternatively be done by the use of COMMON storage.)

ISN Main Program	Comment
5a, 5b	Comment mark avoids execution of READ statement when data is specified in the program, as it is for this run (in lines 9 to 13).

ISN Main Program	Comment
6-8	Set up DO loops for this particular run, to sample effect of various values of HWGB (line 23), AZWG (line 24), and FREQ (line 22)
14, 15	These steps were provided so that the start and end of the range of x over which the radio ray path is to be traced can be specified on input in terms of altitude above the earth's surface rather than in terms of distance from the earth's center.
16	The value of RO is transferred to the subroutines FCT and OUTP as X.
17	The value of PRMT(1) = XO is transferred to subroutine FCT as Y(2).
18, 19	The reversed ray path starts at the observing station which by choice of the coordinate system lies on the x-axis, so y = Y(1) = O and z = Y(3) = O.
20	PRMT(6) = 0 causes subroutine OUTP to perform a sequence of initialization steps, one of which is to change PRMT(6) to unity so that they are shipped over on subsequent calls.
21	DERY(1) serves the same purpose for the subroutine FCT that PRMT(6) does for OUTP. (See comment just above.) A large negative value is used for initialization because later on, DERY(1), is the value of dy/dx along the ray path and this is unlikely to become large and negative.
22-24	See 6-8 above.
25	At this point the program takes up initialization procedure in subroutine FCT, lines 3 to 66, as described below.
26	Now we carry out initialization in subroutine OUTP, lines 2 to 38, as described below.
27	Subroutine DHPCG is called to carry out the first step of tracing the path of the reversed ray. It calls on subroutine FCT to calculate the local values of the space derivatives of the path, and hands the coordinates of the new point on the path to subroutine OUTP which processes them and then returns control to DHPCG. This cycle, DHPCG to FCT to DHPCG to OUTP to DHPCG, is repeated until the end value of x, PRMT(2), as specified on input, is reached. Then control returns to the MAIN program where, in the version listed in Fig. 6, a new set of input parameters is fixed and the entire program is repeated, until the DO loops of the MAIN program are completed.
FCT	
7	Checks whether this is the initial call. If not, the initialization procedure in lines 7A to 66 is skipped.
8-20	On the run shown, data was specified in the program rather than being read in from data cards.

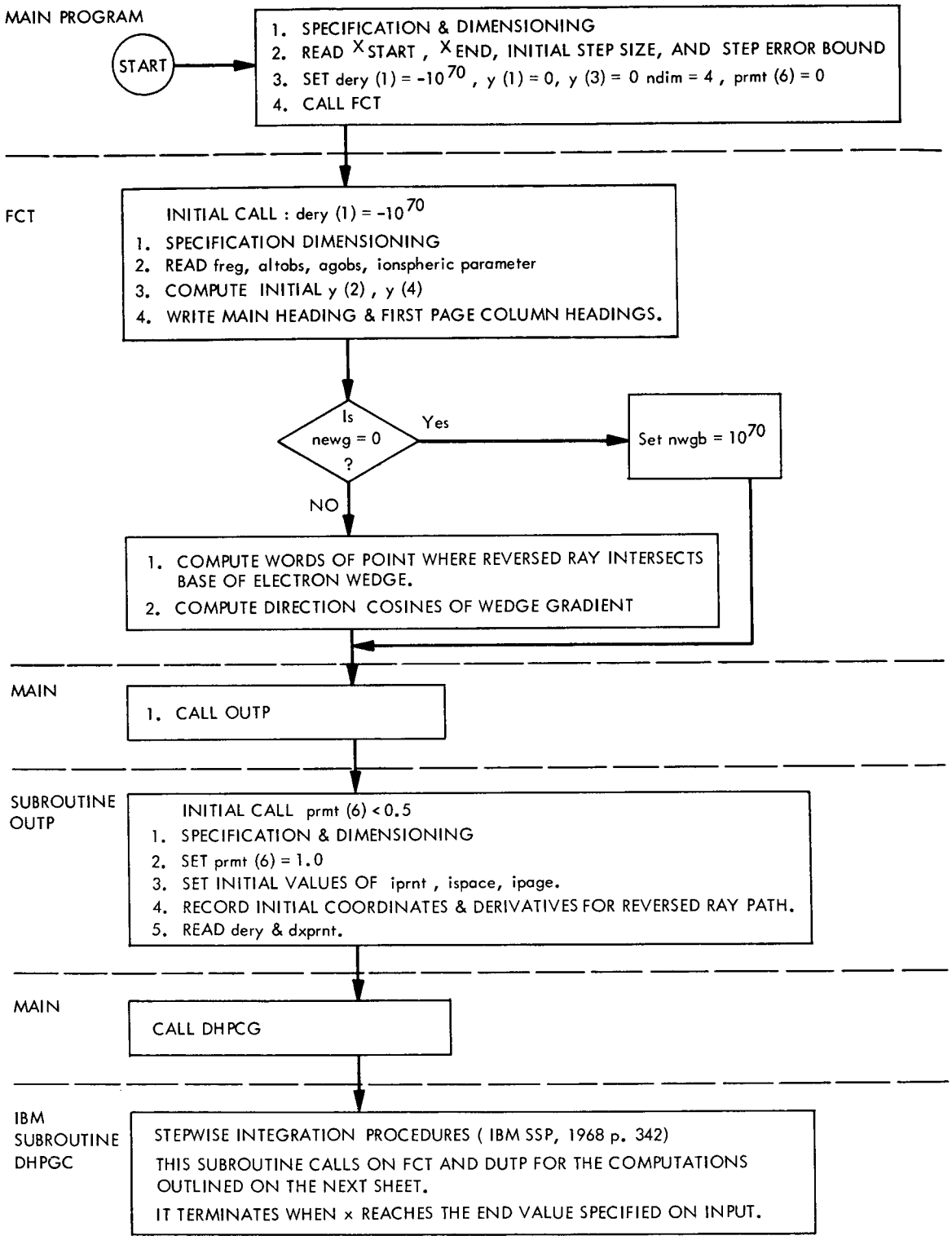
MAIN PROGRAM
START
1. SPECIFICATION & DIMENSIONING
2. READ XSTART , XEND, INITIAL STEP SIZE, AND STEP ERROR BOUND
3. SET dery (1) = -10^70 , y (1) = 0, y (3) = 0 ndim = 4 , prmt (6) = 0
4. CALL FCT
FCT
INITIAL CALL : dery (1) = -10^70
1. SPECIFICATION DIMENSIONING
2. READ freg, altobs, agobs, ionspheric parameter
3. COMPUTE INITIAL y (2) , y (4)
4. WRITE MAIN HEADING & FIRST PAGE COLUMN HEADINGS.
Is newg = 0 ?
Yes
Set nwgb = 10^70
NO
1. COMPUTE WORDS OF POINT WHERE REVERSED RAY INTERSECTS BASE OF ELECTRON WEDGE.
2. COMPUTE DIRECTION COSINES OF WEDGE GRADIENT
MAIN
1. CALL OUTP
SUBROUTINE OUTP
INITIAL CALL prmt (6) < 0.5
1. SPECIFICATION & DIMENSIONING
2. SET prmt (6) = 1.0
3. SET INITIAL VALUES OF iprnt , ispace, ipage.
4. RECORD INITIAL COORDINATES & DERIVATIVES FOR REVERSED RAY PATH.
5. READ dery & dxprnt.
MAIN
CALL DHPCG
IBM SUBROUTINE DHPGC
STEPWISE INTEGRATION PROCEDURES (IBM SSP, 1968 p. 342)
THIS SUBROUTINE CALLS ON FCT AND DUTP FOR THE COMPUTATIONS OUTLINED ON THE NEXT SHEET.
IT TERMINATES WHEN x REACHES THE END VALUE SPECIFIED ON INPUT.

Figure 5(a)

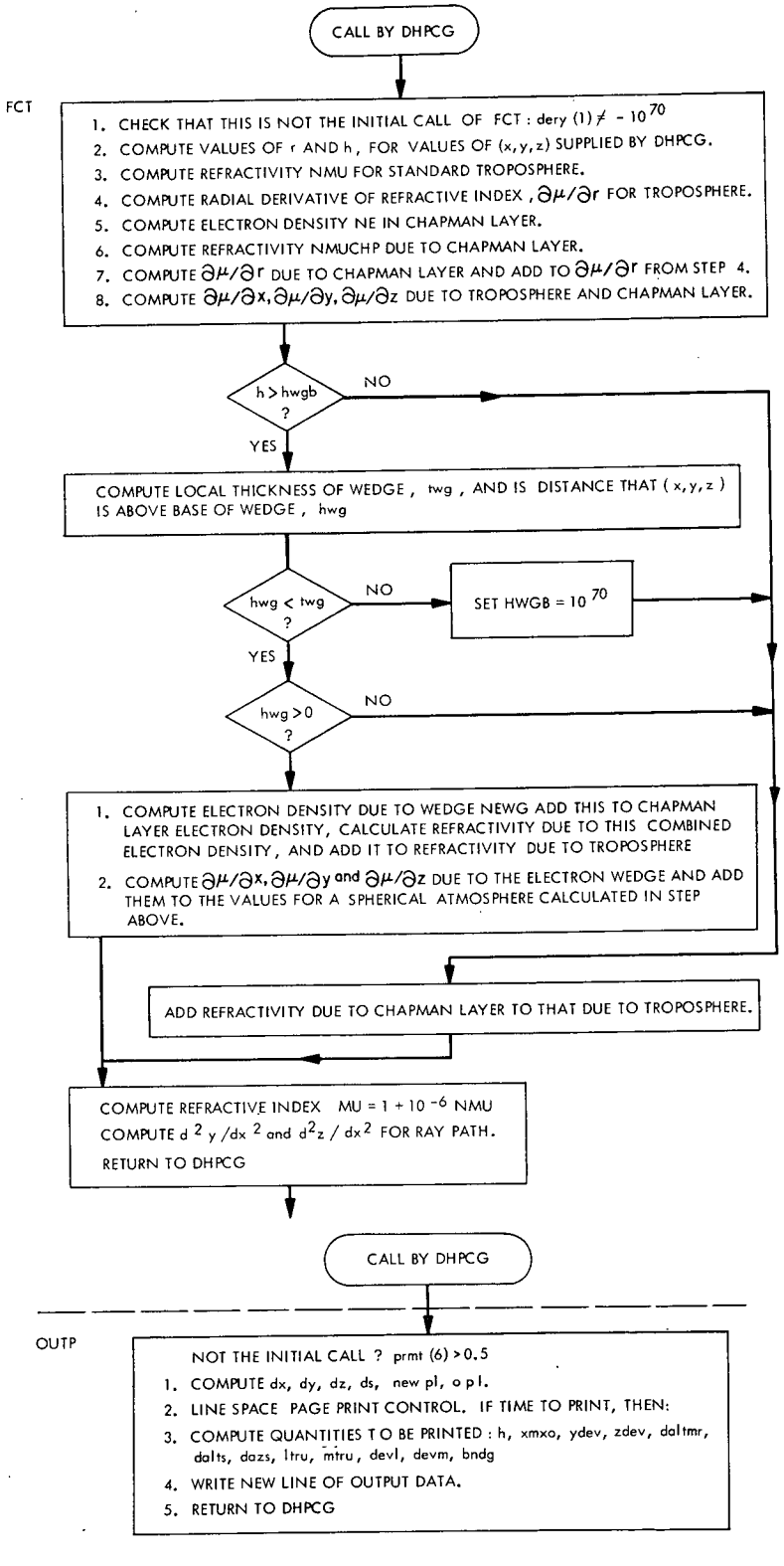

Figure 5(b) and (c)

```
LEVEL 16 ( 1 JULY 69)          OS/360 FORTRAN H

        COMPILER OPTIONS - NAME= MAIN,OPT=00,LINECNT=58,SOURCE,EBCDIC,NOLIST,NODECK
ISN 0002            IMPLICIT REAL*8 (A-H, L-Z)
ISN 0003            INTEGER NDIM / 4 /
ISN 0004            DIMENSION PRMT(6), Y(4), DERY(4), AUX(16,4)
ISN 0005            EXTERNAL FCT, OUTP
      5A    C 10    FORMAT ( 4F10.0 / D8.2 )
      5B    C       READ (5,10) RO, (PRMT(J),J=1,4)
ISN 0006            DO 99 JHWGB = 1, 2
ISN 0007            DO 99 JAZWG = 1,3
ISN 0008            DO 99 JSLOPE = 1,2
ISN 0009            RO = 6.37E+6
ISN 0010            PRMT(1) = 0.
ISN 0011            PRMT(2) = 1000.
ISN 0012            PRMT(3) = 1.
ISN 0013            PRMT(4) = 1.D-06
ISN 0014            PRMT(1) = PRMT(1) + RO
ISN 0015            PRMT(2) = PRMT(2) + RO
ISN 0016            X = RO
ISN 0017            Y(2) = PRMT(1)
ISN 0018            Y(1) = 0.
ISN 0019            Y(3) = 0.
ISN 0020            PRMT(6) = 0.
ISN 0021            DERY(1) = -1.D70
ISN 0022            DERY(2) = 136. / JFREQ
ISN 0023            DERY(3) = 250. + 100. * (JHWGB - 1)
ISN 0024            DERY(4) = 0. + 45. * (JAZWG - 1)
ISN 0025            CALL FCT(X, Y, DERY)
ISN 0026            CALL OUTP (X, Y, DERY, IHLF, NDIM, PRMT)
ISN 0027            CALL DHPCG (PRMT, Y, DERY, NDIM, IHLF, FCT, OUTP, AUX)
ISN 0028         99 CONTINUE
ISN 0029            STOP
ISN 0030            END
ISN 0002            SUBROUTINE FCT (X, Y, DERY)
ISN 0003            IMPLICIT REAL*8 (A-H, L-Z)
ISN 0004            DIMENSION Y(4), DERY(4), PRMT(6)
ISN 0005         10 FORMAT ( F10.0/ 2F10.0 / 4F10.0 / 5E10.0 )
ISN 0006         30 FORMAT ('1', T5, 'THE POSITION OF A RADIC SOURCE OF FREQ =',
                    2 F5.1, ' MHZ; OBSERVED ELEVATION =',F4.0, ' DEG; OBS AZIMUTH',
                    3 ' =', F4.0, ' DEG, NORTH TOWARD EAST.' / T8, 'OTHER ',
                    4 'PARAMETERS ARE, IN KM: EARTH RADIUS =', F6.0, '; HCHP =',
                    5 F5.0, '; HEMAX =', F5.0, '; HT & THK OF ELECTRON WEDGE =',
                    6 F5.0, F5.0 / T8, 'TAN OF WEDGE ANGLE =', F4.2, '; AZIMUTH',
                    7 ' OF WEDGE GRADIENT =', F4.0, ' DEG; SECSUN =', F4.0, ';' /
                    8 T8, 'MAX ELECTRON DENSITY, IN CHAPMAN LAYER, =', F5.0,
                    9 ', IN WEDGE, =', F5.0, ', BOTH IN 10**10/M**3' / T70,
                    1 'H. W. MORGAN, GSEC CODE 544, AUGUST, 1969.' )
ISN 0007            IF (DERY(1) .NE. -1.D70 )  GO TO 70
      8A    C       READ (5,10) FREQ, ALTOBS, AZOBS, SECSUN, HCHP, HEMAX,
      8B    C     2NEMAX,     NEWGMX, HWGB, TWGO, SLOPWG, AZWG
ISN 0009            FREQ = DERY(2)
ISN 0010            ALTOBS = 50.
ISN 0011            AZOBS = 80.
ISN 0012            SECSUN = 1.
ISN 0013            HCHP = 100.
ISN 0014            HEMAX = 300.
ISN 0015            NEMAX = 200.
ISN 0016            NEWGMX = 100.
ISN 0017            HWGB = DERY(3)
ISN 0018            TWGO = 10.
ISN 0019            SLOPWG = .1
ISN 0020            AZWG = DERY(4)
ISN 0021            RO = X
ISN 0022            XO = Y(2)
ISN 0023            IF (NEWGMX .NE. 0. )  GO TO 20
ISN 0026            HWGB = 1.D12
ISN 0025            TWGO = 1.D12
ISN 0027            SLOPWG = 1.D12
ISN 0028            AZWG = 1.D12
```


Figure 6 (Page 1 of 5)

```
LEVEL 16 ( 1 JULY 68)                    OS/360 - FORTRAN H

          COMPILER OPTIONS - NAME= MAIN,OPT=00,LINECNT=58,SOURCE,EBCDIC,NOLIST,NODECK

ISN 0029          20  CONTINUE
ISN 0030              WRITE (6,30) FREQ, ALTOBS, AZOBS, RO, HCHP, HEMAX, HWGB,
                     1TWGO, SLOPWG, AZWG, SECSUN, NEMAX, NEWGMX
ISN 0031              DGTORD = .01745329251 9943
ISN 0032              ALTOBS = DGTORD * ALTOBS
ISN 0033              AZOBS = DGTORD * AZOBS
ISN 0034              Y(2) = ALTOBS
ISN 0035              Y(3) = AZOBS
ISN 0036              Y(4) = DSIN( ALTOBS )
ISN 0037              COTALT = DCOTAN( ALTOBS )
ISN 0038              SINAZO = DSIN( AZOBS )
ISN 0039              COSAZO = DCOS( AZOBS )
ISN 0040              Y(2) = COTALT * SINAZO
ISN 0041              Y(4) = COTALT * COSAZO
ISN 0042              IF ( NEWGMX .EQ. 2 ) RETURN
ISN 0044              L = LSQRY(4)
ISN 0045              LSQ = L * L
ISN 0046              XWGB = (1.-LSQ)*XO + L*DSQRT((RO+HWGB)*(RO+HWGB)-(1.-LSQ)*XO*XO)
ISN 0047              YWGB = Y(2) * ( XWGB - XO )
ISN 0048              ZWGB = Y(4) * ( XWGB - XO )
ISN 0049              RWGBSQ = ( XWGB*XWGB + YWGB* YWGB + ZWGB* ZWGB )
ISN 0050              RWGB = DSQRT( RWGBSQ )
ISN 0051              IF ( DABS(XWGB) .LT. RWGB ) GO TO 50
ISN 0053              COSTHT = 1.
ISN 0054              SINTHT = 0.
ISN 0055              GO TO 60
ISN 0056          50  CONTINUE
ISN 0057              COSTHT = XWGB / RWGB
ISN 0058              SINTHT = DSQRT( 1. - COSTHT * COSTHT )
ISN 0059          60  CONTINUE
ISN 0060              AZWG = DGTORD * AZWG
ISN 0061              SINAZW = DSIN( AZWG )
ISN 0062              COSAZW = DCOS( AZWG )
ISN 0063              AWG = - COSAZW * SINTHT
ISN 0064              BWG =  SINAZW * COSAZO  +  COSAZW * COSTHT * SINAZO
ISN 0065              CWG = -SINAZW * SINAZO  +  COSAZW * COSTHT * COSAZO
ISN 0066              RETURN
ISN 0067          70  CONTINUE
ISN 0068              R = DSQRT( X*X + Y(1)*Y(1) + Y(3)*Y(3) )
ISN 0069              H = R - RO
ISN 0070              NMU = 313. * DEXP( -.1439 * H )
ISN 0071              MUR = 1.D-06 * ( -.1439 ) * NMU
ISN 0072              ZCHP = ( H - HEMAX ) / HCHP
ISN 0073              CHPTRM = SECSUN * DEXP( -ZCHP )
ISN 0074              NE = NEMAX * DEXP( 0.5 * ( 1. - ZCHP - CHPTRM ) )
ISN 0075              NMUCHP = -4.03005 * NE / (FREQ * FREQ )
ISN 0076              MUR = 1.D-06*NMUCHP* 0.5 * ( -1. + CHPTRM ) / HCHP  + MUR
ISN 0077              MUX = ( X / R ) * MUR
ISN 0078              MUY = ( Y(1) / R ) * MUR
ISN 0079              MUZ = ( Y(3) / R ) * MUR
ISN 0080              IF (H .LE. HWGB) GO TO 90
ISN 0082              DXWG = X - XWGB
ISN 0083              DYWG = Y(1) - YWGB
ISN 0084              DZWG = Y(3) - ZWGB
ISN 0085              SWG = DXWG * AWG +  DYWG * BWG +  DZWG * CWG
ISN 0086              TWG = TWGO + SLOPWG * SWG
ISN 0087              HWG = ( DXWG * XWGB +  DYWG * YWGB  +  DZWG * ZWGB  ) / RWGB
      87A     C       CALL HERE(12150)
ISN 0088              IF ( HWG .LT. TWG )  GO TO 80
ISN 0090              HWGB = 1.070
ISN 0091              GO TO 90
ISN 0092          80  CONTINUE
```


Figure 6 (Page 2 of 5)

```
ISN 0093              IF ( HWG .LE. 0. )  GO TO 90
ISN 0095              QWG = 2. * ( HWG / TWG ) - 1.
ISN 0096              WGP1 = 1. - QWG * QWG
ISN 0097              WGP2 = 1. - 1. / WGP1
ISN 0098              NEWG = NEWGMX * DEXP ( WGP2 )
ISN 0099              A1 = 4. * NEWG * QWG / (WGP1 * WGP1 * TWG )
ISN 0100              A = -.403 * A1 / (FREQ * FREQ )
ISN 0101              B = HWG * SLOPWG / TWG
ISN 0102              MUXWG = A * ( B * AWG - XWGB / RWGB )
ISN 0103              MUYWG = A * ( B * BWG - YWGB / RWGB )
ISN 0104              MUZWG = A * ( B * CWG - ZWGB / RWGB )
     104A     C       CALL HERE(13250)
ISN 0105              NE = NE + NEWG
ISN 0106              MUX = MUX + MUXWG
ISN 0107              MUY = MUY + MUYWG
ISN 0108              MUZ = MUZ + MUZWG
ISN 0109              NMU = -4.03005 * NE / (FREQ * FREQ )  + NMU
ISN 0110              GO TO 95
ISN 0111           90 CONTINUE
ISN 0112              NMU = NMUCHP + NMU
ISN 0113           95 CONTINUE
ISN 0114              MU = 1. + 1.D-06 * NMU
                   C625 WRITE (6,630) NMU, X
ISN 0115           630 FORMAT ( ' ',T5,'REFRACTIVITY = ', F12.2,' AT X =',F8.2)
ISN 0116              G = 1. + Y(2) * Y(2)  +  Y(4) * Y(4)
ISN 0117              MUOVG = MU / G
ISN 0118              Y2SQ = Y(2) * Y(2)
ISN 0119              Y4SQ = Y(4) * Y(4)
ISN 0120              A = MU
ISN 0121              B = MUOVG * Y2SQ
ISN 0122              C = MUOVG * Y4SQ
ISN 0123              D = MUOVG * Y(2) * Y(4)
ISN 0124              E = MUY * G
ISN 0125              F = MUZ * G
ISN 0126              H = MUX + MUY * Y(2) + MUZ * Y(4)
ISN 0127              DY2NUM = (A - C) * (E - H * Y(2)) + D*(F - H * Y(4) )
ISN 0128              DY4NUM = (A - B) * (F - H * Y(4) )  + D * (E - H * Y(2) )
ISN 0129              DENOM = (A - B) * (A - C)  -  D * D
                   C665 WRITE (6,670) DENOM
ISN 0130           670 FORMAT( ' ', T5, 'DENOM AT LINE 15300 =', G20.6 )
ISN 0131              DERY(1) = Y(2)
ISN 0132              DERY(2) = DY2NUM / DENOM
ISN 0133              DERY(3) = Y(4)
ISN 0134              DERY(4) = DY4NUM / DENOM
ISN 0135              RETURN
ISN 0136              END
```

```
LEVEL 16 (1 JULY 68)                    OS/360 FORTRAN H

          COMPILER OPTIONS - NAME= MAIN,OPT=00,LINECNT=58,SOURCE,EBCDIC,NOLIST,NODECK,
    ISN 0002              SUBROUTINE OUTP(X,Y,DERY,IHLF,NDIM,PRMT)
    ISN 0003              IMPLICIT REAL*8 (A-H, L-Z)
    ISN 0004              INTEGER NDIM
    ISN 0005              DIMENSION Y(4), DERY(4), PRMT(6)
    ISN 0006           10 FORMAT ( 4F10.0 / F10.0 )
    ISN 0007           20 FORMAT ('1', T90, 'PAGE ', I3)
    ISN 0008           30 FORMAT ('0', T3, ' ALTITUDE     XMO       Y-YNOM     Z-ZNOM  ',
                          2' ELEVATION      AZIMUTH  *  -  -  -  DIRECTION COSINES  ',
                          3'-  -  -  *     TOTAL  ' / T3, ' OF SOURCE   (VERTICAL) (EAST)',
                          4' (NORTH)    OBSV-TRUE     OBS-TRUE       (L: FROM EAST; M: FROM',
                          5' NORTH)         BENDING'    / T6, ' KM          OF OBS''G ',
                          6'STATION, IN KM  MRAD      SEC       SEC      L(TRUE)   M(TRUE)',
                          7'      L-LOBS       M-MOBS        SEC      IHLF'  )
    ISN 0009           40 FORMAT (' ', F9.3, F10.3, 2F9.3, F7.2,  F8.2, F8.1,
                          2 T11.6, F10.6, D12.3, D11.3, F8.1, I5  )
    ISN 0010           50 FORMAT ( ' ' )
    ISN 0011              IF (PRMT(6) .GT. 0.5) GO TO 70
    ISN 0013              PRMT(6) = 1.
    ISN 0014              RO = X
    ISN 0015              XO = PRMT(1)
```

Figure 6 (Page 3 of 5)

```
ISN 0016              XOLD = PRMT(1)
ISN 0017              YOLD = Y(1)
ISN 0018              ZOLD = Y(3)
ISN 0019              DYDX0 = Y(2)
ISN 0020              DZDX0 = Y(4)
ISN 0021              ALTOBS = DERY(2)
ISN 0022              AZOBS = DERY(3)
ISN 0023              LOBS = DERY(4) * Y(2)
ISN 0024              MOBS = DERY(4) * Y(4)
                C     READ (5,10) DERY, DXPRNT
ISN 0025              DERY(1) = .45
ISN 0026              DERY(2) = .05
ISN 0027              DERY(3) = .45
ISN 0028              DERY(4) = .05
ISN 0029              DXPRNT = 10.
ISN 0030              H = X0 - R0
ISN 0031              XMX0 = 0.
ISN 0032              WRITE (6, 30)
ISN 0033              WRITE (6, 40)  H, XMX0
ISN 0034              IPRNT = 1
ISN 0035              ISPACE = 1
ISN 0036              IPAGE = 1
ISN 0037              PRNTFX = PRMT(3) / 1.D4
ISN 0038              RETURN
ISN 0039        70    CONTINUE
ISN 0040              DX = X - XOLD
ISN 0041              IF ( DX .EQ. 0. )  RETURN
ISN 0043              DY = Y(1) - YOLD
ISN 0044              DZ = Y(3) - ZOLD
ISN 0045              DS = DSQRT(DX*DX + DY*DY + DZ*DZ )
ISN 0046              XOLD = X
ISN 0047              YOLD = Y(1)
ISN 0048              ZOLD = Y(3)
ISN 0049              XMXC = X - XC
ISN 0050              IF ( XMX0 + PRNTFX .LT. IPRNT * DXPRNT )  RETURN
ISN 0052              IPRNT = IPRNT + 1
ISN 0053              IF ( IPRNT-2 .NE. 5*ISPACE )  GO TO 80
ISN 0055              WRITE (6, 50)
ISN 0056              ISPACE = ISPACE + 1
ISN 0057        80    CONTINUE
ISN 0058              IF (IPRNT .LT. 30*IPAGE) GO TO 90
ISN 0060              IPAGE = IPAGE + 1
ISN 0061              WRITE (6,20) IPAGE
ISN 0062              WRITE (6,30)
ISN 0063        90    CONTINUE
ISN 0064              R = DSQRT( X*X + Y(1)*Y(1) + Y(3)*Y(3) )
ISN 0065              H = R - R0
ISN 0066              YNOM = DYDX0 * XMX0
ISN 0067              ZNOM = DZDX0 * XMX0
ISN 0068              YDEV = Y(1) - YNOM
ISN 0069              ZDEV = Y(3) - ZNOM
ISN 0070              RANGSQ = XMXC*XMX0 + Y(1)*Y(1) + Y(3)*Y(3)
ISN 0071              RANGE = DSQRT( RANGSQ )
ISN 0072              IF ( DABS(XMX0) .LT. RANGE )  GO TO 110
ISN 0074              ALTS = 1.5707963267948 97
ISN 0075              AZS = -1.D12
ISN 0076              GO TO 120
ISN 0077       110    CONTINUE
ISN 0078              ALTS = DARSIN( XMX0 / RANGE )
ISN 0079              RPOLS = RANGE * DCOS( ALTS )
ISN 0080              IF ( DABS(Y(1)) .LT. RPOLS )  GO TO 115
ISN 0082              AZS = 1.5707963267948 97
ISN 0083              GO TO 120
ISN 0084       115    CONTINUE
ISN 0085              AZS = DARSIN( Y(1) / RPOLS )
ISN 0086       120    CONTINUE
ISN 0087              DEVALT = ALTOBS - ALTS
ISN 0088              DEVAZ = AZOBS - AZS
ISN 0089              DALTMR = 1000. * DEVALT
ISN 0090              DALTS = 206264.80625 * DEVALT
ISN 0091              DAZS = 206264.80625 * DEVAZ
```


Figure 6 (Page 4 of 5)

```
ISN 0092              LTRU = Y(1) / RANGE
ISN 0093              MTRU = Y(3) / RANGE
ISN 0094              DEVL = LTRU - LOBS
ISN 0095              DEVM = MTRU - MOBS
ISN 0096              NOBS = DSQRT( 1. - LOBS * LOBS - MOBS * MOBS )
ISN 0097              LPATH = DY / DS
ISN 0098              MPATH = DZ / DS
ISN 0099              NPATH = DX / DS
ISN 0100              COSBDG = LPATH * LOBS + MPATH * MOBS + NPATH * NOBS
ISN 0101              IF( DABS(COSBDG) .LT. 1. ) GO TO 130
ISN 0103              BNDG = 0.
ISN 0104              GO TO 140
ISN 0105        130   CONTINUE
ISN 0106              BNDG = DARCOS( COSBDG )
ISN 0107        140   CONTINUE
ISN 0108              BNDG = 2C9264.E0625 * BNDG
ISN 0109              WRITE (6,40) H, XMXO, YDEV, ZDEV, DALTMR, DALTS,
                     2DAZS, LTRU, MTRU, LEVL, DEVM, BNDG, IHLF
ISN 0110              RETURN
                      END
ISN 0002              SUBROUTINE HERE(I)
ISN 0003              WRITE (6,1) I
ISN 0004            1 FORMAT(' ', T5, '* * * HERE I AM AT LINE', I7 )
ISN 0005              RETURN
ISN 0006              END
```

Figure 6 (Page 5 of 5)

ISN (FCT)	Comment
21	The value of RO ane XO are transferred from MAIN to FCT as X and Y(z), respectively.
23-29 b	If there is no wedge of electron density (MEWGMX = O), then HWGB is set to a large positive value. This causes the program at line 80 below to skip the electron wedge calculations and go directly to line 111. TWGO, SLOPWG, and AZWG are also given large values so that asterisks will be printed for the values of these quantities in the output data heading.
30	Write main heading for output data.
31	Set numerical multiples for converting angles from degrees to radians.
32-35	Convert ALTOBS and AZOBS from degrees to radians and store in DERY(2) and DERY(3) for transfer to OUTP.
36	S e (ALTOBS) in DERY(4) for transfer to OUTP.
37-39	. SINAZO, and COSAZO.
40-41	Co - SINAXO and COTALT - COSAXO and store in Y(2) and Y(4) for transfer to OUTP.
42	If there is no electron wedge the initialization of FCT is complete and the program returns to MAIN.
44-50	Compute the radius vector of the point where the projection of the reversed ray intersects the base of the electron wedge. (See Appendix D).

ISN (FCT)	Comment
51-55	If the value held by the computer for RWGB is less than XWGB, then to avoid an error signal at 58, the values of COSTHT and SINTHT are set rather than computed. (NOTE: LT. in 51 should be LE.)
56-58	Computation of COSTHT and SINTHT .
59-62	Convert AZWG from degrees to radians and compute SINAZW and COSAZW.
63-65	Compute AWG, BWG, CWG. (See Appendix E.)
66	Return to MAIN; initialization of FCT is completed.
67-69	Use output from DHPCG to compute altitude, H, of current point on ray path.
70	Compute tropospheric radio refractivity. (Reference: Bean, B.R., and Dutton, E. J., Radio Meteorology (NBS Monograph 92) GPO 1966, pp. 65-67).
71	Compute gradient of tropospheric refractive index.
72-74	Compute electron density, NE, of Chapman layer. (Reference: Davies, K., Ionospheric Radio Propagation (NBS Monograph 80) GPO, 1965, page 17.)
75	Compute refractive index due to Chapman layer.
76-79	Compute gradient of the refractivity due to the Chapman layer and the troposphere, superimposed.
80	If the ray path has not yet reached the altitude of the base of the electron wedge, then skip to 111.
82-87	Compute the height of the current point relative to the base plane of the wedge (HWG) and the local thickness of the wedge (TWG)
87A	Call for a print-out, used in debugging the program.
88-90	If HWG is equal to or greater than TWG, then we are through the wedge. In that case, we set HWGB at a large value so on subsequent calls the IF statement at 80 will cause all computations involving the wedge to be skipped over, and proceed to 111.
93	If HWG is less than zero, the reversed ray has not yet entered the electron wedge, and we skip to 111. (It is possible, though not likely, for HWG to be less than zero even though H is greater than HWGB because the base of the wedge is taken as plane so that its altitude above the earth's surface is not constant. HWGB is its minimum altitutde. See Fig. D-1).

ISN (FCT)	Comment
95-104	Compute the electron density, NEWG, and the components of the gradient of the refractive index due to the electron wedge at the current point.
104A	Statements used in debugging the program, to produce a line of print-out at this point each time subroutine FCT is called by DHPCG.
105-108	The total electron density and the gradient of the refractive index at the current point are the respective sums of the values due to the Chapman layer (computed at 74 and 77-79) and those due to the electron wedge.
109-110	The local refractivity is the sum of that due to the total electron density and that associated with the troposphere (line 70).
111-112	If electron wedge calculations have been skipped over, then the local refractivity is just the sum of that due to the Chapman layer and that due to the troposphere (line 70).
113-114	In any case, the refractive index follows from the refractivity, by definition of the latter.
114A-115	Statements used for debugging to produce a line of print-out at this point each time subroutine FCT was called by DHPCG.
116-135	Computation of DERY for return to the calling subroutine, DHPCG. The formulas used are derived in Appendix B of Reference (1) cited in the Introduction (Goddard Space Flight Center, X-520-69-30). For convenience, that Appendix is reproduced as Appendix B of the present paper. Note However that the independent variable used in ERFRAC is x, not z, so that in the formulas of Appendix B, z must be changed to x, x to y, and y to z.
OUTP	
6-10	Format statements; will be mentioned where the read and write statements appear below.
11,13	If this is not the initial call of OUTP, the initialization proceudre, lines 14-38, is skipped over.
14-22	Values of variables are set.
23-24	LOBS and MOBS are computed; see App. F.
24A-29	On the run listed, the values for DERY and for DXPRNT are specified in the source deck rather than read in from data cards. The appropriateness of the values used here for DERY, the error weights used by DHPCG, is uncertain and should be checked. The value of DXPRNT was chosen so as to obtain at least one output data point in the electron wedge, whose thickness was set at 10 km.
30, 31	Initial values of H and XMXO are computed for first line of print-out.
32, 33	Print column headings and initial line of data.

INS (OUTP)	Comment
34-36	Set the three print control indexes to unity.
37	Set PRNTFX at a positive value which is less than the smallest step size that may be used in DHPCG, namely $PRMT(3)/2^{10}$.
38	Return from OUTP to MAIN program following initialization of OUTP.
39	On each call subsequent to the first, execution begins here (Fortran label 70).
40	Compute change in X, since the last call, DX.
41	Return to DHPCG if DX is zero. If DHPCG, when it is first call, merely hands the initial values of the coordinates of OUTP, then OUTP returns to DHPCG for the first step of integration.
43-45	Computes the increment of path length, DS, for the current step of integration. (This is not utilized in the present run, but could be accumulated and printed-out if desired. Also, if in subroutine FCT, the current value of the refractive index MU were stored in COMMON, this could be accessed by OUTP to multiply DS, giving the increment in optical path length.
46-48	Store current values of coordinates of point on ray path.
49	Compute XMXO
50	Return to DHPCG if it is not time for a line of print-out.
52	Increase line print control index by one.
53-57	Print a blank line after every fifth line of output.
58-63	Provides pagination, with column headings on each page. Note: In order to obtain an integral number of groups of five lines each on a page, "IPRNT" in line 58 should be replaced by "IPRNT-2."
64-65	Compute R and H for current point.
66-69	Compute displacement of current point from point at same value of x on a straight line projection of the ray as observed at the observing station.
70-71	Compute RANGE, the distance from observing station to current point.
72-77	If the value held in storage for XMXO is equal to or greater than that for RANGE, then the true elevation angle of the current point is directly set to 90°, thus avoiding the generation of an error signal in an attempt to calculate it, at 85. Also AZS is set to a value which will cause asterisks to be printed for azimuth error in the print-out data.
78-79	Compute the true elevation angle of the current point, and its distance from the X-axis, RPOLS.

INS (OUTP)	Comment
80-84	If the computer's value of y is less than its value of RPOLS, then we avoid an error signal by setting the azimuth of the current point to 90° without trying to compute it.
85	Compute the azimuth angle of the current point.
87-91	Compute the difference between the observed and actual elevation angle of the current point in radians, DEVALT, milliradians, DALTMR, and seconds of arc, DALTS; and the difference between the observed and actual azimuth in radians, DEVAZ, and seconds of arc, DAZS.
92-95	Compute the true direction cosines for the current point and their differences from those of the ray direction as observed at the observing station.
96-108	Compute the angle between the tangent to the ray path at the current point and the direction of the ray as observed at the observing station, in seconds of arc.
109-110	Write a line of output data and return to DHPCG.

7. RESULTS

Successful complete runs of ERFRAC, tracing a radio-ray up and through electron wedges, were achieved on November 10, 1969. Figures 7 through 11 show results obtained on a run for which the parameters were as follows. (See list of symbols in Appendix A for definitions.)

Radio frequency, FREQ = 136 MHz.

Observed Elevation angle of ray, ALTOBS = 50 degrees

Observed azimuth of ray, AZOBS = North 80 degrees East

Chapman Layer Parameters:
- Maximum electron density, NEMAX = 2×10^{12} n^{-3}
- Height of maximum density, HEMAX = 300 km.
- Scale Height of Chapman layer, HCMP = 100 km
- Secant of sun's zenith angle, SECSUN = 1.0

Electron Wedge Parameters:
- Height of base of wedge, HWGB = 250 km
- Thickness of wedge where ray enters, TWGO = 10 km
- Tangent of vertex angle of wedge, SLOPWG = 0.1
- Azimuth of wedge gradient, AZWG = 0 degrees
- Maximum electron density, NEWGMX = 1×10^{12} m^{-3}.

Figure 7 shows to an exaggerated scale the way in which the radio ray is caused to curve by the varying refractive index of the atmosphere. As indicated, the graph shows only the eastward component of the horizontal displacement of the ray from a straight line projection, but this is nearly the total horizontal displacement since the observed azimuth angle of the ray was set to 80°, so the northward component is small (less than 1/5 of the eastward component, according to the print-out).

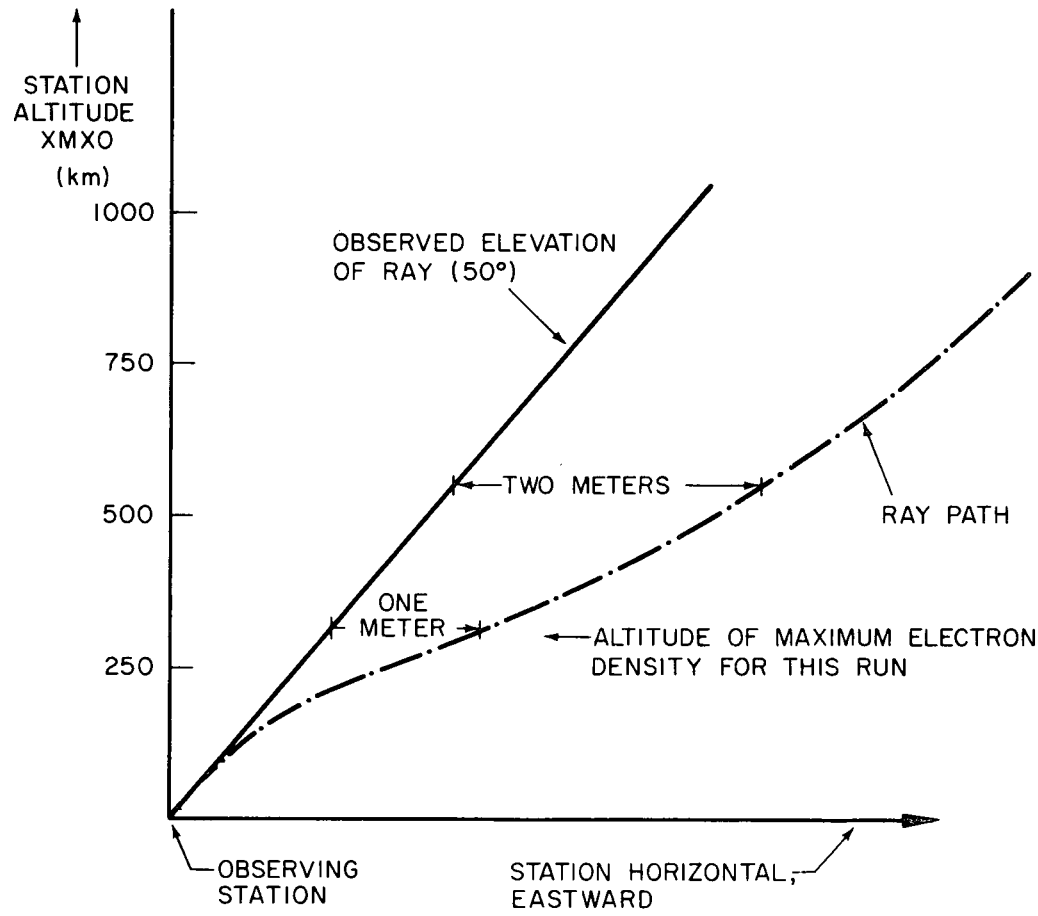

Figure 7. Radio Ray Path, Showing Eastward Component of Horizontal Displacement from Straight Like Projection of the Observed Ray Direction, at the Greatly Exaggerated Scale Indicated.

Figure 8 is another plot of this eastward horizontal displacement, and Fig. 9 shows a magnified portion of Fig. 8, revealing more clearly the effect on the ray path of the assumed electron wedge at 250 km altitude.

Figure 10 shows the elevation angle error (the difference between the apparent and actual elevation of the radio source) as a function of the altitude of the source. The effect of tropospheric refraction is clearly apparent, producing an angle error of some 40 seconds of arc for a source only 20 km up. On the other hand, the effect of the electron wedge at 250 km altitude is hardly discernible. Its presence shows up in Figure 11, however, where the total or cumulative bending is plotted vs. altitude for a ray which starts downward from an altitude (XMXO) of 400 km. It gradually curves upward as it travels down into the Chapman layer until it reaches the altitude of maximum electron density (300 km) and then it begins curving downward again. The electron wedge causes a sharp bend upward and then a sharp downward bend which is not quite as great so that the cumulative bending below the wedge is more positive than it would have been without the wedge. Consequently, for this wedge orientation (AZWG = 0 degrees), the magnitude of the elevation angle error at the observing station is less than it would have been without the wedge. An orientation with AZWG = 180 degrees presumably would cause maximum angle error. (The angle error with AZWG = zero was 453 seconds of arc; with AZWG = 90°, it was 470 seconds, and with no wedge at all 464 seconds.)

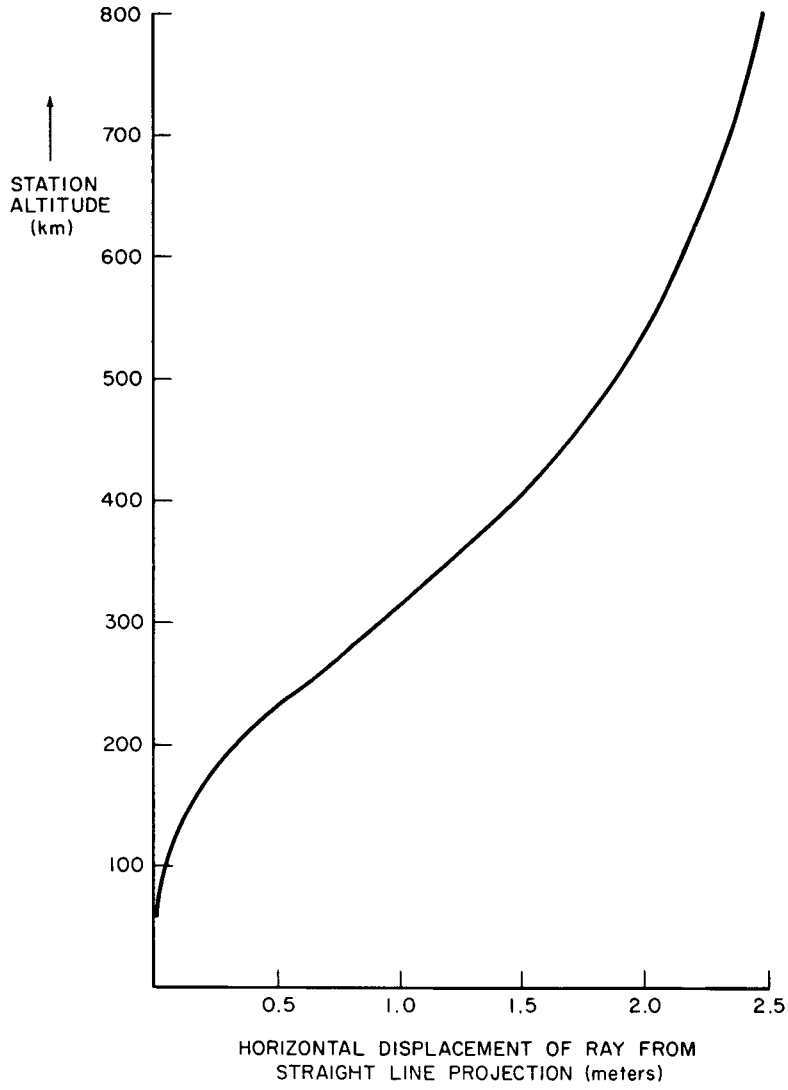

Figure 8. Eastward Displacement of Ray Path from a Straight Line Projection of the Observed Ray Direction

The cumulative bending becomes negative at altitudes below 200 km, indicating that the downward slant of the ray path is steeper than it was when it started at 400 km. (The slant angle which corresponds with this plot is the angle of the ray relative to the observing stations, horizontal rather than local horizontal.)

The integrating subroutine, DHPCG, used the step-size specified on input, PRMT(3) = 1 km throughout the run except at the start and in the electron wedge. At the first print-out point, 2 km altitude, it was using step-size $1/2^3$ = .125 km, and increased this to the nominal 1 km at 44 km altitude. When it encountered the large electron density gradients in the electron wedge, it decreased the step-size, from 1 km at altitude 249 km, to $1/2^5$ = .031 km at 251 km, returning to 1 km step-size at 266 km, which is above the wedge. (DHPCG reduces the step-size if an internally-computed measure of "truncation error" at a single step exceeds an "upper bound" which is specified as PRMT(4) on input.)

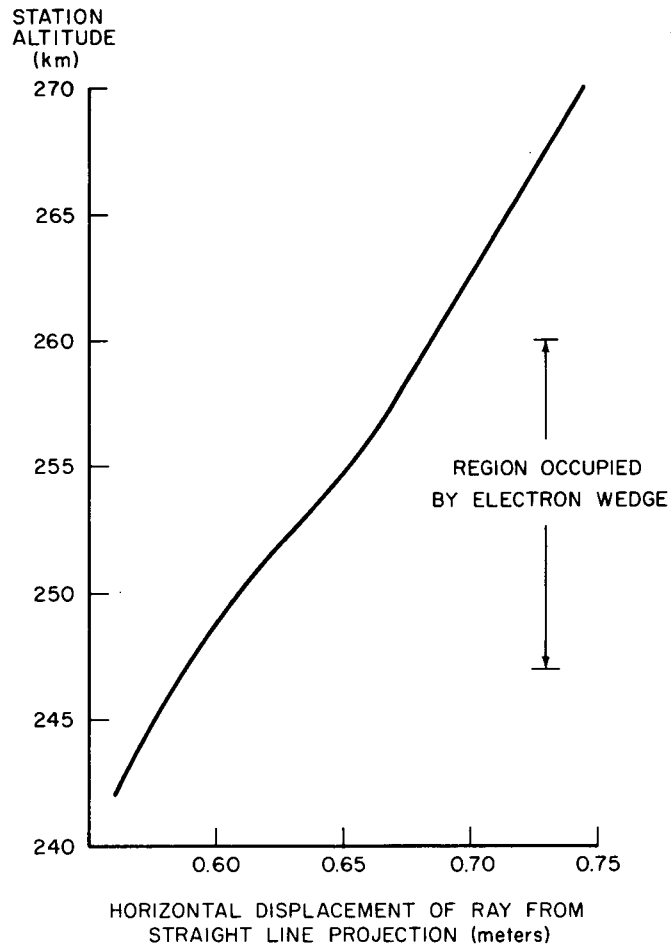

Figure 9. Magnified Portion of Figure 8, Showing Effect of Electron Wedge

Results for the elevation angle error for a variety of circumstances are shown in the table below. The last three columns show that when the angle error ascribable to tropospheric refraction (about 50 arc seconds), is subtracted, the remaining angle error at operating frequency 68 MHz is very nearly just four times that at 136 MHz under all conditions, and is constant at least to slide-rule accuracy, for a given satellite altitude. From this, it appears that if the apparent elevation were observed at both frequencies, the elevation angle error due to the ionosphere could be computed to within one percent which is about 4 arc seconds in the present case, by taking the difference between the two observed elevation angles and dividing by 3.02 or thereabouts, the exact value depending on satellite altitude. The result would then be added to the elevation observed at the lower of the two observed frequencies to get the true elevation.

Of course, careful theoretical analysis is needed before the adoption of such a procedure could be seriously proposed. Such analysis is not attempted in this paper.

For reference, the errors in the direction cosines L and M (these are the cosines of the angles measured from station east and from station north, respectively), which were also computed and printed out, are tabulated below. The values tabulated are 10^5 times the actual error. For example, in the first line, the error in L at 68 MHz is $612 \times 10^{-5} = .00612$, and the error in M at 136 MHz is $29.2 \times 10^{-5} = .000292$.

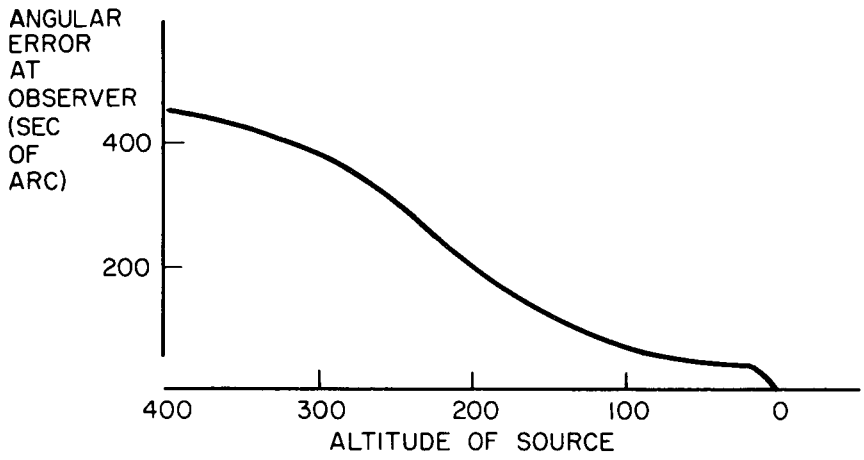

Figure 10. Angular Error at the Observer vs. Altitude (XMXO) of Radio Source.

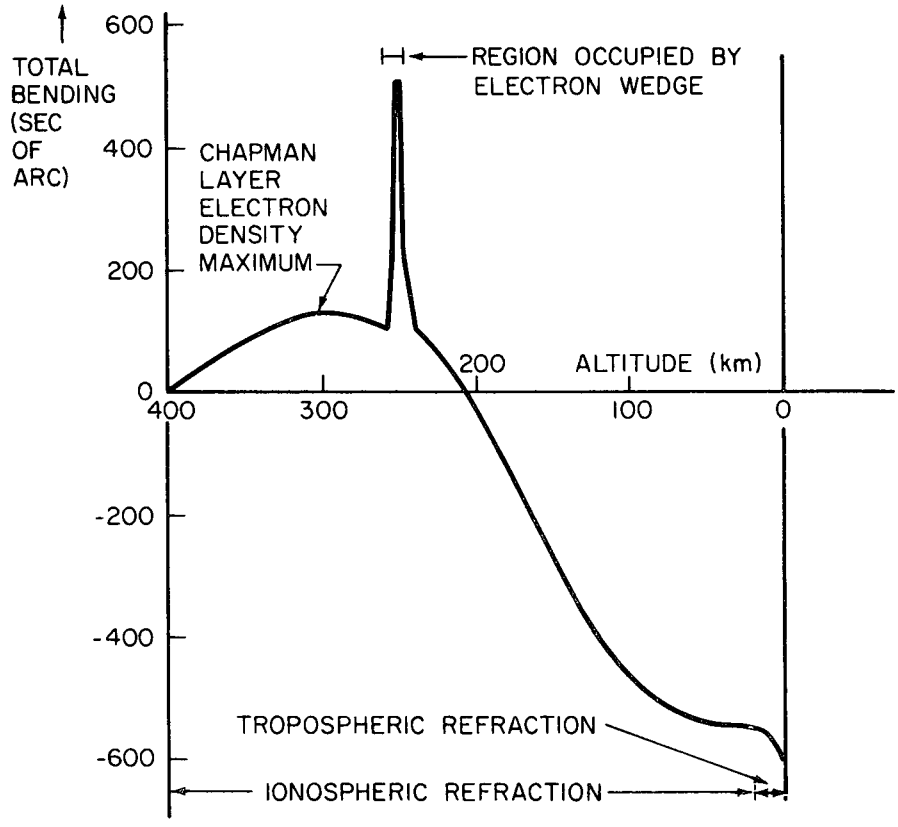

Figure 11. Cumulative Bending of Ray vs. Altitude, for Source at 400 km Altitude.

Satellite Altitude (km)	Azimuth Angle of Electron Wedge	Elevation Angle Error, ϵ (arc sec)		$\epsilon - \epsilon_{TROP}$ (arc seconds)		Ratio of last 2 cols.
		68 MHz	136 MHz	68 MHz	136 MHz	
400	0°	1679	453	1629	403	4.04
	45°	1701	458	1651	408	4.05
	90°	1749	470	1699	420	4.04
600	0°	1633	443	1583	393	4.03
	45°	1667	451	1617	401	4.03
	90°	1744	470	1694	420	4.03
800	0°	1383	382	1333	332	4.01
	45°	1424	392	1374	342	4.02
	90°	1514	414	1464	364	4.02
1000	0°	1166	328	1116	278	4.01
	45°	1211	339	1161	289	4.01
	90°	1310	364	1260	314	4.01

Satellite Altitude (XMXO)	AZOBS	(Error in Direction Cosines) $\times 10^5$			
		Error in L		Error in M	
		68 MHz	136 MHz	68 MHz	136 MHz
400	0°	612	166	108	29.2
	45°	617	167	128	34.0
	90°	633	171	137	36.2
600	0°	595	162	105	28.5
	45°	603	164	136	36.2
	90°	629	170	151	39.8
800	0°	504	140	88.9	24.6
	45°	513	142	126	33.7
	90°	544	149	143	37.9
1000	0°	425	120	75.0	21.2
	45°	435	122	115	31.1
	90°	469	131	134	35.8

APPENDIX A

LIST OF VARIABLES

Note: All distances are measured in meters.

A through H	In termediate variables used in computing the values of DERY in the subroutine FCT when called upon by DHPCG or DRKGS.
A, A1, B	Intermediate variables used in computing the space derivatives of the refractive index in the electron wedge; in FCT.
ALTOBS, AZOBS	The elevation angle and the azimuth angle, measured from north toward east, of the radio ray as observed at the observing station; in OUTP. ALTOBS and AZOBS also appears in FCT, first in degrees as input parameters, and then in radians. Their values are passed to OUTP as DERY(2) and DERY(3), respectively. See Figure C-1.
ALTS, AZS	The elevation angle and the azimuth angle, measured from north toward east, of the radius vector from the observing station to the current point on the ray path; in OUTP.
AUX	A two-dimensional storage array used internally by subroutines DRKGS and DHPCG. For ERFRAC, its dimensions are (8,4) if DRKGS is used, and (16,4) if DHPCG is used.
AWG, BWG, CWQ	Direction cosines of the electron wedge gradient, in FCT.
AZOBS	See ALTOBS.
AZS	See ALTS.
AZWG	An input parameter (in degrees) which specifies the azimuth angle of the density gradient of the electron wedge; in FCT. (Its value is initially transferred from the MAIN program as DERY(4).) See App. E.
B	See A.
BNDG	The angle, in radians and then in seconds of arc, between the tangent to the ray path and the direction of the ray as observed at the observing station; in OUTP.
BWG	See AWG.
C	See A
CHPTRM	An intermediate parameter which appears in the formula for the electron density in a Chapman layer; in FCT; CHPTRM = SECSUN * DEXP (-ZCHP).
COSAZO	The cosine of AZOBS; in FCT.
COSAZW	The cosine of AXWG; in FCT.

COSBDG	Cosine of BNDG
COSTHT	Cosine of the angle between the X axis and the line from the earth's center to the electron wedge base point P; in FCT. See Fig. D-1.
COTALT	Cotangent of the elevation angle of the radio ray as received at the observing station; in FCT.
CWG	See AWG.
D	See A.
DALTMR	This is DEVALT, in milliradians.
DALTS	This is DEVALT in seconds of arc; in OUTP.
DAZS	This is DEVAZ in seconds of arc; in OUTP.
DENOM	An intermediate variable in the evaluation of DERY(2) and DERY(4); in FCT.
DERY	A four-element one dimensional array. At the time of the first call of the integrating subroutine (DRKGS or DHPCG), it is the set of "error weights" used by the subroutine in computing the truncation error at each integration step. Subsequently, its elements are the derivatives of the independent variables, Y, as computed by subroutine FCT. Before the integrating subroutine is ever called, DERY is used in initialization procedures, as follows: DERY(1) is given the value -10^{70} as a way for FCT to determine whether it is being called for the first time. DERY(2) is first used to transfer the value of FREQ from the main program to FCT, when the main program contains a DO Loop to repeat runs with different values for FREQ. Then it is used to transfer the value of ALTOBS from FCT to OUTP. DERY(3) is first used to transfer the value of HWGB from the main program to FCT, when the main program contains a DO Loop to repeat runs with different values for HWGB. Then it is used to transfer the value of AZOBS from FCT to OUTP. DERY(4) is first used to transfer the value of AZWG from the main program to FCT, when the main program contains a DO Loop at repeat runs with different values for AZWG. Then it is used to transfer the value of the sine of ALTOBS from FCT to OUTP. This transfer is not absolutely necessary, but the sine of ALTOBS is needed for initialization computations in both FCT and OUTP and the transfer merely avoids having to calculate it twice.
DEVALT	Difference between the elevation angle of the radio ray as observed at the observing station and the true elevation angle of the current point on the actual ray path, in radians; in OUTP. A positive value means the observed elevation is greater than the true elevation.

DEVAZ	Difference between the azimuth angle of the radio ray as observed at the observing station and the azimuth of the current point on the actual ray path, both measured from north around toward east; in OUTP. A positive value means the observed azimuth is greater than the true azimuth.
DEVL, DEVM	Errors in the direction cosines of the radio source as measured from the y (east) axis and from the z (north) axis, respectively; in OUTP. A positive value means the true direction cosine is greater than the one observed.
DEVM	See DEVL.
DGTORD	Numerical Constant which, as a multiplier, converts arc degrees into radians; in FCT.
DHPCG	A double-precision Fortran-language subroutine listed and explained in the IBM Scientific Subroutine Package (1968), beginning on page 337. It uses Hamming's modified predictor-corrector method to numerically integrate a system of first-order ordinary differential equations with given initial values for the dependent variables.
DRKGS	A double-precision Fortran-language subroutine listed and explained in the IBM Scientific Subroutine Package (1968) beginning on page 333. It uses the Runge-Kutta method to numerically integrate a system of first-order ordinary differential equations with given initial values for the dependent variables.
DS	Increment of length along the ray path, in OUTP.
DX, DY, DZ	Rectangular components of DS; in OUTP.
DXPRNT	An input parameter which specifies the increment of the independent variable, x, at which output is to be printed; in OUTP.
DXWG, DYWG, DZWG	Rectangular Coordinates of point in electron wedge relative to the wedge base point: rectangular components of the vector R_B in Fig. H-1; used in FCT.
DY	See DX.
DYDXO, DZDXO	Rate of change of y and of z, respectively, with respect to x, along the direction of the reversed ray path as observed at the observing station; in OUTP. The initial values of Y(2) and Y(4), respectively.
DYWG	See DXWG.
DY2NUM	An intermediate variable in the evaluation of DERY(2); in FCT.
DY4NUM	An intermediate variable in the computation of DERY(4); in FCT.
DZ	See DX.
DZDXO	See DYDXO.
DZWG	See DXWG.

E	See A.
ERFRAC	The name used by the author for the entire computer program which is the subject of this document. See flow chart, Fig. 5.
F	See A.
FCT	The name of the subroutine called in both DRKGS and DHPCG to calculate the first derivatives with respect to X of the four dependent variable in the array Y.
FREQ	The frequency of the radio signal being transmitted, in megahertz; in FCT. Its value is transferred from the MAIN program to FCT as DERY(2).
G	See A.
H	See A.
H	Height measured vertically (radially from center of earth) above the surface of the earth, H = R - RO; in OUTP.
HCHP	Scale height in the formula for the electron density in a Chapman layer; in FCT.
HEMAX	Parameter in the Chapman layer formula for electron density which represents the height above the earth's surface at which the electron density is maximum ; in FCT.
HWG	Height above the base plane of the electron wedge; in FCT. See Fig. H-1.
HWGB	Height above the base of the election wedge perpendicular to this base; in FCT. See Fig. H-1.
IHLF	This integer gives the number of times that the initially specified integration step size – PRMT(3) – has been cut in half by DRKGS or DHPCG before carrying out the step just completed. It is handed to subroutine OUTP, which can print it if desired.
IPAGE	A print control index used to control the paging; in OUTP.
IPRNT	Line printing control index; in OUTP.
ISPACE	A print control index used to provide a blank line after every five lines of print, in OUTP.
JAZWG	The integer variable index of a DO Loop used to repeat computer runs with different values for AZWG in one mode of executing ERFRAC.
JFREQ	The integer variable index of a DO Loop used to repeat computer runs with different values for FREQ, in one mode of executing ERFRAC.

JHWGB	The integer variable index for a DO Loop used to repeat computer runs with different values for HWGB, in one mode of executing ERFRAC.
L	An intermediate variable used in computing XWGB; in FCT.
LOBS, MOBS, NOBS	Direction cosines of the reversed radio ray as observed at the observing station; measured from the y(east, or y(1)) axis, the z (north, or Y(3)) axis, and the x (vertical) axis, respectively; in OUTP.
LPATH, MPATH, NPATH	Direction cosines of the currently computed increment of ray path, DS, in OUTP, as measured from the y (east), z (north), and x (station vertical) axes, respectively.
LSQ	L * L.
LTRU, MTRU	The direction cosines of the radius vector from the observing station to the current point on the ray path relative to the y (east) and z (north) axes, respectively.
MOBS	See LOBS.
MPATH	See LPATH.
MTRU	See LTRU.
MU	The atmospheric radio refractive index, in FCT.
MUOVG	MU/G; in FCT.
MUR	Gradient of the atmospheric radio refractive index. It is computed as the sum of the gradient of the tropospheric refractive index, which is evaluated first, and the ionospheric refractive index, from the Chapman layer formula.
MUX, MUY, MUZ	The partial space derivatives of the refractive index associated with the troposphere and the Chapman layer; in FCT.
MUXWG, MUYWG, MUZWG	Spatial derivatives of the refractive index associated with the electron index associated with the electron wedge; in FCT.
MUY	See MUX.
MUYWG	See MUXWG.
MUZ	See MUX.
MUZWG	See MUXWG.
NDIM	The number of first-order differential equations in the system to be integrated; it is 4 in ERFRAC, and is so specified in the MAIN program.
NE	Electron density due to the Chapman layer plus density due to electron wedge, if any; in FCT.

NEMAX	The maximum value of the electron density associated with the Chapman layer – an input parameter –; in units of 10^{10} electrons/m^3; in FCT.
NEWG	Electron density in the electron wedge, in units of 10^{10} electrons/m^3; in FCT.
NEWGMX	An input parameter which specifies the maximum electron density associated with the electron wedge in units of 10^{10} electrons/m^3; in FCT. See Appendix H, Equation H3-1.
NMU	Radio refractivity of the troposphere; in FCT. It is related to the refractive index, MU, by the following formula: $$NMU = (MU - 1) * 10^6$$ See App. I.
NMUCHP	Radio refractivity due to the Chapman layer; in FCT. See App. I.
NOBS	See LOBS.
NPATH	See L PATH.
OUTP	The name of the external subroutine called in both DRKGS and DHPCG to receive and utilize the computed results at each integration step.
PRMT	A six-element one dimensional array, as listed below. Only the first five elements of PRMT are needed or used by the subroutines DRKGS and DHPCG. The sixth element is used in ERFRAC as an initialization index for subroutine OUTP. Additional elements can be added if desired by simply dimensioning PRMT greater than six. Such elements could be used to transfer additional numbers from the main program to subroutine OUTP.
PRMT(1)	This is the value of x at which integration of the reversal ray path begins – the x-coordinate of the station which observes the ray. It is also called XO. To facilitate input, the height of the station relative to the earth, of radius RO, was chosen as the quantity to read in. RO is then added by the computer to obtain PRMT(1).
PRMT(2)	This is the value of x at which integration of the reversed ray path terminates. It is called XEND in the integrating subroutines. To facilitate input, the quantity XEND minus RO was chosen as the quantity to read in. RO is then added by the computer to obtain PRMT(2).
PRMT(3)	The initial value of the integration step size, set by the user.
PRMT(4)	The "upper error bound," used in each of the integrating subroutines DRKGS and DHPCG in setting the value of the step size parameter IHLF. See discussion in Sec. 3 of this paper.

PRMT(5)	DRKGS and DHPCG initialize this parameter to zero. The user can stop the integration at any output point by changing it to non-zero in subroutine OUTP.
PRMT(6)	PRMT(6) is initialized by the main program to the value O. As a way of informing subroutine OUTP whether or not OUTP is being called for the first time, for initialization purposes. At the first call, of OUTP, PRMT(6) is set to unity.
PRNTFX	This parameter was introduced in a line print control instruction to get output printed at the discrete values of the independent variable x which are closed to the specified values, IPRNT * DXPRNT, rather than at the x used in the next succeeding step of integration; in OUTP.
QWG	Dimensionaless Parameter which varies from -1, at base of electron wedge, to +1 at its top, along a line perpendicular to the base plane of the wedge; in FCT. See App. H.
R	Distance from the center of the earth to the point at which the current integration step is being performed; in FCT and in OUTP.
RO	The radius of the earth, which is assumed spherical in ERFRAC. RO is the datum for calculating the altitude in the formulas for tropospheric and Chapman-layer (ionospheric) refractivity; in FCT. The variable X is used to transfer the value of RO from the MAIN program to FCT and OUTP.
RANGE	Straight-line distance from observing station to current point on ray path.
RANGSQ	RANGE - RANGE.
RPOLS	The component of the RANGE perpendicular to the x (station vertical) axis; in OUTP. ("POLS" signifies "polar coordinate, relative to observing station.")
RWGB, XWGB, YWGB, ZWGB	Magnitude and rectangular components of the radius vector from the center of the earth to the electron wedge base point; in FCT. See Fig. H-1.
RWGBSQ	RWGB * RWGB.
SECSUN	Secant of the zenith angle of the sun: appears in the formula for the electron density in a Chapman layer, in FCT.
SINAZO	Sine of AZOBS.
SINAZW	Sine of AZW.
SINTHT	Sine of the angle between the x axis and the line from the earth center to the electron wedge base point, P, in FCT. See Fig. D-1.
SLOPWG	Tangent of the vertex angle of the electron wedge; in FCT.

SWG	Distance parameter within the electron wedge, in FCT. See Fig. H-1 and App. H.
TWG	Thickness of the electron wedge, measured perpendicular to the base plane of the wedge, at the point of calculation; in FCT. See Fig. H-1.
TWGO	Vertical thickness of the electron wedge at the wedge base point; in FCT. See Fig. H-1.
WGP1, WGP2	Intermediate parameters used in computing the value and space derivatives of the refractive index associated with the electron wedge, in FCT.
x, X	The independent variable in the ray tracing computation: the x-coordinate of position, measured relative to a rectangular reference frame having its origin at the center of the earth, with its x-axis passing through the station observing the ray. X is the variable name used for x in ERFRAC. Also used initially to transfer the value of RO from the MAIN program to FCT and OUTP.
XO or X_0	The initial value of X, used in subroutine FCT and OUTP, specified by PRMT(1). Not necessarily the same as RO. (The observing station need not be assumed to be the surface of the earth.)
XMRO	This stands for "x and RO"; its initial and final values are entered as input data to specify the range of the independent variable x over which the ray path is to be calculated by ERFRAC.
XMXO	This is the current value of x minuts its initial value, which is its value at the observing station; in OUTP.
XOLD, YOLD, ZOLD	Rectangular coordinates of the point on the reversed ray path as computed in the step immediately preceding the current one; in OUTP.
XWGB	See RWGB.
y	This is the rectangular coordinate y in a coordinate system whose center is at the center of the earth and whose y-axis is parallel to a line drawn due east in the horizon plane of the station which observes the ray being traced. See Fig. D-1.
Y	A four-element one dimensional array containing the elements listed below:
Y(1)	The variable name used for y in ERFRAC.
Y(2)	This is the first derivative of y with respect to x: dy/dx. It is also used in initialization procedures in ERFRAC to transfer the initial value of x, PRMT(1), from the main program to subroutine FCT, where it is called XO.
Y(3)	The variable name used for z in ERFRAC.
Y(4)	This is the first derivative of z with respect to x; dz/dx.

YDEV, ZDEV	The y (east) and z (north) components of the displacement of the current point on the ray path from a point at the same value of x on the projection of the reversed radio ray as observed at the observing station; in OUTP.
YNOM, ZNOM	The y (east) and z(north) components of a point on the projection of the reversed radio ray as observed at the observing station, at the current value of x.
YOLD	See XOLD.
Y2SQ	Y(2) * Y(2).
Y4SQ	Y(4) * Y(4).
YWGB	See RWGB.
z	This is the rectangular coordinate in a coordinate system whose center is at the center of the earth and whose z-axis is parallel to a line drawn due north in the horizon, plane of the station which observes the ray being traced. See Fig. D-1.
ZDEV	See YDEV.
ZNOM	See YNOM.
ZOLD	See XOLD.
ZWGB	See RWGB.

APPENDIX B

THE DIFFERENTIAL EQUATIONS FOR THE RAY PATH

Note: This appendix is reprinted from the Goddard Space Flight Center Report X-520-69-30, pages 120 to 124, in which the rectangular coordinate axes were labeled with x eastward, y northward, and z along the observing station's vertical, z being the independent variable. But the IBM subroutines DRKGS and DHPCG use X as the independent variable, and I thought it wise to be consistent in this usage throughout the present program, ERFRAC. Consequently, as used in ERFRAC, the formulas reprinted in this appendix are modified by chaning z to x, x to y, and y to z. See also section 5 of the present paper which explains how the two second-order equations derived in Appendix B are replaced by a system of four first-order equations for use in ERFRAC.

Those variables used in Appendix B, expressions B24 to B29, reprinted here, which are relabeled in ERFRAC, are as follows:

Original Name	ERFRAC Name	Meaning
DNOMZZ	DENOM	Eqn. B26
MUX	MUY	$\partial \mu / \partial y$
MUY	MUZ	$\partial \mu / \partial z$
MUZ	MUX	$\partial \mu / \partial x$
XZ	Y(2)	$\partial y / \partial x$
XZSQ	Y2SQ	$(\partial y / \partial x)^2$
XZZ	DERY(2)	$\partial^2 y / \partial x^2$
XZZNUM	DY2NUM	Eqn. B-25
YZ	Y(4)	$\partial z / \partial x$
YZSQ	Y4SQ	$(\partial z / \partial x)^2$
YZZ	DERY(4)	$\partial^2 z / \partial x^2$
YZZNUM	DY4NUM	Eqn. B-27

THE DIFFERENTIAL EQUATIONS FOR THE RAY PATH

Fermat's Principle states that the path taken between two points by a ray is that one such that, as compared with neighboring paths, the optical path length, the line integral of the index of refraction along the path, has a stationary value. The optical path length, OPL, for any given path between points A and B, is given by the path integral

$$OPL = \int_A^B \mu \, d s \tag{B1}$$

where μ is the index of refraction for the wave, in general a function of position in space, and ds is an element of length along the path.

In rectangular coordinates,

$$\mu = \mu(x, y, z)$$

$$\begin{aligned} d s &= (d x^2 + d y^2 + d z^2)^{1/2} \\ &= (1 + x_z^2 + y_z^2)^{1/2} \end{aligned} \tag{B2}$$

$$d z = g^{1/2} d z \tag{B3}$$

where $x = x(z)$ and $y = y(z)$ are parametric equations of the ray path;

$$x_z \equiv \partial X/\partial z, \; y_z \equiv \partial y/\partial z; \tag{B4}$$

and

$$g \equiv 1 + x_z^2 + y_z^2. \tag{B5}$$

The optical path length can now be written:

$$OPL = \int_A^B \mu(x, y, z)\, g^{1/2}\, d z = \int_A^B (x, y, z, x_2, y_z)\, dz \tag{B6}$$

where

$$F = \mu g^{1/2}$$

This integral has a stationary value, according to Fermat's Principle, and it can be shown (see for example Matthews and Walker 1964, page 309) that this implies that the integrand function F satisfies the Euler Lagrange equations:

$$\frac{\partial F}{\partial x} = \frac{d}{d z} \frac{\partial F}{\partial x_z} \tag{B7}$$

$$\frac{\partial F}{\partial y} = \frac{d}{d z} \frac{\partial F}{\partial y_z} \tag{B8}$$

The left side of Equation B7 is:

$$\frac{\partial F}{\partial x} \mu_x g^{1/2} \text{ where } \mu_x = \frac{\partial \mu}{\partial x} \tag{B9}$$

The right side develops as follows:

$$\frac{\partial F}{\partial x_z} = 1/2\ \mu\ g^{-1/2}\ (2\ x_z) = \mu\ x_z\ g^{-1/2} \tag{B10}$$

$$d/d\ z\ (\partial F/\partial x_z) = \partial/\partial\ z\ (\partial\ F/\partial\ x_z) + d\ x/d\ z\ \partial/\partial\ x\ (\partial\ F/\partial\ x_z)$$

$$+ d\ y/d\ z\ \partial/\partial\ y\ (\partial\ F/\partial\ x_z) + d\ x_z/d\ z\ \partial/\partial\ x_z\ (\partial\ F/\partial\ x_z)$$

$$+ \partial\ y_z/\partial_z\ \partial/\partial\ y_z\ (\partial\ F/\partial\ x_z) = \text{'1'} + \text{'2'} + \text{'3'} + \text{'4'} + \text{'5'} \tag{B11}$$

where

$$\text{'1'} = \mu_z\ x_z\ g^{-1/2}$$

$$\text{'2'} = x_z\ [\mu_x\ x_z\ g^{-1/2}]$$

$$\text{'3'} = y_z\ [\mu_y\ x_z\ g^{-1/2}]$$

$$\text{'4'} = x_{zz}\ [\mu\ g^{-1/2} + \mu\ x_z\ (-\ 1/2)\ g^{-3/2}\ (w\ x_z)] \tag{B12}$$

$$= x_{zz}\ [\mu\ g^{-1/2} - \mu\ x_z^2\ g^{-3/2}]$$

$$\text{'5'} = y_{zz}\ [\mu\ x_z\ (-\ 1/2)\ g^{-3/2}\ 2\ y_z]$$

$$= -\ \mu\ x_2 y_z y_{zz}\ g^{-3/2}$$

When these results are substituted into Equation B7 and it is multiplied through by $g^{1/2}$ it becomes:

$$\mu_x\ g = \mu_z\ x_z + \mu_x\ x_z^2 + \mu_y\ x_z\ y_z + \mu\ x_{zz} - \mu\ x_z^2\ x_{zz}\ g^{-1} - \mu\ x_z\ y_z\ y_{zz}\ g^{-1}; \tag{B13}$$

Rearranging terms:

$$\mu\ (1 - x_z^2/g)\ x_{zz} - \mu\ x_z\ y_z\ g^{-1}\ y_{zz} = \mu_z\ g - \mu_z\ x_z - \mu_z\ x_z^2 - \mu_y\ x_z\ y_z$$

$$= \mu_x\ g - (\mu_z + \mu_x\ x_z + \mu_y\ y_z)\ x_z. \tag{B14}$$

In exactly the same way, we obtain from Equation B8:

$$\mu (1 - y_z^2/g)\, y_{zz} - \mu\, x_z\, y_z\, g^{-1}\, x_{zz} = \mu_y\, g - \mu_z\, y_z - \mu_y\, y_z^2$$

$$+ \mu_x\, x_z\, y_z = \mu_y\, g - (\mu_z + \mu_y\, y_z + \mu_x\, x_z)\, y\, z \qquad \text{(B15)}$$

Now let

$$a = \mu$$

$$b = \mu\, x_z^2\, g^{-1}$$

$$c = \mu\, y_z^2\, g^{-1}$$

$$d = \mu\, x_z\, y_z\, g^{-1} \qquad \text{(B16)}$$

$$e = \mu_x\, g$$

$$f = \mu_y\, g$$

$$g = \mu_z + \mu_x\, x_z + \mu_y\, y_z.$$

Then Equations B14 and B15 become:

$$(a - b)\, x_{zz} = d\, y_{zz} = e - h\, x_z \qquad \text{(B17)}$$

and

$$-d\, x_{zz} + (a - c)\, y_{zz} = f - h\, y_z. \qquad \text{(B18)}$$

The solution is:

$$x_{zz} = \frac{\begin{vmatrix} (e - h\, x_z) & -d \\ (f - h\, y_z) & a - c \end{vmatrix}}{\begin{vmatrix} (a - b) & -d \\ -d & a - c \end{vmatrix}} = \frac{(a - c)(e - h\, x_z) + d\,(f - h\, y_z)}{(a - b)(a - c) - d^2} \qquad \text{(B19)}$$

$$y_{zz} = \begin{vmatrix} a - b & e - h x_z \\ -d & f - h y_z \end{vmatrix} = \frac{(a - b)(f - h y_z) + d(e - h x_z)}{(a - b)(a - c) - d^2} \qquad \text{(B20)}$$

For the special case where the ray path is entirely in the x_z plane, y(z) = 0, and from B16:

$$c = 0 \quad f = 0$$

$$d = 0 \quad h = \mu_z + \mu_x x_z \qquad \text{(B21)}$$

Then Equations B19 and B20 give:

$$x_{zz} = \frac{a(e - h x_z) + 0}{(a - b)\, a - 0} = \frac{e - h x_z}{a - b}$$

$$= \frac{\mu_x g - (\mu_z + \mu_z) x_z}{\mu - \mu x_z^2 g^{-1}} = \frac{\mu_x (g - x_z^2) - \mu_z x_z}{\mu (1 - x_z^2/g)} \qquad \text{(B22)}$$

and

$$y_{zz} = \frac{(a - b)(0 - 0) + 0}{(a - b)\, a - 0}$$

$$= 0 \qquad \text{(B23)}$$

For computer programming in the general case, we define:

$$A = MU$$

$$M = MU * XZSQ/G = MUOVG * XZSQ$$

$$C = MU * YZSQ/G = MUOVG * YZSQ$$

$$D = MU * XZ * YZ/G = MUOVG * XZ * YZ$$

$$E = MUX * G \qquad \text{(B24)}$$

$$F = MUY * G$$

$$H = MUZ + MUX * XZ + MUY * YZ$$

$$MUOVG = MU/G;\ XZSQ = XZ * XZ;\ YZSQ = YZ * YZ$$

Then from Equations B19 and B20, we have:

$$XZZNUM = (A - C) * (E - H * XZ) + D * (F - H * YZ) \quad \text{(B25)}$$

$$DNOMZZ = (A - B) * (A - C) - D * D \quad \text{(B26)}$$

$$YZZNUM = (A - B) * (F - H * YZ) + D * (E - H * XZ) \quad \text{(B27)}$$

$$XZZ = XZZNUM/DNOMZZ \quad \text{(B28)}$$

$$YZZ = YXXNUM/DNOMZZ \quad \text{(B29)}$$

APPENDIX C

VALUES OF DYDXO AND DZDXO

The initial values of y(2) = dy/dx and y(4) = dz/dx for an upward projected ray at the observing station can be written down in terms of the observed altitude, θ and ϕ azimuth, ϕ , of the ray, by inspection of Fig. C-1:

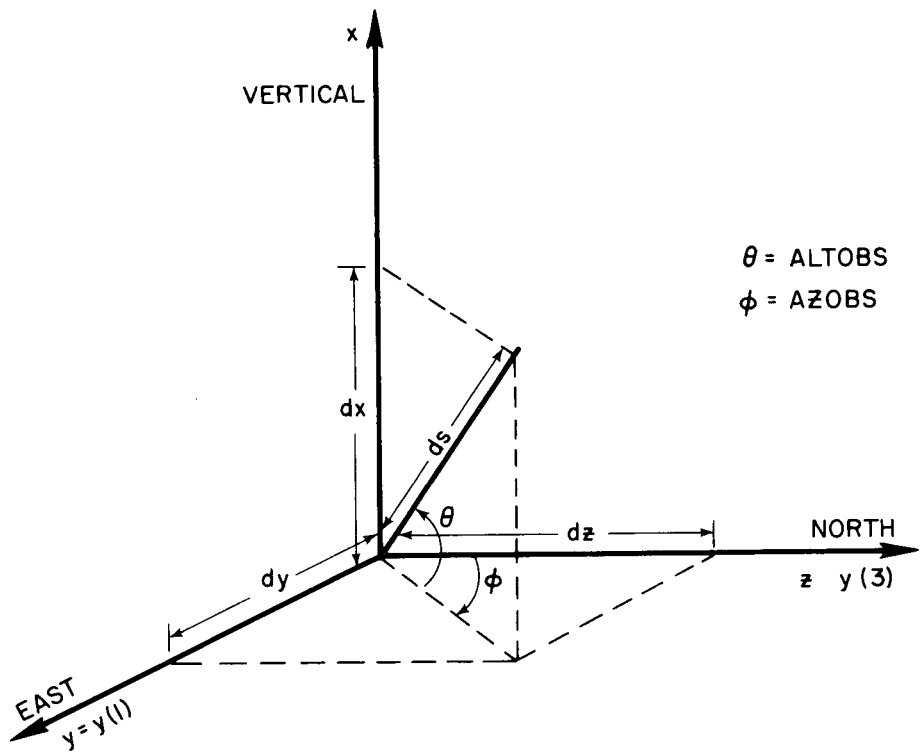

Figure C-1. Ray Geometry at Observing Station

$$d x = d s \sin \theta \tag{C1}$$

$$d y = d s \cos \theta \sin \phi \tag{C2}$$

$$d z = d s \cos \theta \cos \phi \tag{C3}$$

$$d y/d x = \cos \theta \sin \phi/\sin \theta = \cot \theta \sin \phi \tag{C4}$$

$$d z/d x = \cos \theta \cos \phi/\sin \theta = \cot \theta \cos \phi \tag{C5}$$

In ERFRAC terminology, θ = ALTOBS, and ϕ = AZOBS, and we have

$$Y(2) = COTALT * DSIN(AZOBS), \tag{C6}$$

and

$$Y(4) = COTALT * DCOS(AZOBS), \tag{C7}$$

where

$$COTALT = DCOTAN(ALTOBS) \tag{C8}$$

APPENDIX D

COORDINATES OF RAY-WEDGE BASE INTERSECTION

Here we derive formulas for the rectangular coordinates of the point at which a straight-line projection of the initial direction of the reverse ray at the observing station reaches a given altitude HWGB. This altitude is called simply h in this derivation.

The actual reversed radio ray will reach altitude HWGB at very nearly the same point, since its total bending never exceeds a very few minutes of arc, and one minute of arc at even 300 km distance corresponds to a sideways displacement of less than 0.1 km.

The problem is to determine the point, P, at which a straight line intersects a sphere of radius $r_0 + h$, where r_0 is the radius of the earth. (See Fig. D-1). Since the

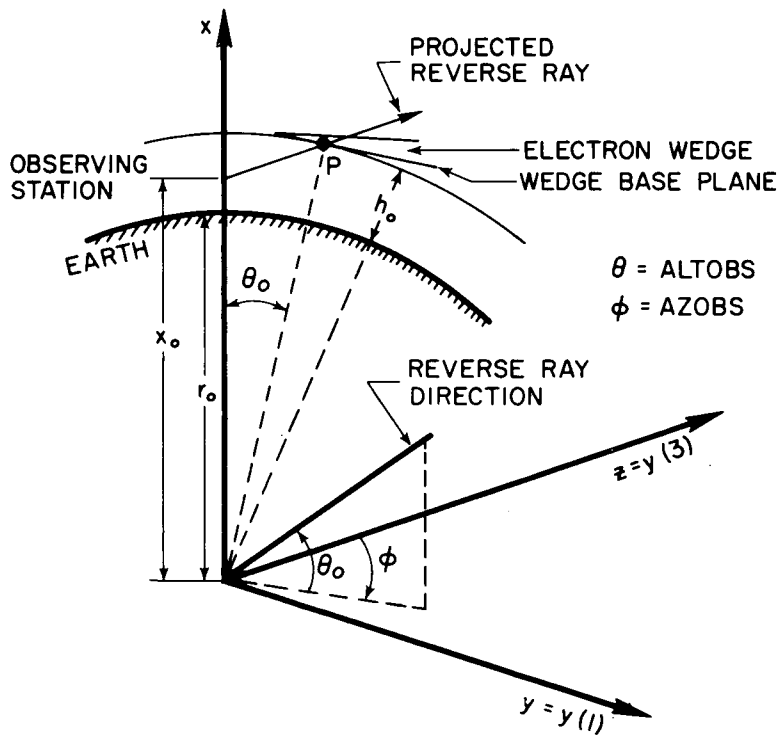

Figure D-1. Geometry for Calculating Coordinates of Ray-Wedge Intersection

line goes through the point $(x_0, 0, 0)$, which is the location of the observing station, the equations for it can be written:

$$(x - x_0)/\ell = y/m = z/n, \tag{D1}$$

where (ℓ, m, n) are the direction cosines of the line. The equation for the sphere is:

$$x^2 + y^2 + z^2 = (r_0 + h)^2 = r^2, \tag{D2}$$

where we define

$$r = r_0 + h \tag{D3}$$

Expressions for y and z from Eq. D1, when substituted into Eq. D2, give:

$$x^2 + (m\,(x - x_0)/\ell)^2 + (n\,(x - x_0)/\ell)^2 = r^2 \tag{D4}$$

or

$$x^2\,(1 + m^2/\ell^2 + n^2/\ell^2) - 2\,x_0\,x\,(m^2/\ell^2 + n^2/\ell^2) + x_0^2\,(m^2/\ell^2 + n^2/\ell^2) = r^2 \tag{D5}$$

or

$$x^2 - 2\,x_0\,(m^2 + n^2)\,x + (m^2 + n^2)\,x_0^2 = \ell^2\,r^2, \tag{D6}$$

where we have used the fact that the direction cosines satisfy the relation

$$\ell^2 + m^2 + n^2 = 1. \tag{D7}$$

If, for brevity, we introduce

$$p = m^2 + n^2 = 1 - \ell^2, \tag{D8}$$

Eq. D5 becomes:

$$x^2 - 2\,x_0\,p\,x + (p\,x_0^2 - \ell^2\,r^2) = 0 \tag{D9}$$

The more positive of the two roots is:

$$x = (2\,x_0\,p + (4\,x_0^2\,p^2 - 4\,p\,x_0^2 + 4\,\ell^2\,r^2)^{1/2}/2 \tag{D10}$$

$$= x_0\,p + (x_0^2\,p^2 - x_0^2\,p + \ell^2\,r^2)^{1/2}. \tag{D11}$$

(Consideration of Fig. D-1 shows that we want this one of the two intersections which the line theoretically makes with the sphere.)

The substitution of Eqs. D3 and D8 for r and p gives, after simplification;

$$x = x_0 (1 - \ell^2) + \ell ((r_0 + h)^2 - (1 - \ell^2) x_0^2)^{1/2} \tag{D12}$$

As a simple check on the correctness of this equation, we try it for the case $\ell = 1$, which corresponds to a ray traveling vertically upward. The equation then gives the intersection point at $x = r_0 + h$, which is correct. Also, for the case $\ell = 0$, the ray travels along a station horizontal, so that the answer given by the equation, $x = r_0$, is again correct.

In ERFRAC terminology, Eq. D12 is:

```
XWGB = (1. - LSQ) * XØ + L * DSQRT ((RØ + HWGB) * (RØ + HWGB)
                                                                    (D13)
     - (1. - LSQ) * XØ * XØ)
```

where LSQ is L * L.

The variables RO and HWGB are among those read in near the beginning of subroutine FCT and are therefore available in storage. The direction cosine L is the cosine of the angle between the reverse ray and the vertical and is therefore the sine of the observed ray altitude angle:

$$\ell = \sin \theta \tag{D14}$$

A previous computer step gave to DERY(4) this value:

```
DERY (4) = DSIN (ALTOBS),                                           (D15)
```

so that it could be transmitted to subroutine OUTP. Therefore here we merely set:

```
L = DERY (4)                                                        (D16)
```

and

```
LSQ = L * L                                                         (D17)
```

Once the value of x at the intersection is obtained by Eq. D13 the values for y and z follow from Eq. D1:

$$y = (m/\ell) (x - r_0) \tag{D18}$$

$$z = (n/\ell) (x - r_0) \tag{D19}$$

In terms of the observed altitude θ and azimuth ϕ,

$$y = (\cos\theta \sin\phi/\sin\theta)(x - r_0)$$
$$= \cot\theta \sin\phi (x - r_0); \tag{D20}$$

$$z = (\cos\theta \cos\phi/\sin\theta)(x - r_0)$$
$$= \cot\theta \cos\phi (x - r_0) \tag{D21}$$

The coefficients of $(x - r_0)$ in these two equations are, of course, just the values of the derivatives dy/dx and dz/dx for the reversed ray at the ground. These have previously been evaluated and stored as y(2) and y(4). (See App. C.) Therefore

$$YWGB = Y(2) * (XWGB - RØ) \tag{D22}$$

and

$$ZWGB = Y(4) * (XWGB - RØ) \tag{D23}$$

(In ERFRAC, y is the eastward coordinate and z is the northward coordinate.)

APPENDIX E

DIRECTION COSINES OF THE ELECTRON WEDGE GRADIENT

The electron wedge base plane in ERFRAC is taken as tangent to an earth-centered sphere of radius ($r_0 + h_0$), at the point P where the projection of the reversed ray reaches altitude h_0, as shown in Fig. D-1 of Appendix D. The "electron wedge gradient," as the term is used here, lies in the base plane, at an angle AZWG with the plane defined by the station vertical (the x axis) and the point P, as shown in Fig. E-1.

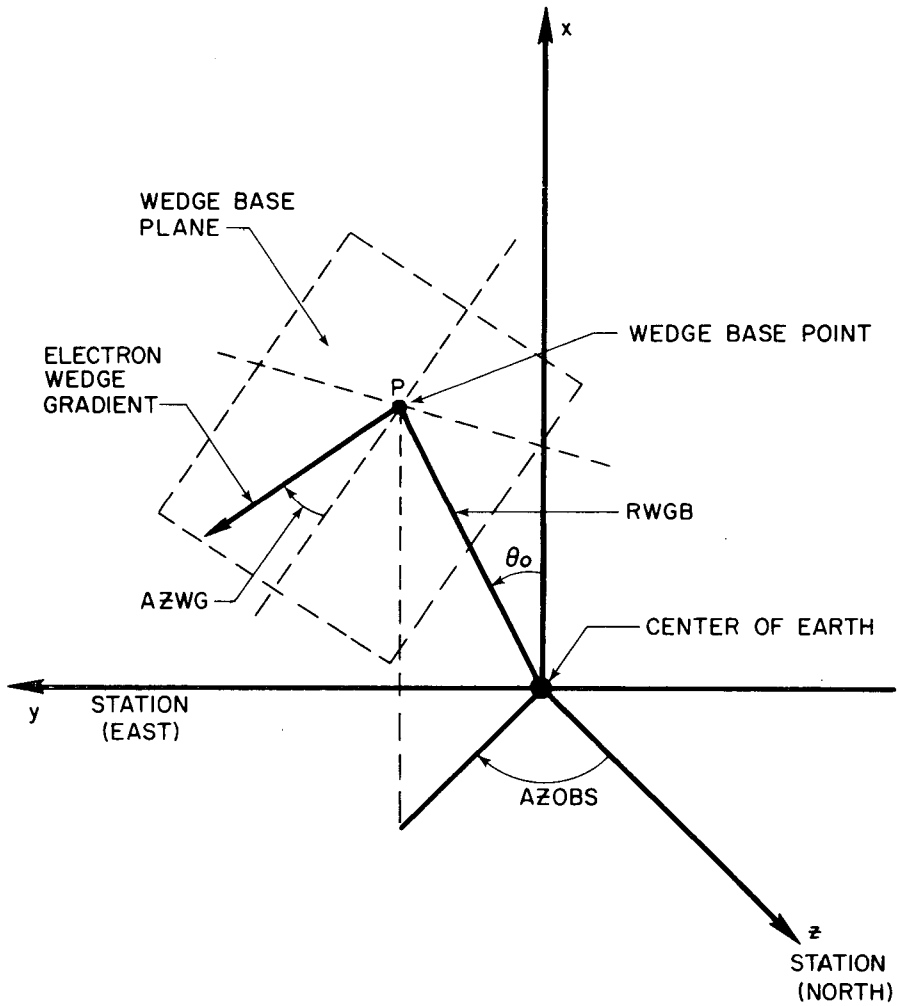

Figure E-1. Geometry of Electron Wedge Gradient

Consideration of this figure shows that the direction cosines of the wedge gradient with respect to the x, y, and z axes established at the ground station, are respectively given by

$$AWG = -\cos AZWG \sin \theta_0$$

$$BWG = \sin AZWG \cos AZOBS + \cos AZWG \cos \theta_0 \sin AZOBS$$

$$CWG = -\sin AZWG \sin AZOBS + \cos AZWG \cos \theta_0 \cos AZOBS$$

Since the coordinates of the wedge base point P are XWGB, YWGB, and ZWGB, cos θ_0 in Fig. E-1 is given by:

$$\cos \theta_0 = COSTH = XWGB/RWGB,$$

where

$$RWGB = (XWGB^2 + YWGB^2 + ZWGB^2)^{1/2}$$

Also, then, sin θ_0 is given by:

$$\sin \theta_0 = SINTHT = (1 - COSTHT^2)^{1/2}.$$

Finally, we introduce

$$SINAZW = DSIN (_{\Delta}AZWG_{\Delta})$$

and

$$COSAZW = DCOS (_{\Delta}AZWG_{\Delta})$$

The formulas for the direction cosines then become:

$$AWG = -COSAZW * SINTHT$$

$$BWG = SINAZW * COSAZO + COSAZW * COSTHT * SINAZO$$

$$CWG = -SINAZW * SINAZO + COSAZW * COSTHT * COSAZO$$

Unless the observed ray arrives at a lower angular altitude than is normal in Minitrack observations, the great circle angle between the station vertical and the wedge base point P (θ_0 in Fig. E-1) will be small, perhaps two or three degrees. Then the geographical azimuth of the wedge gradient, ϕ_{WG}, measured easterly from north, will be approximately given by:

$$\phi_{WG} \simeq \text{AZOBS} + \text{AZWG}, \tag{E1}$$

or

$$\text{AZWG} \simeq \phi_{WG} - \text{AZOBS} \tag{E2}$$

If AZOBS is specified, this equation enables one to determine the value of AZWG to use t_0 simulate a wedge whose gradient is oriented at a given azimuth angle (approximately), ϕ_{WG}, from north. However, it may actually be of more immediate interest to specify the angle between the plane containing the projected reverse ray and the station zenith and the direction of the wedge gradient, and this is AZWG itself.

APPENDIX F

FORMULAS FOR LOBS AND MOBS

Inspection of Fig. C-1 shows that the direction cosines of the reversed ray, with respect to the y (east) and z (north) axes, respectively, are given by:

$$\text{LOBS} = \cos\theta \sin\phi \tag{F1}$$

$$\text{MOBS} = \cos\theta \cos\phi \tag{F2}$$

The quantities Y(2) and Y(4) were previously calculated according to formulas C-4 and C-5 of Appendix C, as follows:

$$y(2) = \cot\theta \sin\phi \tag{F3}$$

$$y(4) = \cot\theta \cos\phi \tag{F4}$$

Since $\cos\theta = (\sin\theta)(\cot\theta)$, our formulas F-1 and F-2 can then be written:

$$\text{LOBS} = \cos\theta \sin\phi = \sin\theta \cot\theta \sin\phi = y(2) \sin\theta$$

$$\text{MOBS} = \cos\theta \cos\phi = \sin\theta \cot\theta \cos\phi = y(4) \sin\theta$$

As part of the initialization procedures, the value of $\sin\theta$ is passed from subroutine FCT to subroutine OUTP as DERY(4). Therefore, we finally have, in ERFRAC variables:

$$\text{LOBS} = \text{dery}(4) * y(2)$$

$$\text{MOBS} = \text{dery}(4) * y(4)$$

APPENDIX G

PERFORMANCE DATA FOR DRKGS AND DHPCG

Data on CPU (central processing unit) time charged for the various trials of DRKGS and DHPCG are tabulated below. The table shows the number of runs that were made at each value of IHLF used.

		DRKGS				DHPCG				
Jobs of 69.218	IHLF	0	2	4	6	0	1	3	5	7
	No. of Runs	2	1	1	1	1	1	1	1	1
	*Total CPU Time	3.45 sec				4.51 sec				

Jobs of 69.220	IHLF	4	5	6	7	5	6	7
	No. of Runs	6	12	6	6	12	6	6
	*Total CPU Time	57.35 sec				37.82 sec		

*Note: CPU Time used for program compilation and link steps, about one second, is not included.

In order to calculate the computer time required by each of the subroutines, DRKGS and DHPCG to make a given run, for purposes of comparison, I here assume that, using a given subroutine, a run with IHLF increased by one takes twice as much time.

This seems reasonable to me, since when the integration step size is cut in half, twice as many steps must be computed to cover the specified range of X (X = 0 to X = 7.) Let r and p be the time required for DRKGS and DHPCG, respectively, to make a single run with step size corresponding to IHLF = 5. Then using the assumption stated above, the data for the jobs of 69.218 give:

$$2\,(r/32) + 1\,(r/8) + 1\,(r/2) + 1\,(2\,r) = 3.45, \tag{G2-1}$$

or

$$r = 1.28 \text{ seconds}, \tag{G2-2}$$

and

$$1\,(p/32) + 1\,(p/16) + 1\,(p/4) + 1\,(p) + 1\,(4\,p) = 4.51, \tag{G2-3}$$

or

$$p = 0.84 \text{ seconds}$$

The data for the jobs of 69.220 give:

$$6\,(r/2) + 12\,r + 6\,(2\,r) + 6\,(4\,r) = 57.35, \tag{G3-1}$$

or

$$r = 1.12 \text{ seconds}, \tag{G3-2}$$

and

$$12\,(p) + (2\,p) + 6\,(4\,p) = 37.83, \tag{G3-3}$$

or

$$p = 0.79 \text{ seconds}$$

While the data for the two jobs do not lead to exactly the same results for r or for p, they are in reasonable agreement, and indicate that the computer time required by DHPCG to complete a single run with a given step size comes out significantly less than that required by DRKGS, 34% less by the first calculation and 29% less by the second.

APPENDIX H

ELECTRON DENSITY IN THE ELECTRON WEDGE

A side view of an electron wedge region as used in ERFRAC, is included in Fig. D-1, near the top of the figure. An enlarged view is shown in Fig. H-1.

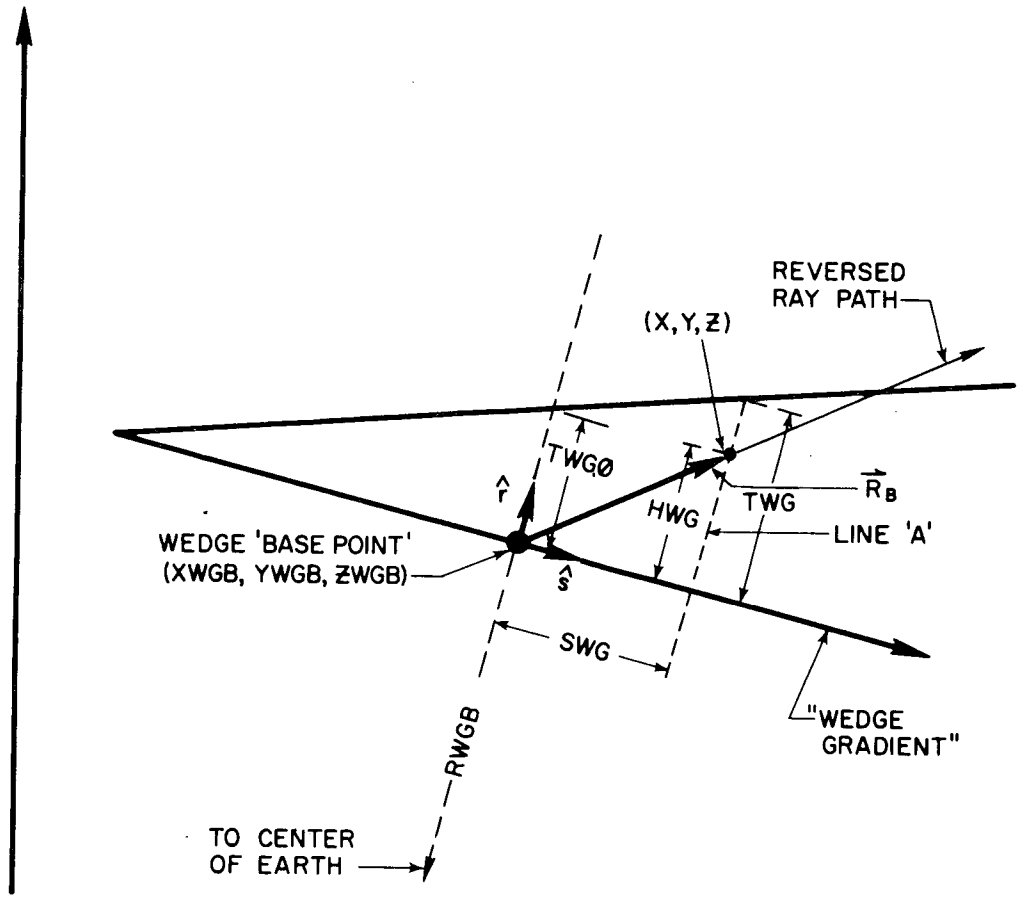

Figure H-1. Electron Wedge Geometry

The direction cosines of the wedge gradient with respect to the x, y, and z axes are called AWG, BWG, and CWG. (See Appendix E.) The overall thickness, TWG, of the wedge at an arbitrary point (x, y, z) is taken to be the thickness, TWGO, at the base point plus an additional amount which depends upon the distance SWG, that the point (x, y, z) is from the base point measured parallel to the "wedge gradient." If $\underline{R}_B$ is the vector drawn from the base point to the point (x, y, z), and $\hat{s}$ is a unit vector in the direction of the wedge gradient, then SWG is clearly given by the dot product of $\underline{R}_0$ and $\hat{s}$. Since the components of $\hat{s}$ are AWG, BWG, and CWG, this can be written:

$$SWG = AWG\,(X - XB) + BWG\,(Y - YB) + CWG\,(Z - ZB), \qquad (H2\text{-}1)$$

where XB, YB, and ZB are used here to represent the coordinates of the wedge base point. The local thickness of the wedge is then given by:

$$TWG = TWG\emptyset + (SWG)\ (SLOPWG) \qquad (H2\text{-}2)$$

Let HWG be the perpendicular distance of the arbitrary point above the base plane of the wedge, as shown in Fig. H-1. Now we assume that the electron density due to the wedge depends upon HWG in accordance with the following formula:

$$newg = newmx * \exp\ [1 - (1 - q^2)^{-1}], \qquad (H3\text{-}1)$$

where q, defined by

$$q = 2\ (hwg/twg) - 1., \qquad (H3\text{-}2)$$

varies linearly with HWG from q = -1, at the base of the wedge, to q = +1, at its top.

The function specified by equation (H3-1) symmetrical about q = 0; it is shown in Figure H-2 for q = 0 to q = +1. It closely resembles a parabola except that at each end of its range it has a point of inflection and a short but smooth tail by which it approaches

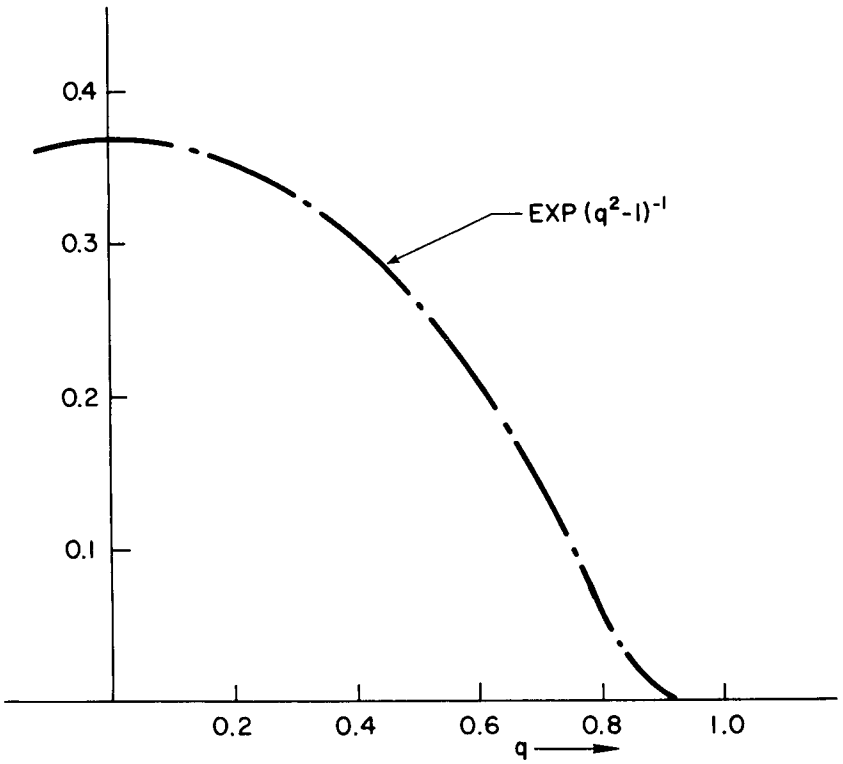

Figure H-2. Assumed Electron Density Distribution in the Electron Wedge

zero tangentially. The author tried using a simple parabolic distribution, which approaches zero at $q = \pm 1$ with a finite slope, but the integrating subroutine was unable to get past this point of discontinuity in the gradient of total electron density. He came across the function used in equation (H3-1) while browsing in a book on elementary topology.)

NEWGMX is equation (H3-1) is the maximum electron density in the wedge, which is assumed to be constant, independent of wedge thickness. This assumption is defensible in ERFRAC because of the fact that the ray being traced will never pass through the region near the vertex of the wedge, regardless of what orientation parameters are specified for the wedge. (See Appendix E.)

The parameter HWG can be written in terms of known variables by noting that it is the dot product of the vector $\vec{R}_B$, introduced above, and a unit vector r which is perpendicular to the base plane, and therefore parallel to a line drawn from the center of earth to the base point (XWGB, YWGB, ZWGB). If RWGB is the length of this line, HWG is then given by:

$$\begin{aligned} HWG = (XWGB/RWGB)\,(X - XWGB) &+ (YWGB/RWGB)\,(Y - YWGB) \\ &+ (ZWGB/RWGB)\,(Z - ZWGB) \end{aligned} \qquad \text{(H6-1)}$$

We can now derive formulas for the space partial derivatives of the electron density. Consider first the partial derivative with respect to x. Using lower case abbreviations of the variable names appearing in the formulas above, and a prime (′) to represent partial differentiation with respect to X, we have, from equation (H3-1)

$$n = n_m \exp\left(1 - (1 - q^2)^{-1}\right) \qquad \text{(H7-1)}$$

$$\begin{aligned} n' &= n\,(1 - q^2)^{-2}\,(-2q)\,q' \\ &= -2nq\,(1 - q^2)^{-2}\,q' \end{aligned} \qquad \text{(H7-2)}$$

Now from equation (H7-2),

$$\begin{aligned} q' &= 2\,(h'/h\; t'/t)/t \\ &= 2\,(h' - h\,t'/t)/t \end{aligned} \qquad \text{(H7-3)}$$

From equation (H6-1)

$$h' = x_b/R_b, \qquad \text{(H6-1)}$$

from equation (H2-2),

$$t' = s' p, \tag{H6-2}$$

and from equation (H2-1),

$$s' = a \tag{H6-3}$$

Using these results in equation (H7-3) and (H7-2), we obtain:

$$q' = 2 (x_b/R_b - h a p/t)/t$$

$$n' = - 2 n q (1 - q^2)^{-2} (2) (x_b/R_b - h a p/t)/t \tag{H9-1}$$

or

$$\partial n/\partial x = + 4 * newg * (1 - q^2)^{-2} (hwg * awg * slopwg/twg - xwgb/rwgb/rwgb)/twg \tag{H9-2}$$

Because of the symmetry in equations (H2-1) and (H5-1), the formulas for $\partial n/\partial y$ and for $\partial n/\partial z$ can immediately be written down by replacing XWGB and AWG with YWGB and BWG, to get $\partial n/\partial y$, or with ZWGB and CWG to get $\partial n/\partial z$. If we define:

$$A_H = 4 * newg * g (1. - q * q) * (1. - q * q) twg \tag{H8-1}$$

and

$$B = HWG * SLOPWG/TWG, \tag{H8-2}$$

then the three derivatives can be written:

$$\partial N_e/\partial x = A_H (B * AWG - XWGB/RWGB), \tag{H8-3}$$

$$\partial N_e/\partial y = A_H (B * BWG - YWGB/RWGB), \tag{H8-4}$$

and

$$\partial N_e/\partial z = A_H (B * CWG - ZWGB/RWGB). \tag{H8-5}$$

where we have used N_e in place of n to represent electron density.

$$n = n_m \sin^2 q$$

$$n = n_m (1 - q^2) \qquad \text{(H5-2)}$$

Differentiating this:

$$n' = -2 q n_m q'$$

$$n' = 2 n_m (\sin q \cos q) q' \qquad \text{(H5-3)}$$

Now from equation H3-1,

$$q' = 2 (h'/t - h t'/t^2).$$

$$= 2 (h' - h t'/t)/t \qquad \text{(H5-4)}$$

From equation (H5-1).

APPENDIX I

INDEX OF REFRACTION AND ITS DERIVATIVES

Lawrence et al (1964) give as an approximate expression for the index of refraction, μ, in the ionosphere:

$$\mu = 1 - b N_e/\omega^2, \tag{I1-1}$$

where

$$b = e^2/2 \epsilon_0 m. \tag{I1-2}$$

Here, N_e is the number of free electrons per cubic meter, $w = 2\pi f$ is the angular frequency of the radio wave, c is the charge on an electron, ϵ_0 is the permittivity of free space, and m is the mass of an electron. When $\omega = 2\pi f$ and the values of the constants in MKS units are substituted, the formula I1-1 becomes:

$$\mu = 1 - 40.3 N_e/f^2 \tag{I1-3}$$

In ERFRAC, N_e is in units of 10^{10} electrons/m^3 and f is in units of 10^6 Hz. Using these units, equation I1-3 becomes:

$$\mu = 1 - 0.403 N_e/f^2 \tag{I2-1}$$

For convenience in computation, the refractivity, N, is defined as follows:

$$N = (\mu - 1) \times 10^6 \tag{I2-2}$$

From equation (I2-1),

$$N = - 4.03 \times 10^5 N_e/f^2 \tag{I2-3}$$

Since $\mu = 1 + 10^{-6}$ N, it is clear that

$$\partial \mu/\partial x = 10^{-6} \partial N/\partial x. \tag{I2-4}$$

From equation (I2-3),

$$\partial N/\partial x = - (4.03 \times 10^5/f^2) \partial N_e/\partial x \tag{I2-5}$$

Then equation (I2-4) becomes:

$$\partial \mu / \partial x = - (.403/f^2) \partial N_e / \partial x \qquad \text{(I3-1)}$$

Now using equation (H8-3) of Appendix H,

$$\partial \mu / \partial x = - (.403/f^2) A_H (B * AWG - XWGB/RWGB), \qquad \text{(I3-2)}$$

where A_H is given by equation (H8-1).

(I3-3)

If now we define the new variable A as follows:

$$A = - (.403/f^2) A_H. \qquad \text{(I3-4)}$$

$$MUXWG \equiv \partial \mu / \partial x = A (B * AWG - XWGB/RWGB) \qquad \text{(I3-5)}$$

then we have

$$MUYWG = A (B * BWG - YWGB/RWGB) \qquad \text{(I3-6)}$$

$$MUZWG = A (B * CWG - ZWGB/RWGB) \qquad \text{(I3-7)}$$

APPENDIX J

INPUT DATA FORMAT

As originally designed and written, eight cards of input data are required for ERFRAC, as follows:

Card No.	Format	Variables, In Order (Refer to List of Variables in Appendix .)
		Note: All distances are to be specified in meters.
1	4F10.0	RO; $XMRO_{start}$; $XMRO_{end}$; INITIAL STEP SIZE.
2	D8.2	PRMT(4). (Upper bound on truncation error. Enter in the form bb1.D-mn, where bb represents two blanks and mn is the desired exponent, such as 09.)
3	F5.0	FREQ. (In megahertz.)
4	2F10.0	ALTOBS; AZOBS. (Both in degrees.)
5	4F10.0	SECSUN; HCHP; HEMAX; NEMAX
6	5F10.0	NEWGMX; HWGB; TWGO; SLOPWG; AZWG. (Enter AZWG in degrees.)
7	4F10.0	DERY(1); DERY(2); DERY(3); DERY(4).
8	F10.0	DXPRNT.

A SURVEY ON SOME MATHEMATICAL MODELS OF THE VERY LOW FREQUENCY WAVE PROPAGATION*

David H. S. Cheng
University of Missouri
Columbia, Missouri

*This work was published in X-521-70-425.